GOETHE
UNIVERSITÄT
FRANKFURT AM MAIN

Downscaling of general circulation models in two alpine regions: The European Alps and the Himalayas

Dissertation

zur Erlangung des Doktorgrades

der Naturwissenschaften

vorgelegt beim Fachbereich Geowissenschaften/Geographie

der Johann Wolfgang Goethe-Universität

in Frankfurt am Main

von

Andreas Dobler

aus Appenzell, Schweiz

Frankfurt 2010

(D30)

vom Fachbereich Geowissenschaften/Geographie der

Johann Wolfgang Goethe-Universität als Dissertation angenommen.

Dekan:

Gutachter:

Datum der Disputation:

Danksagung

Contents

Abstract

The main objective of this thesis is to examine the possibilities and limitations of high resolution climate projections in orographically influenced areas on the examples of the European Alps and the Himalayas. In particular, the question whether observed regional patterns can be better represented in the regional data than in the driving large-scale data is of interest. To this end, regional climate simulations by the COSMO-CLM and from two statistical downscaling methods are compared to ERA40 reanalysis data and data from the global atmosphere-ocean model ECHAM5/MPIOM using various parameters of the climate system.

A comparison with the reanalysis on the basis of daily precipitation shows that the accuracy of the COSMO-CLM rainfall data on the 0.5° scale is comparable with ERA40 and statistically downscaled ERA40 precipitation. An additional bias correction of the COSMO-CLM precipitation shows good results. However, a sufficient number of rain days is necessary to give a certain degree of security in the bias estimate. In the present study a threshold of about 500 rain days is proposed.

For the South Asian region the reproduction of a realistic Indian summer monsoon (ISM) is of high relevance. Considering only the mean values and temporal variabilities of different large-scale indices, the COSMO-CLM provides no added value compared to the driving data. However, the spatial patterns of rainfall and vertical wind shear as well as the temporal correlation of the ISM indices are improved by the application of the COSMO-CLM to the ECHAM5/MPIOM model.

COSMO-CLM projections carried out for the years 1960 to 2100 show negative trends in the ISM indices for the SRES scenarios A2, A1B and B1. The most negative trends are found in A2, followed by A1B and B1. Almost no trends appear in the commitment scenario. Although there are large temporal variabilities, the trends in rainfall, outgoing longwave radiation and meridional and zonal wind shear are statistically significant in many regions of the simulation domain. For northwest India, the projections partially show a decline in rainfall during the monsoon season of more than 70% in 100 years. The decrease in wind shear is found to be based mainly on changes in the upper troposphere at 200 hPa.

While in the COSMO-CLM projections all ISM indices show simultaneous negative trends, the trends for the all-India monsoon rainfall in the

ECHAM5/MPIOM model are positive. Following the definition of the indices, simultaneous trends are more likely and the COSMO-CLM is able to add value on the global projections in this aspect as well. Overall, the results of this study show that the COSMO-CLM adds valuable regional information to the global models in the two regions investigated.

For the river basins of the upper Danube and the upper Brahmaputra, the COSMO-CLM projections reveal a significant rise in temperature in both basins and for all seasons from 1960 to 2100. The values are generally higher in the Brahmaputra area with the highest values in the region of the Tibetan Plateau. For precipitation, there are also clear seasonal trends, such as an increase in spring precipitation in the upper Danube. The largest trends are again simulated in the region of the Tibetan Plateau with an increase of up to 50% in the drought length from June to September and a simultaneous increase of about 10% for the maximum amount of rainfall on five consecutive days. For the region Assam in India, the projections show further an increase of 25% in the number of consecutive dry days during the monsoon season.

Kurzzusammenfassung

(Eine ausführliche deutsche Zusammenfassung findet sich in Kapitel 7.)

Das Ziel dieser Studie ist es, die Möglichkeiten und Grenzen von hochauflösenden Klimaprojektionen in orographisch beeinflussten Gebieten an den Beispielen der europäischen Alpen und des Himalajas zu prüfen. Insbesondere wird die Fragestellung untersucht, ob beobachtete regionale Muster in den höher aufgelösten Daten besser wiedergegeben werden als in den antreibenden großskaligen Daten. Dazu werden regionale Klimasimulationen des COSMO-CLM Modells und Daten von zwei statistischen Regionalisierungsmethoden mit ERA40 Reanalysen sowie Daten des globalen Atmosphäre-Ozean Modells ECHAM5/MPIOM für verschiedene Parameter des Klimasystems verglichen.

Ein Vergleich mit den Reanalysen anhand täglicher Niederschlagsstatistiken ergibt, dass die COSMO-CLM Niederschlagsdaten auf der 0.5° Skala vergleichbar sind mit ERA40 Niederschlägen und mit statistisch regionalisierten ERA40 Niederschlägen. Eine zusätzliche Fehlerkorrektur der COSMO-CLM Niederschläge liefert gute Ergebnisse. Dabei sind jedoch etwa 500 Regentage notwendig, um eine robuste Fehlerabschätzung zu gewährleisten.

Für das südasiatische Gebiet ist eine realistische Wiedergabe des indischen Sommermonsuns (ISM) in den Modellen von hoher Relevanz. Betrachtet man nur die Mittelwerte und zeitlichen Variabilitäten von verschiedenen Indizes des ISM, so liefert das COSMO-CLM keinen Mehrwert im Vergleich zu den antreibenden Daten. Allerdings werden die räumlichen Strukturen von Niederschlag und vertikaler Windscherung, sowie die zeitliche Korrelation der modellierten Indizes gegenüber dem ECHAM5/MPIOM Modell verbessert.

Die durchgeführten COSMO-CLM Projektionen für die Jahre 1960 bis 2100 zeigen negative Trends des ISM für die SRES Szenarien A2, A1B und B1. Die negativsten Trends sind dabei im Szenario A2 zu finden, gefolgt von A1B und B1. Fast keine Trends zeigen sich im *commitment* Szenario. Trotz großen zeitlichen Variabilitäten sind die Abnahmen in Niederschlagsmengen, ausgehender langwelliger Strahlung und Windscherung statistisch signifikant in großen Regionen des Simulationsgebietes. Für Nordwest-Indien weisen die Projektionen teilweise einen Rückgang der Monsunniederschläge von über 70% in 100 Jahren auf. Der

Rückgang der Windscherung ist hauptsächlich auf Veränderungen in der oberen Troposphäre bei 200 hPa zurück zu führen.

Während in den COSMO-CLM Projektionen alle Indizes des ISM synchrone Negativtrends aufweisen, sind die Trends für den Monsunregen über Indien im globalen ECHAM5/MPIOM Model positiv. Gemäß den Definitionen der verschiedenen Indizes, sind jedoch synchrone Trends wahrscheinlicher und das COSMO-CLM liefert zu den globalen ISM Projektionen ebenfalls einen Mehrwert. Insgesamt zeigen die Ergebnisse dieser Studie, dass das COSMO-CLM wertvolle regionale Zusatzinformationen zu den globalen Modellen in den beiden untersuchten Regionen liefert.

Für die Einzugsgebiete der oberen Donau und des oberen Brahmaputra liefern die COSMO-CLM Projektionen einen signifikanten Anstieg der Temperatur für alle Jahreszeiten der Jahre 1960 bis 2100. Die Werte sind generell höher im Brahmaputragebiet, mit den größten Trends in der Region des tibetanischen Plateaus. Im Niederschlag zeigen die saisonalen Anteile ebenfalls klare Trends, beispielsweise eine Zunahme des Frühjahrsniederschlags im Einzugsgebiet der oberen Donau. Die größten Trends werden wiederum in der Region des tibetanischen Plateaus projiziert mit einem Anstieg von bis zu 50% in der Länge der Trockenperioden zwischen Juni und September und einem gleichzeitigen Anstieg von etwa 10% für die maximale Niederschlagsmenge an fünf aufeinander folgenden Tagen. Für die Region Assam in Indien, zeigen die Projektionen zudem eine Zunahme von 25% in der Anzahl der aufeinander folgenden trockenen Tage während der Monsunzeit.

Chapter 1

Introduction

With the increasing availability of inexpensive computational resources, general circulation models (GCMs) and regional climate models (RCMs) have become very popular and are broadly used at many scientific institutions worldwide. They serve as helpful tools to understand climate processes, simulate historic climates and to project future climates under various assumptions (e.g., future greenhouse gas concentrations or land use).

Most of the recently performed climate projections use scenarios defined in the special report on emission scenarios (SRES, Nakicenovic and Swart, 2000) of the international panel on climate change (IPCC, `http://www.ipcc.ch`). Each scenario assumes different future developments and together they cover a large part of the uncertainties in future emissions. The output of more than 20 atmosphere-ocean GCMs (AOGCMs) following the SRES scenarios have been collected within the coupled model intercomparison project (CMIP) Phase 3 (Meehl et al., 2007, `http://cmip-pcmdi.llnl.gov/`). This data provided the basis for a large part of the research results presented in the fourth IPCC assessment report.

In the present work, simulations according to the following four SRES scenarios are considered.

- A1B: A very rapid economic growth with a low global population growth that peaks in mid-century and declines thereafter. It also assumes rapid introduction of new and more efficient technologies and a balance of fossil and non-fossil energy sources.

- B1: A convergent world with the same global population as in the A1 storyline but with rapid changes in economic structures toward a service and information economy, with reductions in material intensity, and the introduction of clean and resource-efficient technologies.

- A2: A very heterogeneous world with continuously increasing global population and regionally oriented economic growth that is more fragmented and slower than in other story lines.

- Commitment: The greenhouse gas concentrations are held fixed at the year 2000 level.

Currently, the demand for climate information increases in many scientific disciplines like hydrology, climate change impact and adaption studies, but also in politics. However, most GCMs are run with a horizontal grid resolution of about 200 km due to still arising limitations in computational power. While it is necessary to generate these global GCM projections, for instance to force RCMs at the boundary, the spatial resolution is often not sufficient to fulfill the requirements of highly resolved regional information. A downscaling to a grid resolution of 0.5° (50 km) or less is necessary to generate regional precipitation patterns (Ahrens, 2003; Beck et al., 2004; Dobler and Ahrens, 2008; Frei et al., 2003; Salathé, 2003), especially in regions with a complex orography. Furthermore, while most GCMs show agreement in the projected global and continental temperature trends in the 21st century, there is large disagreement in the projections of precipitation at the regional scale (Annamalai et al., 2007; IPCC, 2007b) and a downscaling may add some value in this aspect.

Thus, the use of downscaling methods has significantly increased in the last years. However, the resulting regional climate projections include uncertainties due to: 1) the downscaling approach, 2) the driving GCM, 3) the greenhouse gas emission scenario, and 4) natural climate variability.

Generally, two classes of downscaling methods can be distinguished (Murphy, 1999; Xu, 1999): a) dynamical downscaling via a high-resolution simulation of physical processes (e.g., by a RCM) and b) statistical downscaling employing observed relationships between coarse and fine scales. Furthermore, the two methods may be used in combination and statistical downscaling methods can be applied as bias correction methods, where the final data is at the same scale as the input fields.

The here presented work investigates the possibilities, limitations, uncertainties and applications of different methods with the purpose to bridge the scale gap between GCM projections and impact modeling. The investigation focuses on two spatially heterogeneous areas including two major alpine regions: the European Alps and the Himalayas.

In chapter 2 of this work, different downscaling methods are evaluated with the help of daily precipitation statistics in Europe and South Asia. In chapter 3, an analysis of the representation of the Indian summer monsoon (ISM) system in the RCM COSMO-CLM (`http://www.clm-community.eu`) and in the driving GCMs is given. Chapter 4 deals with the discussion of climate projections for the ISM generated by the COSMO-CLM and the AOGCM ECHAM5/MPIOM. To provide different possible future developments, the SRES scenarios A1B, A2, B1 and commitment have been simulated for the time span 1960-2100. In chapter 5 the issue of a changing climate in the upper Danube and the upper Brahmaputra river basin (UDRB and UBRB) is assessed by the use of seasonal trends

of daily precipitation and temperature indicators from 1960 to 2100. Finally, chapter 6 gives the conclusions drawn from this work and chapter 7 provides a German summary. An evaluation study on radiation fluxes over Europe by Kothe et al. (2010), including the COSMO-CLM simulations generated for this thesis, is shown in the Appendix.

As a further application, the downscaled projections have been used within the BRAHMATWINN project (`http://www.brahmatwinn.uni-jena.de`) as input to simulate historical and future water balances of the UDRB and the UBRB (Prasch et al., 2010), in glacier and permafrost modeling (Lang et al., 2010) and in the calculation of climate change indicators (Giannini and Giupponi, 2010; Giannini et al., 2010).

Chapter 2

Precipitation by a regional climate model and bias correction in Europe and South Asia

2.1   Abstract

Because coarse-grid global circulation models do not allow for regional esti-
mates of the water balance or trends of extreme precipitation, downscaling of
global simulations is necessary to generate regional precipitation. This paper ap-
plies for downscaling the regional climate model CLM as a dynamical downscaling
method (DDM) and two statistical downscaling methods (SDMs). Because the
SDMs neglect information available to the DDM, and vice versa, a combination
of the dynamical and statistical approaches is proposed here. In this combined
approach, a simple statistical step is carried out to correct for the regional model
biases in the dynamically downscaled simulations.

To test the proposed methods, coarse-grid global re-analysis data (ERA40 with
$\sim 1.125°$ grid spacing) is downscaled in two regions with different climatology and
orography: one in South Asia and the other in Europe. All of the methods are
tested on daily precipitation with $0.5°$ grid spacing. The SDMs are generally
successful: the standardized root mean square error of rain day intensity is re-
duced from ERA40's 0.16 to 0.10 in a test area to the west of the European Alps.
The CLM simulations perform less well (with a corresponding error of 0.14), but
represent a promising approach if the user requires flexibility and independence
from observational data. The proposed bias correction of the CLM simulations
performs very well in European test areas (better than or at least comparable
with the SDMs; i.e., with a corresponding error of 0.07), but fails in South Asia.
An investigation of the observed and simulated precipitation climate in the test
areas shows a strong dependence of the bias correction performance on sampling
statistics (i.e., rain day frequency) and on the robustness of bias estimation.

2.2   Zusammenfassung

Da grob aufgelöste globale Zirkulationsmodelle keine regionale Einschätzung des Wasserhaushalts oder der Entwicklung von Extremniederschlägen erlauben, ist ein Hinunterskalieren der globalen Klimaprojektionen auf die regionale Skala notwendig, um regionale Niederschlagsfelder zu erzeugen. In dieser Arbeit werden das regionale Klimamodell CLM für ein dynamisches Hinunterskalieren und zwei statistische Skalierungsmethoden angewendet. Da statistische Methoden Information vernachlässigen, welche in dynamischen Methoden verwendet wird, und umgekehrt, stellen wir hier einen kombinierten Ansatz vor. In diesem Ansatz wird ein einfacher statistischer Schritt durchgeführt um regionale, systematische Fehler in den dynamisch hinunterskalierten Simulationen zu korrigieren.

Um die Methoden zu testen, werden grob aufgelöste globale Reanalyse Daten (ERA40 mit ∼1.125° Gitterabstand) in zwei Regionen mit unterschiedlicher Klimatologie und Orographie skaliert: Eine in Südasien die andere in Europa. Alle Methoden werden im Vergleich mit täglichem Niederschlag mit 0.5° Gitterabstand getestet. Die statistischen Skalierungsmethoden sind generell erfolgreich: Der standardisierte mittlere quadratische Fehler der Regentagintensität von ERA40 wird von 0.16 auf 0.10 reduziert in einem Testgebiet westlich der Europäischen Alpen. Die CLM Simulationen schneiden weniger gut ab (mit einem entsprechenden Fehler von 0.14), sind aber vielversprechend, wenn Unabhängigkeit von Beobachtungsdaten und Flexibilität erwünscht sind. Die vorgestellte Fehlerkorrektur der CLM Simulationen funktioniert sehr gut in europäischen Testgebieten (besser oder zumindest vergleichbar mit den statistischen Skalierungsmethoden, d.h. mit einem entsprechenden Fehler von 0.07), schlagen aber fehl in Südasien. Eine Untersuchung der beobachteten und simulierten Regentaghäufigkeit in den Testgebieten zeigt eine grosse Abhängigkeit der Güte der Fehlerkorrekturen von Sampling-Statistiken (d.h. Regentaghäufigkeit) und von der Robustheit der Modellfehlerschätzung.

2.3   Introduction

Climate predictions of regional precipitation patterns are important for investigations of water balance or changes in heavy precipitation. Although simulations performed using current global circulation models (GCMs) feature a grid resolution of about $2°$, this is insufficient for examining regional precipitation patterns, which requires downscaling to a grid resolution of $0.5°$ or less (Ahrens et al., 2003; Beck et al., 2004; Frei et al., 2003; Salathé, 2003).

Generally, two different classes of downscaling methods may be applied (Murphy, 1999; Xu, 1999)): a) dynamical downscaling methods (DDMs) based on simulations of physical processes at a fine scale, and b) statistical downscaling methods (SDMs) that employ observed statistical relationships between the coarse and fine scale. A wide range of different downscaling methods have been reviewed by Wilby and Wigley (1997); Giorgi et al. (2001). As a DDM, this paper applies the regional climate model CLM (`http://www.clm-community.eu`; Böhm et al., 2006). The DDM performance is compared with the performance of two simple SDMs in terms of our predictant, daily precipitation with $0.5°$ grid resolution. To minimize the influence of predictor uncertainties on the downscaling results, we use ERA40 (Uppala et al., 2005) re-analysis data from the European Centre for Medium-Range Weather Forecasts (ECMWF) rather than GCM simulations. The global ERA40 re-analysis has only small circulation errors, thereby yielding an optimal environment for evaluation of the different downscaling methods. In using the CLM, precipitation is generated by regional climate simulations driven with ERA40 data. For the SDMs, the coarse-grid ERA40 precipitation is used as a predictor. The use of coarse-grid precipitation as a predictor for SDMs has previously been successfully applied by Widmann et al. (2003).

This paper also tests the potential of combining the dynamical and statistical downscaling approaches via the application of bias correction to the dynamically downscaled simulations. The goal is to make use of the advantages of the two approaches (DDM and SDMs). The employed bias correction methods (BCMs) are conceptually identical to the applied SDMs.

The employed statistical methods make use of the empirical relationships between the predictants (i.e., ERA40 precipitation in the case of the SDMs and CLM precipitation in the case of the BCMs) and observations over a certain training period to reduce the bias in rain day frequency and rain day intensity over an independent evaluation period. Therefore, the statistical methods depend on the stationarity of any error in the predictant from the training to evaluation periods (as discussed in greater detail below) and fail if this stationarity is not achieved; however, methods implemented to reduce model biases have shown good results, both for downscaling (Wood et al., 2004) and bias correction (Hay et al., 2002).

Our methods are applied and evaluated in six regions with different climates.

The results of this evaluation may be used as a guide for the future choice of methods employed in the downscaling of climate projections from GCMs. One of our aims is to assess the performances of the different methods in terms of transferability from one climate region to another; i.e., to determine the degree to which the performances of the downscaling methods are region-specific. As part of this transferability study, we also intend to identify deficiencies in the different downscaling and bias correction methods. The transferability of the CLM to different climate zones of the earth (using the example of precipitation) is addressed in detail by Rockel and Geyer (2008). Additional transferability studies, including analyses of other regional climate models, are outlined in Takle et al. (2007).

The remainder of this paper is organized as follows. Section 2 describes the analyzed data and Section 3 the applied methods. Section 4 presents and discusses the results, and the conclusions are provided in Section 5.

2.4 Data

2.4.1 Regions

Test regions with contrasting climatology and orography were chosen in two domains: Europe (Fig. 2.1), with a generally temperate climate, and South Asia (Fig. 2.2), with a tropical monsoon climate. In turn, three evaluation regions were selected within each of these two domains. The three European evaluation regions are based on those used previously by Schmidli et al. (2006): a flat area to the west of the Alps (WEST), an alpine region in southern Switzerland (TIC), and a region containing the northern alpine ridge (NALP). The sizes of the three regions are $3.5° \times 3°$, $2° \times 2°$, and $3.5° \times 2°$, respectively (see. Fig. 2.1). Precipitation in TIC and NALP is strongly influenced by orography. We chose the same European evaluation regions as those used previously to enable a comparison of our methods with the local intensity scaling (LOCI) method used by Schmidli et al. (2006). The three selected evaluation regions in the South Asian domain (each $2° \times 2°$; Fig. 2.2) are Central India (CI), Lhasa (LH), and Assam (AM). CI is located upon the Deccan Plateau, and LH and AM are located to the north and south of the eastern Himalayas, respectively. Thus, precipitation in LH and AM is strongly influenced by orographic factors.

2.4.2 Reference data sets

Observation-based reference data sets are required for training of the SDMs, training of the BCMs, and for evaluation purposes. For the South Asian domain, the East Asia Daily Precipitation dataset (Xie et al., 2007) is used on its native $0.5°$ grid for the period 1978-2001. For the European Alpine area, a 29-year
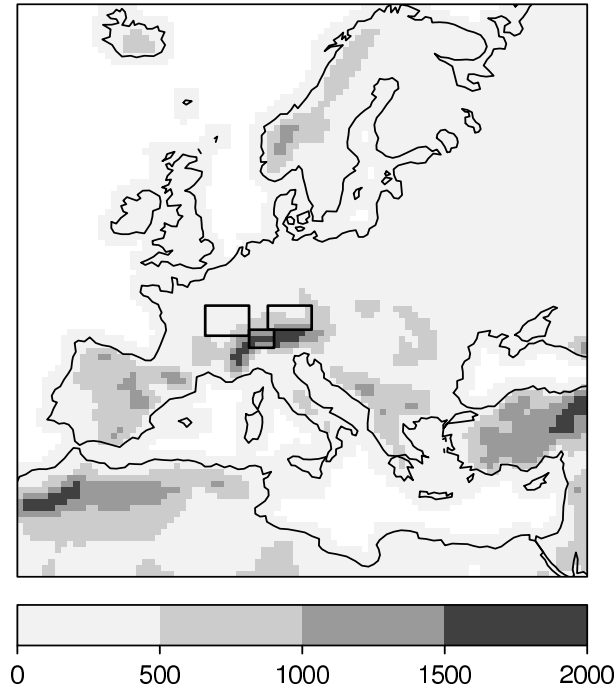
Figure 2.1: Orography (m) used for the regional climate simulations with the CLM and evaluation regions WEST, TIC, and NALP (from left to right) in the European computational domain.

(1971-1999) daily analysis at a grid resolution of $1/6°$ is available (Frei and Schär, 1998, version 4.1). However, the European dataset is averaged to a $0.5°$ grid for consistency; thus, the target resolution of downscaling in both domains is $0.5°$. Both data sets are gauge-based analyses. In the South Asian region, the lower density of the gauge network is compensated by the use of monthly climatologies to correct for orographic effects (Xie et al., 2007). The data sets are split into a training period (South Asia: 1978-1989, Europe: 1971-1985) and an evaluation period (1990-2001 and 1986-1999, respectively). The impact of the limited duration of the periods assigned for daily training and evaluation of the data for the South Asian region are discussed in Section 4. Figures 2.3a) and 2.4a) show the mean yearly precipitation during the entire observation periods for parts of the European and South Asian domains, including the evaluation regions. Note that the SDMs and BCMs yield precipitation fields on the grid of the reference data sets by design as will be discussed in Section 3.

2.4.3   ERA40 data

ERA40 re-analyses (Uppala et al., 2005) from the ECMWF with a resolution of $\sim 1.125°$ (T159) are used as a substitute for coarse-grid GCM projections.
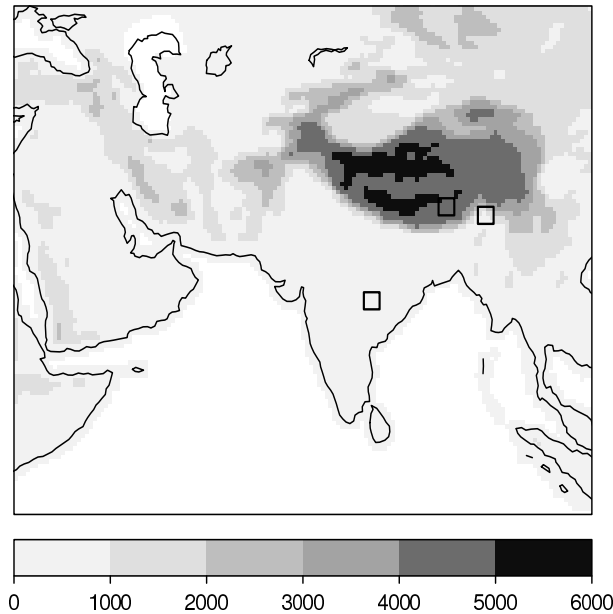
Figure 2.2: As for Fig. 2.1, but for the South Asian computational domain. Here the evaluation regions (from left to right) are Central India, Lhasa, and Assam.

Several ERA40 fields are used as forcing data for the DDM. For the SDMs, ERA40 precipitation interpolated to a $1.25°$ regular latitude/longitude grid is used as a predictor.

While the large-scale circulation in the re-analysis is bound to observations, precipitation is generated by the model of the ECMWF analysis system. Figures 2.3b) and 2.4b) show the mean yearly ERA40 precipitation during the observation periods in parts of the European and South Asian domains. Note that to enable comparison, the precipitation fields in Figs. 2.3b) and 2.4b) have been bilinearly interpolated to the target grid with $0.5°$ grid spacing.

2.5 Methods

Figure 2.5 provides a schematic overview of the different methods applied in this paper. The downscaling methods are either a dynamical downscaling method (DDM) or one of two statistical downscaling methods (SDMs). We also propose two bias correction methods (BCMs) that combine the DDM with an additional bias correction step based on the SDMs. The methods are described in the following subsections.
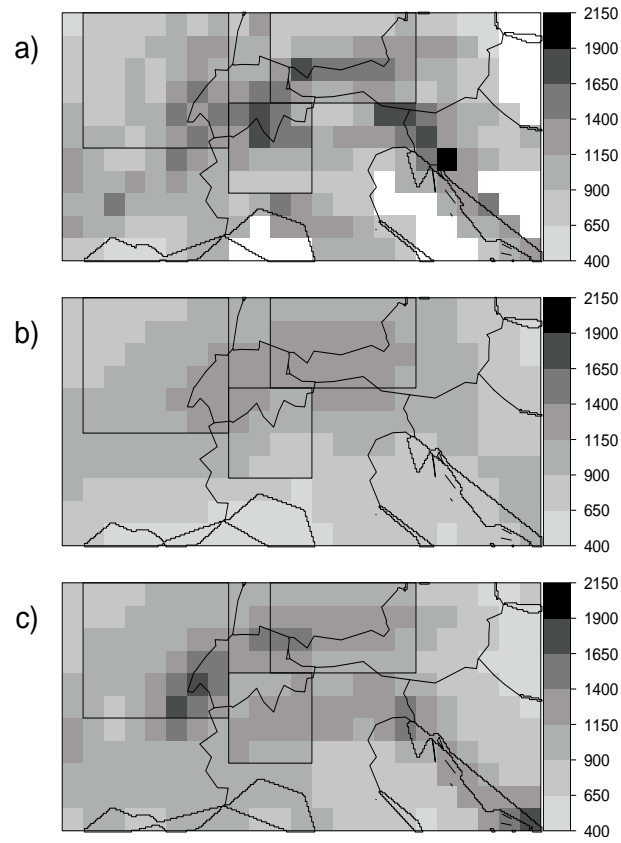
Figure 2.3: Mean yearly precipitation (mm/a) during the observation period 1971-1999 for a) observations, b) ERA40, and c) dynamically downscaled ERA40 precipitation for part of the European domain containing the three evaluation regions.

2.5.1   Dynamical downscaling using the CLM

Dynamical downscaling of ERA40 simulations employs the CLM (clm 3.1, climate version of the *COSMO* model from the *German meteorological service* (DWD); Böhm et al. 2006). The model is driven by ERA40 data in two computational domains: Europe and South Asia (see Figs. 2.1 and 2.2). A rotated grid is used in each of the domains with a grid spacing of 0.44°. The model is driven by conventional forcing at the lateral boundaries with an update interval of 6 hours. As shown in Figs. 2.1 and 2.2, the orography in the South Asian domain shows relatively steep slopes compared with the European domain. The two regions also show major differences in their climatological properties, such as the total yearly amount of precipitation (Figs. 2.3c and 2.4c); however, to assess the transferability problem we use the same setup and model version in both domains. This setup is equivalent to that used for the CLM consortial runs (Hollweg et al., 2008) except for the horizontal resolution (0.44° in the present
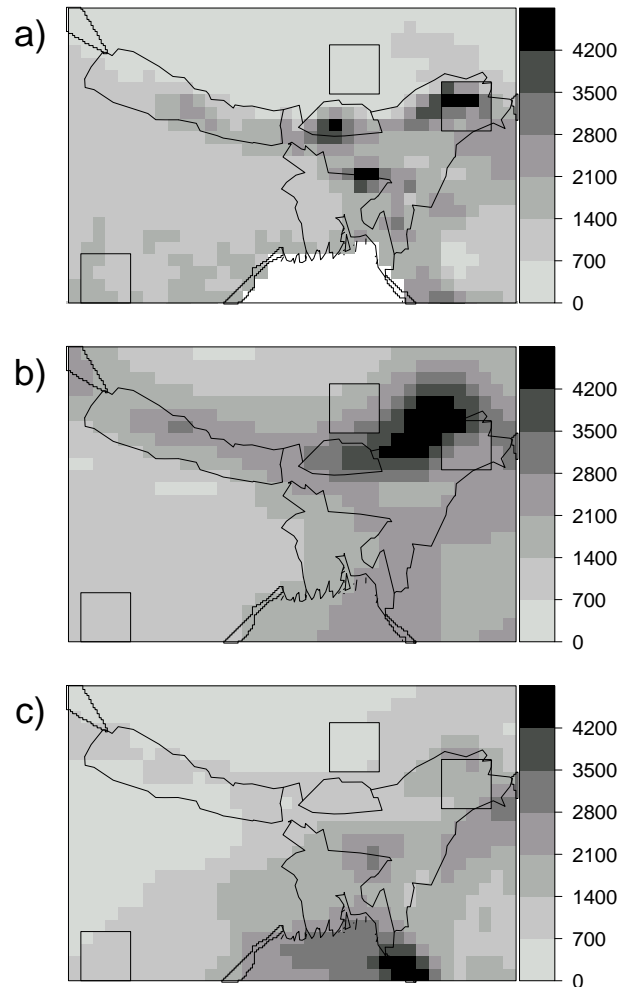
Figure 2.4: As for Fig. 2.3, but for part of the South Asian domain and the observation period 1978-2001.

study) and the number of vertical layers (20 in the present study). In particular, we used prognostic cloud water and diagnostic rain and snow in the parameterization of grid-scale precipitation, and the Tiedtke scheme (Tiedtke, 1989) for convection parameterization. The simulations were initialized in 1958 to avoid spin-up effects, and the whole ERA40 period (1958-2001) was downscaled.

2.5.2   Statistical downscaling with local intensity scaling (LOCI)

Local intensity scaling (LOCI), suggested by Schmidli et al. (2006) for downscaling of GCM precipitation, works on the basis of daily precipitation. The downscaled precipitation is corrected for biases in rain day frequency and rain
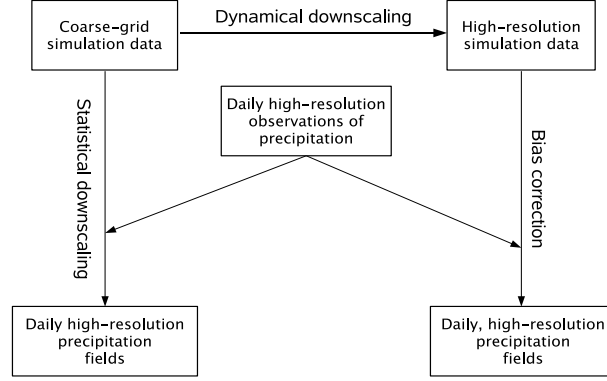
Figure 2.5: Schematic overview of the applied downscaling and bias correction methods.

day intensity. The LOCI algorithm applied in the present study consists of the following four steps:

(1) Bilinear interpolation of model precipitation to the observation grid. Here, our method differs slightly from the original LOCI algorithm, where a simple nearest neighbor interpolation was applied; however, the evaluated statistics are in agreement with the findings of Schmidli et al. (2006) (see section 4.1).

(2) Determination of the model rain day threshold RDT^m such that

$$\frac{|\{P \in P_t^m | P > RDT^m\}|}{|P_t^m|} = \frac{|\{P \in P_t^o | P > 1 \text{ mm/d}\}|}{|P_t^o|},$$

where P is the daily precipitation and P_t^o and P_t^m are observed and interpolated model precipitation series, respectively. The subscript t denotes the training period. Thus, RDT^m is obtained in the training period such that the frequency of the simulated rain days is equal to the frequency of the observed rain days (i.e., days with more than 1 mm/d observed precipitation).

(3) Estimation of the scaling factor

$$\hat{s} = \frac{\overline{\{P \in P_t^o | P > 1 \text{ mm/d}\}} - 1 \text{ mm/d}}{\overline{\{P \in P_t^m | P > RDT^m\}} - RDT^m}$$

as the ratio of the mean rain day intensity of observed to model precipitation during the training period.

(4) Calculation of the final downscaled precipitation:

$$\hat{P} = max\left(0 \text{ mm/d}, 1 \text{ mm/d} + \hat{s} \cdot (P - RDT^m)\right)$$

for all $P \in P_e^m$, where the subscript e denotes the evaluation period. Thus, the difference between the evaluation period model precipitation and model rain

day threshold is multiplied by the scaling factor $\hat{s}$ and added to the observation rain day threshold (1 mm/d). Resulting negative values are set to zero.

The method is applied at every observation grid point. Thus, applying step four to the model training period precipitation series P_t^m instead of P_e^m would yield time series with the same climatological rain day frequency (FRE) and rain day intensity (INT) as P_t^o at every grid point. When applied to P_e^m, one would expect the resulting downscaled precipitation to be more accurate than the coarse-grid precipitation in terms of FRE and INT; however, this is only true if RDT^m and $\hat{s}$ have a similar value in the evaluation and training periods.

2.5.3 Statistical downscaling with gamma distribution mapping (GAMMA)

A two-parameter gamma distribution is commonly used to model observed rain day intensities (Aksoy, 2000), and has previously been used for the downscaling of GCM seasonal forecasts to the station scale (Ines and Hansen, 2006). The distribution is given by

$$\gamma(P) = \frac{1}{\beta^\alpha \Gamma(\alpha)} P^{\alpha-1} e^{-P/\beta}$$

for any rain day intensity of $P \geq 0$ mm/d. The distribution is defined by the shape parameter α and the scale parameter β. The mean and variance of the distribution are given by $\alpha\beta$ and $\alpha\beta^2$, respectively.

As an example, consider one grid cell in the evaluation region CI. Figure 2.6 shows the probability densities of observed rain day intensities above 1 mm/d for this point during the evaluation period 1990-2001, a fitted two-parameter gamma distribution, and a fitted exponential distribution. For the gamma distribution, the estimated parameter values are $\hat{\alpha} \approx 0.6$ and $\hat{\beta} \approx 16.6$ mm/d, and the mean and variance values are 10.7 mm/d and 177.2 $(\text{mm/d})^2$, respectively. For the exponential distribution, these values are 10.7 mm/d and 114.5 $(\text{mm/d})^2$, respectively, whereas for the observations the corresponding values are 10.7 mm/d and 228.8 $(\text{mm/d})^2$.

The local statistical downscaling method presented here, named GAMMA, maps the ERA40 precipitation series to a projected two-parameter gamma distribution at every observation grid point. The first two steps of GAMMA are the same as in LOCI given above. These are followed by:

(3) Reduction of the precipitation series to the amount above the corresponding rain day threshold. For the observations the threshold is 1 mm/d, and for the model precipitation we use RDT^m. The resulting time series are

$$P_t^{o*} = \{P \in P_t^o | P > 1 \text{ mm/d}\} - 1 \text{ mm/d},$$
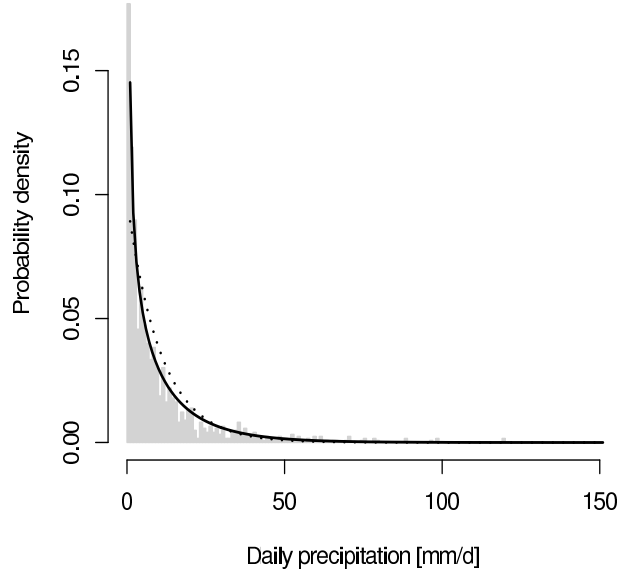$$P_t^{m*} = \{P \in P_t^m | P > RDT^m\} - RDT^m,$$

Figure 2.6: Gamma (solid) and exponential (dotted) distribution fitted to the probability densities of observed daily precipitation above 1 mm/d (gray) for a single grid cell in the evaluation region Central India during the period 1990-2001.

$$P_e^{m*} = \{P \in P_e^m | P > RDT^m\} - RDT^m.$$

(4) Maximum likelihood estimation of the shape (α) and scale (β) parameters $\hat{\alpha}_t^o$, $\hat{\beta}_t^o$, $\hat{\alpha}_t^m$, $\hat{\beta}_t^m$, $\hat{\alpha}_e^m$, and $\hat{\beta}_e^m$ for P_t^{o*}, P_t^{m*}, and P_e^{m*}.

(5) Generation of a gamma distribution projection γ with $\hat{\alpha} = \hat{\alpha}_e^m \cdot \hat{\alpha}_t^o / \hat{\alpha}_t^m$ and $\hat{\beta} = \hat{\beta}_e^m \cdot \hat{\beta}_t^o / \hat{\beta}_t^m$. Thus, the ratio between the two parameters of the new distribution γ and the reduced model precipitation of the evaluation period P_e^{m*} is set to be the same as the ratio between the two parameters of the reduced observation and model precipitation during the training period.

(6) Map the model precipitation to the gamma distribution γ using

$$\hat{P} = F_\gamma^{-1}(F^m(P)) + 1 \text{ mm/d}$$

for all $P \in P_e^{m*}$, where $F^m()$ is the empirical cumulative distribution function (CDF) of the model precipitation and $F_\gamma^{-1}()$ is the inverse of the CDF of the projected gamma distribution γ.

In step (6), mapping is only performed for model precipitation above RDT^m. Below RDT^m, the model precipitation is simply linearly interpolated between 1 and 0 mm/d; however, the total precipitation amount for days with precipitation below 1 mm/d is only 2.5% of the total yearly amount, and the mapping errors for small model precipitation is negligible. The use of an exponential distribution instead of a gamma distribution in mapping the model precipitation yielded a reduction in accuracy (not shown).

2.5.4 Bias correction of CLM precipitation

Both regional and global climate models commonly show model biases in, for example, rain day frequency and rain day intensity. When applying one of the SDMs described above, a bias correction for the coarse-grid precipitation is performed automatically. To correct for the bias of CLM precipitation (i.e., of DDM output), we employ the same algorithms as those used for statistical downscaling. The interpolation step is also carried out, as the model and observation grids are not identical. Both BCMs are carried out at every observation grid point, thereby enabling us to correct the model bias locally; this is advantageous because the CLM bias shows spatial variations (Jaeger et al., 2008).

2.6 Results and discussion

2.6.1 Statistical downscaling of ERA40 precipitation

Both SDMs are applied to all grid points inside the six evaluation regions. As evident in Fig. 2.7, both methods yield a more accurate rain day intensity in the European evaluation regions than the interpolated ERA40 precipitation; this is especially true for the region TIC. ERA40 precipitation was interpolated to the observation grid using the nearest neighbor technique, but bilinear interpolation yields similar results (not shown). The differences between the two SDMs are small for all European regions. The results obtained using LOCI are in agreement with those of Schmidli et al. (2006).
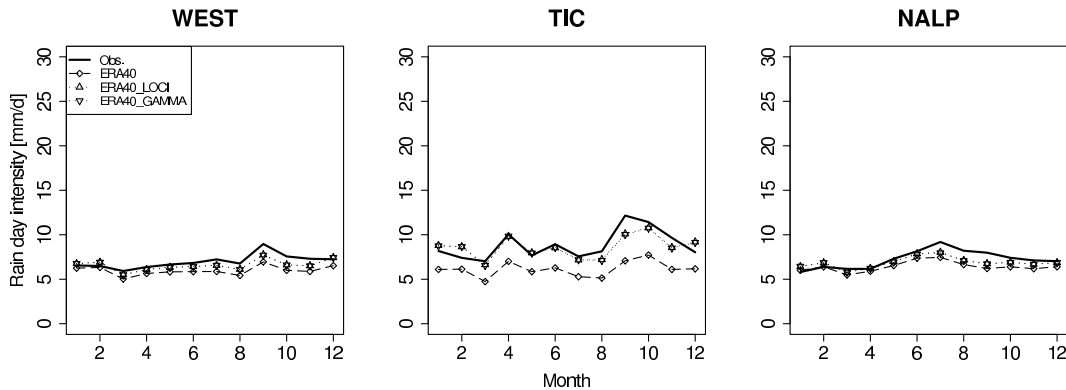

Figure 2.7: Rain day intensity in the European evaluation regions for observations, ERA40, and statistically downscaled ERA40 precipitation by LOCI and GAMMA during the evaluation period.

In the South Asian evaluation regions, the seasonal cycle of the ERA40 simulations and the observations show a number of differences that the SDMs are
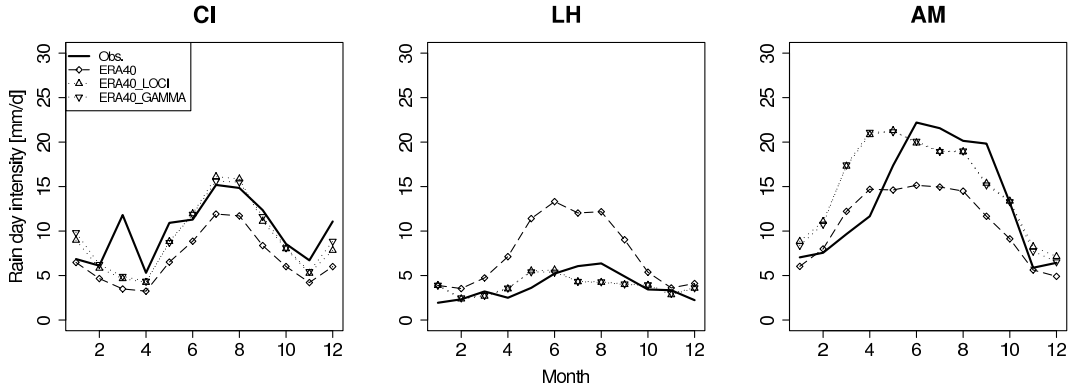
Figure 2.8: As for Fig. 2.7, but for the South Asian evaluation regions.

Table 2.1: List of precipitation properties

Acronym	Description	Unit
FRE	Fraction of days with more than 1 mm/d precipitation	1
INT	Mean precipitation amount on days with more than 1 mm/d precipitation	mm/d
FL90	Fraction of total precipitation above the long-term 90th percentile	1

unable to correct (Fig. 2.8). The differences between the two methods are some-
what larger than those obtained for the European evaluation regions, but remain
very small.

For a more quantitative analysis, we calculate the root mean square errors
(RMSEs) of rain day frequency (FRE), rain day intensity (INT), and heavy rain-
fall proportion (FL90). FL90 is the proportion of total rainfall derived from
events more intense than the 90% quantile. More detailed information on FRE,
INT, and FL90 is provided in Table 2.1. The RMSEs are calculated from the
spatially averaged monthly deviations from the observations and are standard-
ized by division by the observed annual mean. Table 2.2 shows the standardized
RMSEs for the six evaluation regions for the interpolated and statistically down-
scaled ERA40 precipitation. For FRE, the RMSE is reduced in all evaluation
regions except WEST. The two methods yield the same result, as is inevitable
by design: for both statistical methods, the first two steps are the same, meaning
that RDT^m is the same. As RDT^m is not affected by the following steps, FRE
is also unaffected. For INT there is an increase in accuracy in all six regions. In
examining the performance of the two methods concerning INT, LOCI performs
better in WEST and GAMMA performs better in CI; however, the differences
are small, and no clear differences are observed between the two methods for the

Table 2.2: Standardized root mean square errors for ERA40 and statistically downscaled ERA40 precipitation. These errors are calculated from the spatially averaged monthly deviations from the observations. The values are given as part of the observed annual mean in the six evaluation regions for different precipitation properties.

	WEST	NALP	TIC	CI	LH	AM
FRE						
ERA40	0.10	0.13	0.18	0.29	1.67	0.39
ERA40_LOCI	0.11	0.13	0.18	0.26	0.38	0.10
ERA40_GAMMA	0.11	0.13	0.18	0.26	0.38	0.10
INT						
ERA40	0.16	0.14	0.33	0.38	1.21	0.35
ERA40_LOCI	0.09	0.10	0.11	0.25	0.38	0.31
ERA40_GAMMA	0.10	0.10	0.11	0.24	0.38	0.31
FL90						
ERA40	0.07	0.06	0.10	0.31	0.25	0.08
ERA40_LOCI	0.08	0.07	0.09	0.29	0.35	0.09
ERA40_GAMMA	0.07	0.07	0.09	0.25	0.33	0.13

other four evaluation regions. The biggest differences between the two methods can be found in the RMSE of FL90. In this case, GAMMA performs better than LOCI in WEST, CI, and LH. This result was expected, as LOCI simply scales the coarse-grid precipitation with the estimated factor $\hat{s}$, while GAMMA uses two parameter estimates; however, in the evaluation region AM, LOCI performs better than GAMMA. With regard to FL90, the raw ERA40 simulations are slightly more accurate than LOCI in WEST and more accurate than both SDMs in NALP, LH, and AM.

As shown by Hagemann et al. (2005), the ERA40 precipitation strongly overestimates precipitation in the Ganges-Brahmaputra region for the period 1989-2001. This overestimation can also be seen in Fig. 2.8 for LH, which is located in the same region. Furthermore, the relatively high RMSEs of the statistically downscaled ERA40 precipitation in LH can be explained by the changing model bias in the ERA40 data from the training to evaluation periods (Hagemann et al., 2005). The wet bias of the ERA40 data in LH, and especially in AM during spring, as well as the general dry bias in NALP, are also in agreement with the findings of Hagemann et al. (2005).

2.6.2 Dynamical downscaling by the CLM with and without bias correction

Dynamical downscaling by the CLM reproduces the observed INT reasonably well in the European evaluation regions (Fig. 2.9). Comparing Fig. 2.9 with

Fig. 2.7, we see that in TIC the CLM bias is much smaller than the ERA40 bias; in the two other regions it is comparable to the ERA40 bias. Figure 2.10 is the same as Fig. 2.9 but for the South Asian evaluation regions. Here, the CLM experienced major difficulties in representing the observed INT climatologies. For example, the interseasonal variance of the CLM INT bias is much larger in CI than in NALP; the same is true for FRE and FL90 (not shown). However, a comparison of Table 2.3 and Table 2.2 reveals that the overall CLM performance is comparable with that of ERA40 and statistically downscaled ERA40 precipitation. As reported by Beck et al. (2004), it is difficult to improve the high-quality ERA40 precipitation in the European Alps with nested model simulations if compared at the 0.5° scale. In LH, however, the CLM clearly outperforms ERA40; this can be explained by the limitations of the ERA40 data described above.
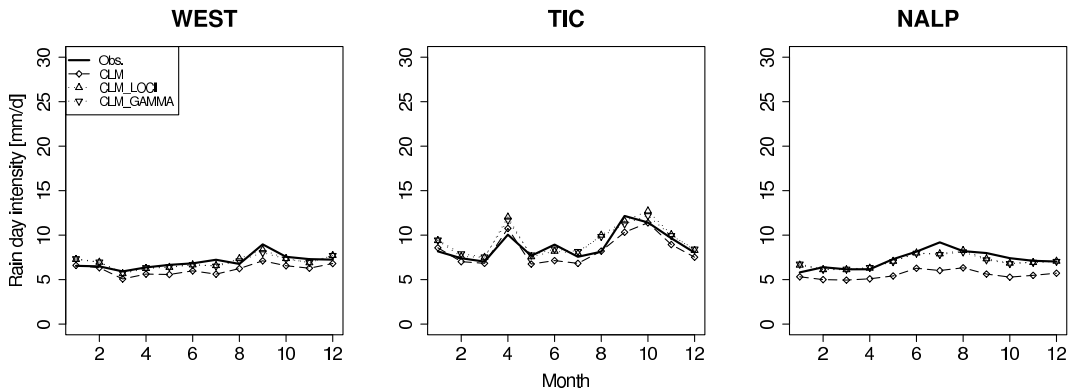

Figure 2.9: Rain day intensity in the European evaluation regions for observations, CLM, and bias corrected CLM precipitation by LOCI and GAMMA during the evaluation period.
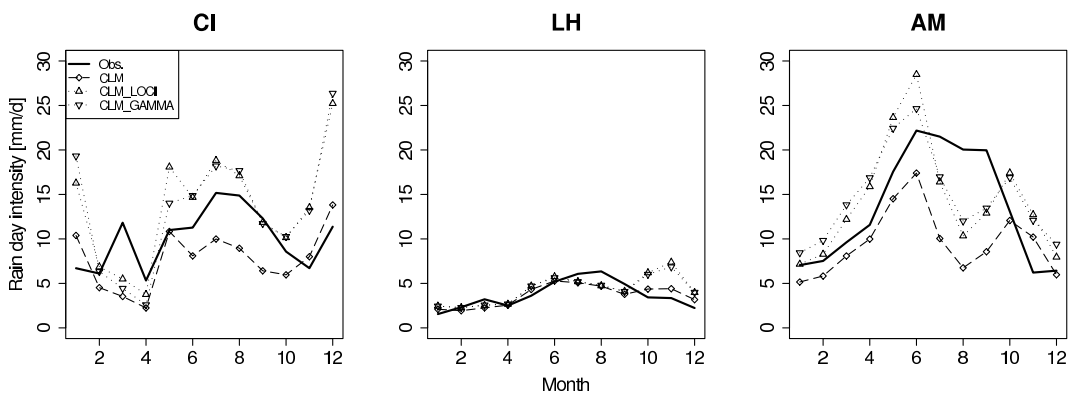

Figure 2.10: As for Fig. 2.9, but for the South Asian evaluation regions.

Both BCMs perform well in Europe (see Fig. 2.9), but the BCMs perform less

Table 2.3: As for Table 2.2, but for CLM and bias corrected CLM precipitation.

	WEST	NALP	TIC	CI	LH	AM
FRE						
CLM	0.21	0.27	0.18	0.42	0.54	0.18
CLM_LOCI	0.06	0.12	0.14	0.43	0.19	0.12
CLM_GAMMA	0.06	0.12	0.14	0.43	0.19	0.12
INT						
CLM	0.14	0.25	0.10	0.42	0.24	0.48
CLM_LOCI	0.07	0.07	0.11	0.61	0.45	0.39
CLM_GAMMA	0.07	0.08	0.10	0.66	0.41	0.35
FL90						
CLM	0.08	0.07	0.06	0.38	0.17	0.23
CLM_LOCI	0.08	0.07	0.06	0.34	0.17	0.31
CLM_GAMMA	0.05	0.06	0.10	0.33	0.18	0.18

well in South Asia. Bias correction increases the CLM INT bias in CI for several months (Fig. 2.10). The statistics provided in Table 2.3 show that in the two European regions WEST and NALP and the South Asian region AM there is a positive impact of GAMMA on INT, FRE, and FL90. Among the three other regions (TIC, CI, and LH) the impact of GAMMA is variable. The performances of LOCI and GAMMA are strongly similar; again, the biggest differences can be found in FL90, where GAMMA shows an overall superior performance. Due to the high interseasonal variance of the CLM bias in CI, training of the BCMs over the entire period is insufficient: both BCMs fail, even in the bias correction of FRE.

The bias corrected CLM precipitation outperforms the statistically downscaled ERA40 precipitation in all European evaluation regions, but the opposite result is obtained for two of the South Asian evaluation regions due to the strong seasonality of the precipitation and its generating processes, which are better reproduced in the ERA40 data. It must be remembered, however, that the CLM is under constant development, and its performance in the South Asian region is expected to improve over time. Because the BCMs use the same methods as the SDMs, the accuracy of the bias corrected CLM precipitation will increase with reduced variation in the CLM bias.

2.6.3 Monthly training for bias correction of CLM precipitation

As shown above, the high interseasonal variance of the CLM bias has a negative effect on the BCMs. Thus, monthly training for the BCMs is tested in

Central India (CI), although seasonal or monthly training raises the potential for overfitting (Schmidli et al., 2006). Figure 2.11 shows a number of positive effects of this procedure (e.g., for March) but also some marked deficiencies (e.g., for November). For each month, the relative CLM INT bias is calculated as the difference between simulated and observed INT divided by observed INT (Fig. 2.12). It is evident that for several months the CLM INT bias changes significantly between the training and evaluation periods. For example, in November the model underestimates the observations during the training period but slightly overestimates them during the evaluation period. This changing bias from the training to evaluation periods resulted in the failure of both BCMs.
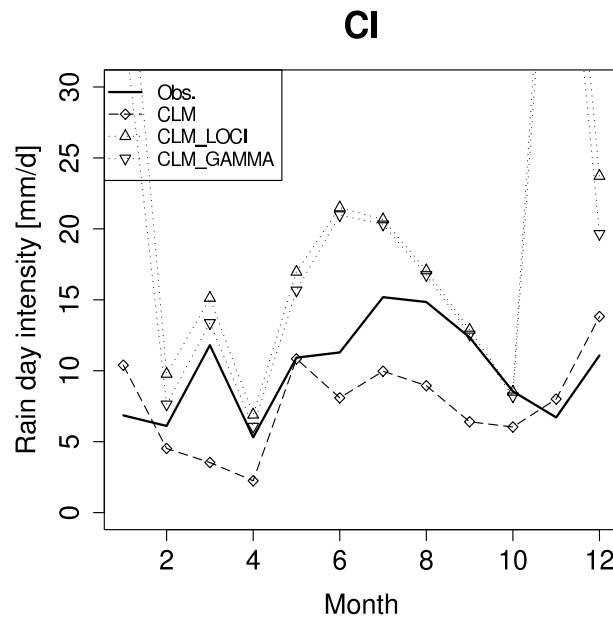

Figure 2.11:   Rain day intensity in the South Asian evaluation region CI during the evaluation period for observations, CLM and, bias corrected CLM precipitation using monthly training.

2.6.4   Bias estimation

The observed change of the CLM INT bias in CI is not purely a problem with model performance: it may also be a statistical artifact due to a small sample size of rain days. Training and evaluation periods of the same length as those employed for Europe would increase the sample size, although not by much. For example, note that for November the total number of observed rain days (spatially averaged over CI) is 22 in the training period and 26 in the evaluation period (not shown). During this training period, the observations show a number of heavy precipitation events (up to 200 mm/d), yet these events are almost completely
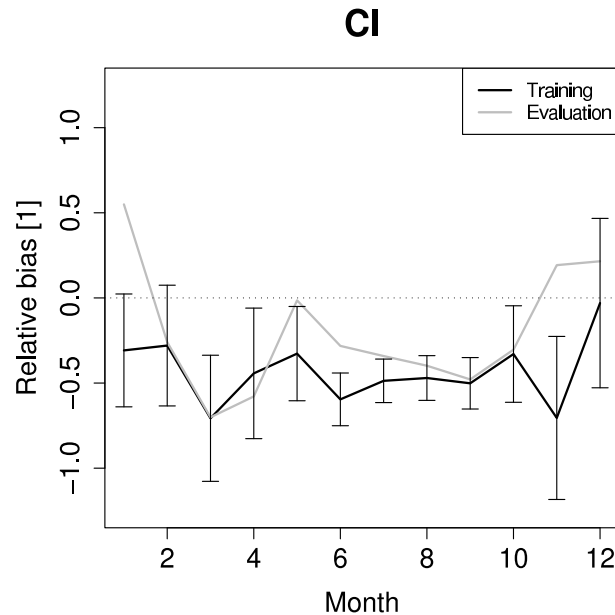
Figure 2.12: Relative rain day intensity bias of the CLM in the South Asian evaluation region CI during the training (black) and evaluation (gray) periods. Bars denote estimations for the 90% confidence interval of the CLM bias.

missing in the evaluation period. This does not appear to be a problem with observational data, as a comparison with CRU TS 2.1 (Mitchell and Jones, 2005) monthly rainfall amounts showed that the monthly sums are comparable. Given the small total number of rain days, however, these extreme events have a major impact on the rain day distribution and INT. In this training period the CLM simulates only 7 rain days and is not able to simulate the extreme events, thereby explaining the observed underestimation. In the evaluation period, however, the CLM simulates 29 rain days and slightly overestimates the observations. With a higher number of rain days the likelihood of changing model bias is expected to decrease. Taking into account all of the rain days for an evaluation region increases the number of rain days under consideration; however, as the events at individual points are not independent, the actual distribution and performance of the BCMs show little change (not shown).

Figure 2.12 shows the uncertainties in the CLM INT bias estimates. The 90% confidence interval is shown for each month of the training period. The intervals for individual months were calculated using Student's t-distribution with $n - 1$ degrees of freedom, where n is the number of observed rain days. The resulting intervals scale with $1/\sqrt{n}$. Note that for a small number of rain days and non-normal distributions these intervals are only approximations; however, similar intervals were estimated using a bootstrap method (Ahrens et al., 2003),

indicating that the confidence intervals are robust (not shown).

For the non-monsoon season (October-May), the uncertainties are large due to the small number of observed rain days, while for the monsoon season (June-September) the uncertainties are relatively small; however, for several months the bias change lies outside the 90% confidence intervals. For these months, the changing model bias is probably partly due to deficiencies in the CLM physics or problems within the observation data set. The same investigation was carried out for the European evaluation region NALP (not shown). In this case, the average, variance, and change of the relative bias are much smaller than in CI; furthermore, the minimum number of observed rain days is higher: all months show at least 100 rain days. Thus, the uncertainties for individual months are small in NALP compared with CI.

2.7 Conclusions

ERA40 simulations were downscaled to the regional scale with two SDMs (LOCI and GAMMA) and a DDM (the regional climate model CLM). Two bias correction methods (BCMs) were also applied to the CLM simulations. The BCMs are based on the same methods as the SDMs. To test the different methods for transferability, they were applied to European and South Asian domains, with each domain containing three evaluation regions.

The performance of the SDMs was related to the intra- and interannual variance of the estimated model bias. In the European evaluation regions, the ERA40 simulations show stationary biases in precipitation that the SDMs are able to correct to a reasonable degree. In the South Asian evaluation regions, the biases of the ERA40 precipitation show a higher seasonal dependency and the SDMs perform less well. This is a major drawback for application of the SDMs on GCM projections, as GCMs are expected to show a bigger intraannual variance of the bias then the ERA40 data. The same holds for the size of the bias: with an increasing bias, the risk of a negative impact of the SDMs also increases.

The main deficiencies of the CLM in the South Asian domain are apparent during the monsoon season, when the CLM underestimates the observed rain day intensity. As shown by Rockel and Geyer (2008), the CLM also highly underestimates the seasonal precipitation in this region during summer (JJA) when the Kain-Fritsch convection scheme (Kain and Fritsch, 1993) and spectral nudging (von Storch et al., 2000) are applied; only an improved parameterization of the cloud and precipitation processes leads to an increase in CLM performance. This finding is not surprising because the model was not designed for this climate region. Nevertheless, the accuracy of CLM precipitation at the 0.5° scale is comparable with that of ERA40 precipitation, and in most places comparable with that of statistically downscaled ERA40 precipitation. The CLM is therefore a promising downscaling method for application on GCM projections. Moreover,

the CLM has an advantage in that it yields a consistent set of different meteorological parameters that can be used, for example, as input to a hydrological model; however, it remains to compare the CLM and SDMs for downscaling of a general GCM. This task will be undertaken in a future study.

LOCI and GAMMA yield similar results in all six evaluation regions, both for downscaling of ERA40 precipitation and bias correction of CLM precipitation. Overall, GAMMA performs slightly better than LOCI when considering the heavy rainfall proportion.

In comparing the different methods, we conclude that the CLM combined with a BCM should be the method of choice for simulations of precipitation in a European domain. In the South Asian domain, however, a high seasonality in the CLM bias and a large uncertainty in the bias estimation for non-monsoon months have negative impacts on bias correction. Thus, based on the current results we suggest the use of CLM precipitation without any BCM in this region, as the risk of a negative impact is too high. The combination of CLM simulation and BCM appears to be less transferable than the CLM itself.

Our results reveal that a reasonable number of rain days in the training period is essential to generate sufficient certainty in the model bias and thus the impact of the statistical methods. We suggest a minimum number of about 500 rain days to ensure a robust estimation of stationary (GCM or CLM) model bias and thereby the successful application of the statistical methods. This requirement limits the application of the statistical methods in dry or seasonally dry climates.

Regarding the general transferability of the methods, we wish to emphasize that this paper focuses only on precipitation modeling in Europe and South Asia. Any other domains and simulated fields (including those from other climate models) are outside of the scope of this work and therefore must be evaluated separately; however, we do plan to analyze the transferability of temperature modeling with the CLM and an optional BCM in the same domains as those of the present study. Note that the statistical methods described above only have an effect on precipitation; the redistribution of water and resulting physical inconsistencies between precipitation and other meteorological fields might have negative impacts in subsequently applied models (Salathé, 2003). The input fields should therefore be used with caution.

Chapter 3

Analysis of the Indian summer monsoon system in the regional climate model COSMO-CLM

3.1   Abstract

The Indian summer monsoon (ISM) influences daily lives and economies in many countries in the South Asian region. This study analyses the representation of the ISM system in the regional climate model COSMO-CLM. Simulations driven by ERA40 re-analysis and present-day (1960-2000) data from the global climate model ECHAM5 are investigated. The ability of the COSMO-CLM to reproduce the ISM better than the coarser-grid driving models is tested using a set of well established, complementary monsoon indices: the all-India monsoon rainfall, vertical wind shear indices and an outgoing longwave radiation (OLR) index. The results show that regarding these large-scale indices the COSMO-CLM simulations are not more accurate than the driving models. Considering the spatial distribution of rainfall, the ERA40-driven COSMO-CLM simulations show major overestimations (about 100%) for the west coast of India, and underestimations (about 50%) for the Himalayan foothills. Large biases occur in the OLR data over the Arabian Sea and the Bay of Bengal where the COSMO-CLM shows high convective activity (OLR $< 180 \, \mathrm{W \, m^{-2}}$) at about three times as many days as observed in the monsoon season. In the ECHAM5-driven simulation underestimations of rainfall appear at the Himalayan foothills, too. Nevertheless, the application of COSMO-CLM to ECHAM5 improves the temporal correlations of the modeled ISM indices, and the spatial patterns are better simulated in the COSMO-CLM with 0.44° horizontal grid-spacing than in the large-scale ECHAM5 data.

3.2   Introduction

The Indian summer monsoon (ISM) has been the subject of numerous scientific studies for more than a century (Walker, 1910; Flohn, 1970; Webster et al., 1998; Gadgil, 2003). Interannual variability in the ISM has a profound impact on society, the environment, agriculture, and the economy, both in India and other countries in the South Asian region. The most obvious impact of the ISM is on rainfall in the monsoon season (June, July, August, and September; JJAS), which accounts for about 75% of the annual precipitation in India.

Kripalani et al. (2007) examined 22 global climate models (GCMs) on the ability to simulate the South Asian summer monsoon precipitation and its variability. They showed that most of the models are able to reproduce the observed annual cycle (with some difference in amplitude), but also showed that simulation of precipitation at regional scales is very difficult. Moreover, Kumar et al. (2006) stated that GCM applications in the Indian region are limited by an insufficient orographical representation of, for instance, the Western Ghats due to their coarse grid resolution (around 200-300 km), and that the use of regional climate models (RCMs) helps to add regional details to the GCM simulations, especially for precipitation.

Parthasarathy et al. (1992) defined the all-India monsoon rainfall (AIMR) index as the total rainfall amount in JJAS averaged over India. Although the interannual standard deviation is only about 10% of the long-term mean, the extremes lead to floods and droughts (Webster et al., 1998; Krishnan et al., 2003). The AIMR index thus provides an important criterion for evaluation of GCMs and regional climate models (RCMs) in this region. However, precipitation in GCMs and RCMs is modeled very late in the process chain and is influenced by many foregoing processes. Thus, indices representing other aspects of the monsoon system allow for a more detailed analysis of the ISM representation in these models and may help to find deficiencies in foregoing model processes.

In the present study, we use the ISM indices based on precipitation, wind, and outgoing longwave radiation (OLR) and their correlations as a tool to investigate possible shortcomings in dynamics and convection parametrization in climate models. The method is applied to investigate if the ISM is better represented in the RCM COSMO-CLM (http://www.clm-community.eu) than in the global re-analysis data set ERA40 (Uppala et al., 2005) from the European Centre for Medium Range Weather Forecasts (ECMWF) or in global simulations done with the coupled atmosphere-ocean climate model ECHAM5/MPIOM (Roeckner et al., 2003; Jungclaus et al., 2006), which are applied as driving data for COSMO-CLM.

We introduce the use of the indices to calculate the degree to which these processes can explain the interannual variability in the AIMR in observations and models. Further, to explore details that are ignored as a consequence of simplifi-

cations inherent in index representation, the spatial distributions of the involved fields are investigated. To assess the question of a better representation of the ISM provided by COSMO-CLM simulations, these explorations also include the driving models. This is motivated by the assumption that a better representation of the ISM leads to more accurate climate projections for the South Asian region.

The remainder of this report includes Section 2, which describes the COSMO-CLM and the setup used in the present study; Sections 3 and 4, which respectively describe the reference datasets and the methods used; Section 5, which presents the results and discussion; and Section 6, which provides conclusions and a brief outlook.

3.3   Model and model setup

The COSMO (COnsortium for Small-scale MOdeling) model is a non-hydrostatic regional model (`http://www.cosmo-model.org`) used by a number of European weather services for numerical weather prediction. The results of this work are based on experiments carried out with the climate version of the model (COSMO-CLM) in a South Asian domain (Fig. 3.1). We have used the model version 2.4.11 which is identical to the current official, evaluated version of the CLM-Community (version 3.2) with exception of two corrections in parts of the model code which have not been used in this work. A detailed documentation of the model, source code, modifications and further information can be found on the CLM web page `http://www.clm-community.eu/`.

The basic differences between the original COSMO model and its climate version are of technical nature and focus on the ability to use dynamical boundary data for soil properties, varying CO_2 concentrations for climate scenarios, a scale-selective relaxation to the boundary data ("spectral nudging") as well as the implementation of a restart possibility. An overview of all changes is given in Böhm et al. (2006).

For our analysis we used data resulting from two types of global forcing: the ERA40 re-analysis data were used to reduce the influence of GCM circulation biases on the RCM output and the ECHAM5 model was used as a more general circulation model. Thus, the COSMO-CLM was driven by (a) ERA40 data with a resolution of $\sim$1.125° (T159) for the period 1958-2000, and (b) by ECHAM5 data with a resolution of 1.875° (T63) for the period 1960-2000. For ECHAM5, run 1 of the simulations for the 4th Assessment Report of the Intergovernmental Panel on Climate Change (IPCC, `http://www.ipcc.ch`) was used (Roeckner et al., 2006a). The run starts in the year 1860, initialized from the preindustrial control run.

In both cases the COSMO-CLM configuration was the same, and the included physical parameterizations are well tested in the European domain (Hollweg et al., 2008; Jaeger et al., 2008; Kothe et al., 2010) and have been successfully applied in
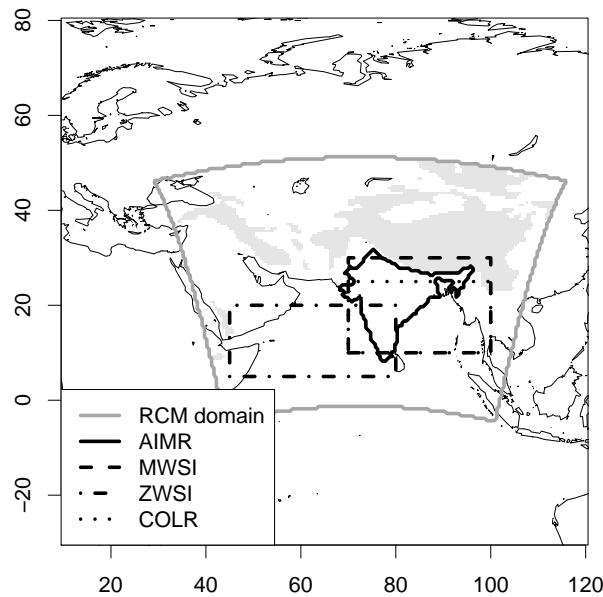
Figure 3.1: Model domain (light gray) and areas used for the calculation of the different indices. Shading indicates the region where the 850 hPa surface is below the model orography.

the South Asian region (Dobler and Ahrens, 2008) before. The simulations were carried out on a 0.44° rotated grid with 20 vertical layers centered on northwestern India (Fig. 3.1). This resolution was chosen due to the fact that we also carried out climate projections up to the year 2100 for different scenarios using the same setup. Thus, a higher spatial resolution was not affordable. Nevertheless, the higher resolution than in ERA40 and ECHAM5 is expected to lead to a better representation of the ISM than in the driving data.

For numerical integration a leapfrog scheme with a time step of 240s was used and no spectral nudging was applied. The applied setup includes a multilayer soil model (Schrodin and Heise, 2002), a radiation scheme following Ritter and Geleyn (1992) and a Kessler-type (Kessler, 1969) microphysic scheme including ice-phase processes for cloud water, rain and snow. The Tiedtke (Tiedtke, 1989) parametrization scheme was used for convection.

3.4   Reference data and indices

A wide range of indices have been defined to measure and predict the strength of the ISM, as reviewed by Wang and Fan (1999). These are based on precipitation (Parthasarathy et al., 1992; Goswami et al., 1999), on the vertical shear over certain pressure levels of zonal winds (Webster and Yang, 1992), (Chen et al., 2007) or meridional winds (Goswami et al., 1999), or on the use of outgoing

longwave radiation as a measure of convection (Wang and Fan, 1999). However, the question of which index best estimates ISM strength remains controversial (Goswami, 2000; Wang, 2000), as is the attempt to represent such a complex phenomenon in a simple index (Wang and Fan, 1999).

All ISM indices in this study were obtained by averaging the corresponding data over particular areas (Fig. 3.1). The AIMR index was calculated as the sum, the other indices as the mean values over the monsoon season JJAS.

The averaging area of the AIMR included all of India with the exception of four hilly meteorological sub-divisions as proposed by Parthasarathy et al. (1992) because of low rain-gauge densities and low areal representation of rain-gauge data in hilly areas. The meridional wind shear index (MWSI) was defined over the area 10°N-30°N x 70°E-100°E, which includes almost all of India, the Bay of Bengal and parts of the Indian Ocean close to the west coast of India. The zonal wind shear index (ZWSI) covered the area 5°N-20°N x 45°E-80°E, which includes the region of the Somali Jet and a large part of the Arabian Sea. Finally, the convection index based on outgoing longwave radiation (COLR) covered the area 10°N-25°N x 70°E-100°E, which is almost the same as the MWSI region.

3.4.1   All-India monsoon rainfall

As reference time series for precipitation we used the homogeneous all-India rainfall data (Parthasarathy et al., 1994) which cover the period 1871-2006. The data are provided as monthly values by the Indian Institute of Tropical Meteorology on their web site `http://www.tropmet.res.in/`.

To investigate the spatial variability of precipitation in the COSMO-CLM model we used the Global Precipitation Climatology Centre (GPCC) full data product version 4 (Schneider et al., 2008) with a spatial resolution of 0.5°. A comparison with the Climate Research Unit time-series version 2.1 (Mitchell and Jones, 2005) and the University of Delaware (UDEL) precipitation dataset version 1.02 (Legates and Willmott, 1990) showed that these three gridded datasets agree well in means of spatial correlations and variability over India as well as with the IITM time series (not shown). Thus, the choice of GPCC as the reference rainfall dataset had no critical influence on our results. The spatial distribution of the GPCC data is shown in Fig. 3.2. The highest values are observed at the north-south oriented west coasts of India, Myanmar (Burma), Thailand and in the Assam region.

3.4.2   Meridional and zonal wind shear

Both wind shear indices were defined as the difference between the lower troposphere winds at 850 hPa and the upper troposphere winds at 200 hPa. The averaging areas for the two wind shear indices were slightly smaller than those originally proposed for the MWSI (Goswami et al., 1999) and the ZWSI (Wang
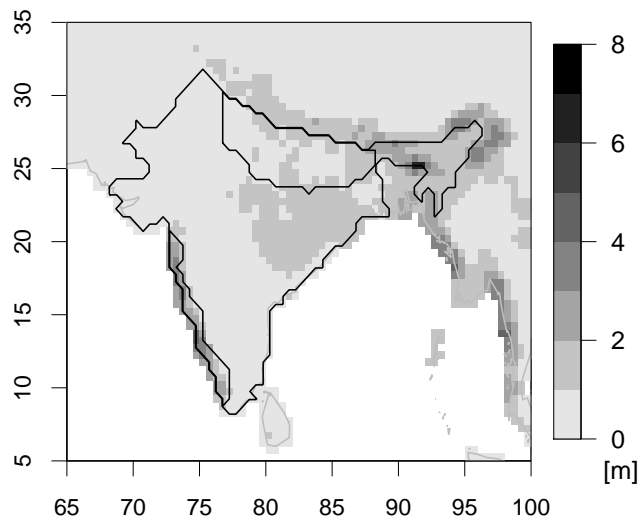
Figure 3.2: Spatial distribution of GPCC mean rainfall in JJAS 1960-2000. The black lines denote the west coast of India, the Himalayan foothills and the AIMR area, respectively.

and Fan, 1999), because of model domain restrictions (Fig. 3.1). As results obtained close to the edge of the model domain can be influenced by boundary effects, no data derived from closer than 3.5° (i.e., eight grid points) from the boundary was used.

Figure 3.1 also denotes the region in which the COSMO-CLM orography is higher than the model's reference atmosphere at 850 hPa. The winds at pressure levels below ground are extrapolated in different ways for different models and should be handled carefully. However, there were only few points within the averaging area of the MWSI in this region (about 9%), and the influence of the extrapolation method on the mean MWSI was assumed to be negligible. Therefore these points were not treated differently.

The reference data used for the 200 hPa and 850 hPa meridional and zonal winds were derived from the National Centers for Environmental Prediction/ National Center for Atmospheric Research (NCEP/NCAR) re-analysis 1 (Kalnay et al., 1996) for the time period 1960-2000. These fields are classified as category A files, which are highly influenced by observations; they are considered to be in the most reliable class of NCEP output variables (Kalnay et al., 1996) and served as pseudo-observations in this study. NCEP re-analysis data were obtained from the Physical Sciences Division of the Earth System Research Laboratory and Office of Oceanic and Atmospheric Research, NOAA web site `http://www.cdc.noaa.gov/` at 2.5° resolution. We used NCEP rather than ERA40 data to ensure data independence as much as possible. However, due to the fact that both NCEP and ERA40 wind fields are based on similar data sources, we do not expect the

COSMO-CLM to perform better than ERA40 in comparison to NCEP data.

An additional index based on the north-south temperature gradient may be defined following the investigations of Goswami et al. (2006): In their work, the mean 200-600 hPa temperature difference between a northern area (15°N-35°N x 40°E-110°E) and southern area (10°S-15°N x 40°E-110°E) was used to derive the monsoon onset. However, correlations between the north-south temperature gradient and the meridional wind sheer index are very high in ECHAM5 (0.99), NCEP and ERA40 re-analyses (0.95 for both). A possible explanation is given in the Appendix A with the help of the thermal wind equation. Due to the high correlation, the index would provide little further insights in model deficiencies. Furthermore, the southern area is not included in the smaller COSMO-CLM domain, and the index was excluded from this study. Nevertheless, it may be useful as a replacement of the vertical wind shear index, if the data are available.

3.4.3 Convection

As a measure of convection we used OLR data from NOAA (Liebmann and Smith, 1996). As shown by Wang and Fan (1999) OLR yields a good estimation of convection in which a low OLR value corresponds to high convective activity. The NOAA data have been corrected for varying satellite equatorial crossing times (Lucas et al., 2001), and covers the period June 1974 to December 1999, with missing data from 17 March 1978 to 31 December 1978. The data are available from the Research Data Archive at `http://dss.ucar.edu` in dataset ds684.1 at NCAR with a resolution of 2.5°.

3.5 Methods

The analysis in this study was based on: 1) the mean values of the indices, 2) the interannual variability of the indices, 3) the spatial distribution of the fields involved, and 4) the representation of the temporal correlations of the indices within the COSMO-CLM, and comparison with observed correlations. Spatial correlations and variabilities were calculated after interpolation to the reference dataset resolution, i.e., 0.5° for precipitation and 2.5° for OLR and the wind fields.

As we were using a model in climate mode, the temporal correlation with observed time series was not of primary interest, contrary to the temporal variability. This was particularly true in the case of forcing of the COSMO-CLM with the ECHAM5 data. For the ERA40-driven simulation the relevance of the temporal correlation is arguable since no spectral nudging was applied and the COSMO-CLM was allowed to develop its own dynamics within the model domain. Therefore, and for the sake of completeness, the values are shown for the ERA40-driven simulations in the following section, but placed in parentheses in Tables 3.1-3.4.

Spatial correlations and variabilities are presented in Taylor diagrams (Taylor, 2001), which are useful for comparing multiple datasets to a reference dataset. The diagrams include correlations, variability values (i.e., standard deviations), and the centered root mean square differences. The variance of AIMR explained by the three other indices was estimated by the coefficient of determination as shown in Ahrens (2003), using a multilinear regression.

3.6 Results and discussion

In the following subsections the results of our analysis of the different ISM indices are shown. For a more detailed analysis, the spatial distributions of the involved fields in the COSMO-CLM are discussed.

3.6.1 All-India monsoon rainfall

Table 3.1 shows the mean values and the standard deviation of the AIMR for the reference data (IITM), the data for COSMO-CLM driven by ERA40 (CLM_{ERA}) and ECHAM5 (CLM_{EC5}), and the driving models for the time interval 1960-2000. The mean value of CLM_{ERA} was closest to the reference, but was very low for CLM_{EC5}. In both COSMO-CLM runs, the interannual variability (measured by the standard deviation) was underestimated. The variability in ERA40 and ECHAM5 was similar to that of IITM, despite lower mean values.

Table 3.1: Mean and standard deviation (sd) of AIMR for different model datasets and correlation (R) of ERA40 and CLM_{ERA} with IITM for the time period 1960-2000.

Data	Mean [mm]	sd [mm]	R
IITM	839	84.5	1
ERA40	701	91.3	0.57
CLM_{ERA}	789	55.7	(0.47)
ECHAM5	684	83.9	
CLM_{EC5}	473	68.6	

The spatial distribution of JJAS rainfall in the two COSMO-CLM simulations and the differences to GPCC are shown in Figs. 3.3 and 3.4. In both simulations, the patterns of high values at the west coasts and in the region around Assam were well reproduced. However, in CLM_{ERA} the rainfall at the west coast of India was much too high, with a maximum overestimation of more than 4000 mm over the four monsoon months (Fig. 3.3). The mean precipitation value on the west coast in CLM_{ERA} was about 4400 mm (Fig. 3.3), compared to 2100 mm

for GPCC (Fig. 3.2) and 1900 mm for CLM$_{EC5}$ (Fig. 3.4). Using data from the meteorological sub-divisions Konkan and Goa, Coastal Karnataka, and Kerala from IITM we calculated a reference value of 2400 mm.
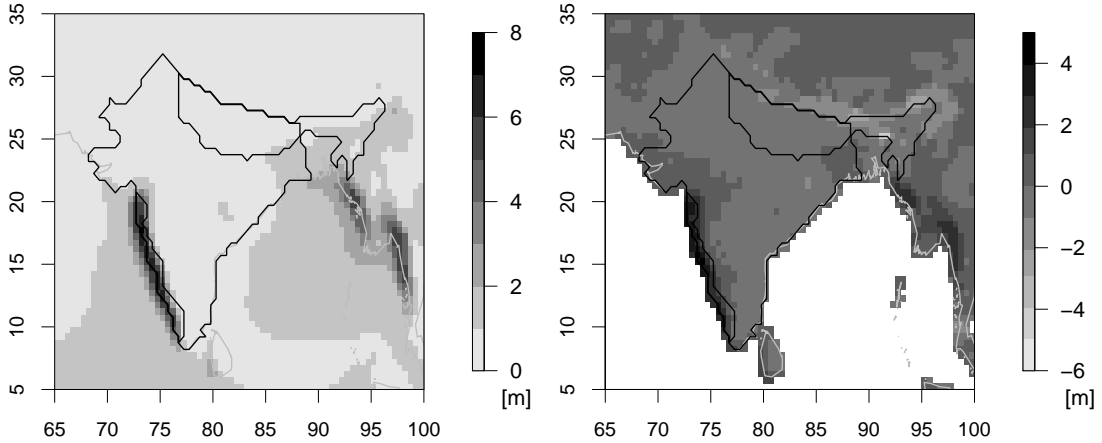

Figure 3.3: As for Fig. 3.2, but for CLM$_{ERA}$ (left) and CLM$_{ERA}$ minus GPCC (right).

In the northern part of India, in the Himalayan foothills (see Figs. 3.3 and 3.4), both runs showed underestimations, with mean values of about 420 mm for the CLM$_{ERA}$ and 340 mm for CLM$_{EC5}$, compared to 900 mm for GPCC. Here, the IITM figures for the average over the sub-divisions Bihar, East Uttar Pradesh, and West Uttar Pradesh is 900 mm. After compensation for errors in the CLM$_{ERA}$ over the whole AIMR area (Fig. 3.3), the mean value was close to that of GPCC.

The spatial correlations with the GPCC data and spatial variabilities of the models are shown in Fig. 3.5. The spatial variability of the JJAS rainfall in CLM$_{ERA}$ was too high (Fig. 3.5); this is related to the over- and under-estimations shown in Fig. 3.3. Further, the spatial correlation with the GPCC data was smaller than in the forcing ERA40 data. These results show that for the spatial distribution of JJAS rainfall over India, CLM$_{ERA}$ provided no additional information relative to ERA40. In contrast, improvements in both spatial correlation and variability were evident in the CLM$_{EC5}$ run compared with the large-scale driving data.

3.6.2   Meridional and zonal wind shear

One reason for shortcomings in the ability of the COSMO-CLM to accurately simulate rainfall over India may be the dynamics of the model. To investigate
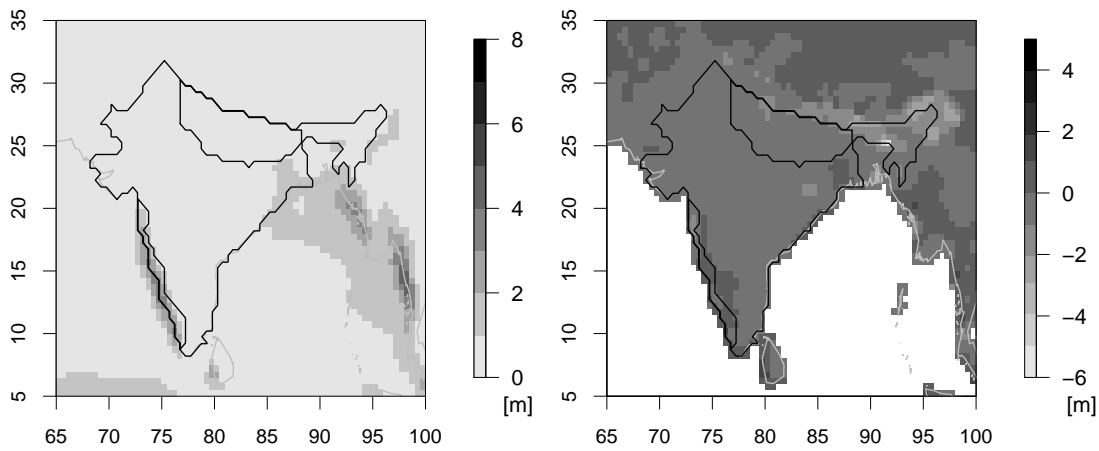
Figure 3.4: As for Fig. 3.3, but for CLM_{EC5}.
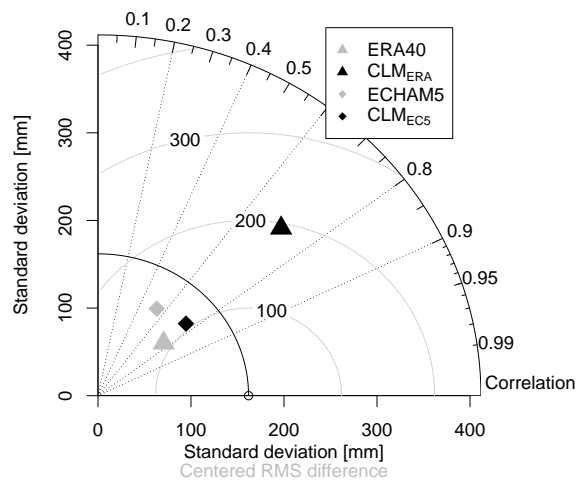
Figure 3.5:   Similarities of the spatial precipitation patterns within the AIMR area between GPCC and different models.

this possibility, vertical wind shear indices were calculated for the period 1960-2000 and compared with indices derived from NCEP data (Tables 3.2 and 3.3). In the ERA40 re-analysis the wind fields are strongly influenced by observation, and were thus expected to be in very good agreement with those of NCEP. Nevertheless, the CLM_{ERA} results were almost as good as those of the ERA40 data.

Overall, the properties of the two dynamic indices in COSMO-CLM were very

Table 3.2: As for Table 3.1, but for MWSI using NCEP as reference.

Data	Mean [m s^{-1}]	sd [m s^{-1}]	R
NCEP	1.90	0.48	1
ERA40	2.19	0.54	0.83
CLM$_{ERA}$	2.35	0.53	(0.73)
ECHAM5	0.85	0.76	
CLM$_{EC5}$	-0.24	0.75	

Table 3.3: As for Table 3.1, but for ZWSI using NCEP as reference.

Data	Mean [m s^{-1}]	sd [m s^{-1}]	R
NCEP	27.4	1.92	1
ERA40	26.4	1.82	0.92
CLM$_{ERA}$	28.3	1.81	(0.81)
ECHAM5	26.3	3.50	
CLM$_{EC5}$	25.0	3.67	

similar to those of the driving model. For instance, in CLM$_{EC5}$ and ECHAM5 the temporal variability of the MWSI and the ZWSI showed large overestimations, and the MWSI was very low, suggesting that the models have difficulty in correctly representing the monsoon Hadley circulation (Goswami et al., 1999). In CLM$_{EC5}$ the mean value over the region was negative.

Figure 3.6 shows the spatial variabilities and correlations with NCEP data for meridional and zonal wind shear within the averaging areas of the different model datasets. To summarize the results in one picture, the datasets were normalized via division by the standard deviation of NCEP for the MWSI and the ZWSI, respectively.

The too high spatial variability in CLM$_{ERA}$ (Fig. 3.6) shows that the good agreement of the mean MWSI and ZWSI with that of NCEP (Tables 3.2 and 3.3) is (as with the AIMR index) mainly caused by compensation for errors over the averaging area. In the CLM$_{EC5}$ however, an added value over ECHAM5 can be seen in the spatial structure, especially in the MWSI, despite the very low mean value and the very great temporal variability (Tables 3.2 and 3.3). This indicates that, in CLM$_{EC5}$, the MWSI and ZWSI errors are distributed homogeneously over the averaging area.

For all models the errors in the 200 hPa meridional and zonal winds were relatively small (data not shown). As the strong zonal winds at 200 hPa account for about two-thirds of the ZWSI these values dominate the index. Thus, the
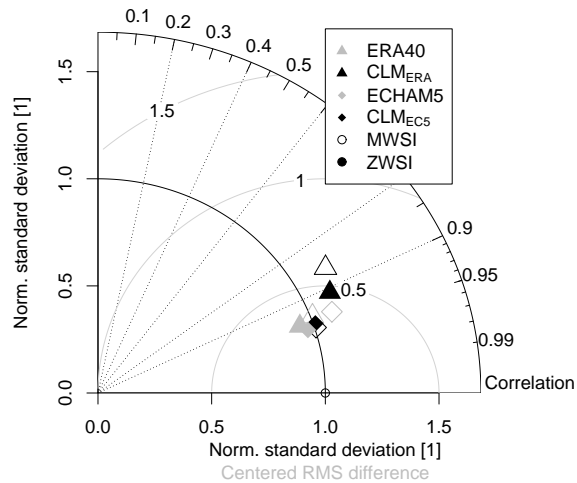
Figure 3.6: Similarities of the spatial wind shear patterns between NCEP and different model datasets within the MWSI (hollow) and ZWSI (solid) area.
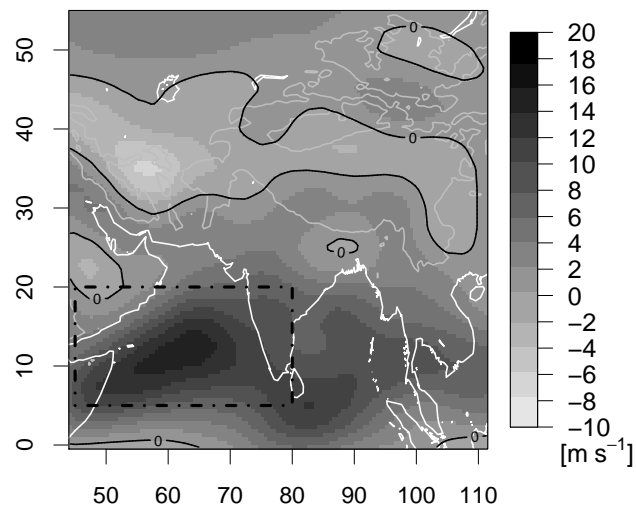

Figure 3.7: Mean NCEP zonal winds at 850 hPa in JJAS 1960-2000. Also shown are the region where the 850 hPa surface is below the model orography (light gray line) and the ZWSI area (dash-dotted).

good agreement with the NCEP mean value provides little information about the lower troposphere dynamics of the models. However, moisture transport toward India mostly happens at the lower levels (Lim et al., 2002). Figure 3.7 gives the

850 hPa zonal winds as provided by the NCEP data. Figures 3.8 and 3.9 show the results form the two COSMO-CLM runs and the differences to the NCEP data. In both simulations the model overestimated westerly winds over the southern part of the Bay of Bengal and large parts of the Arabian Sea, with the maximum overestimation occurring in the Gulf of Aden. However, in the eastern part of the Arabian Sea, close to the west coast of India, the CLM_{EC5} simulation of winds was similar to that of the NCEP, but underestimated winds in the northern part of the coast. In both COSMO-CLM runs orographically influenced wind patterns appeared which are not visible in the coarse resolution (2.5°) NCEP data.
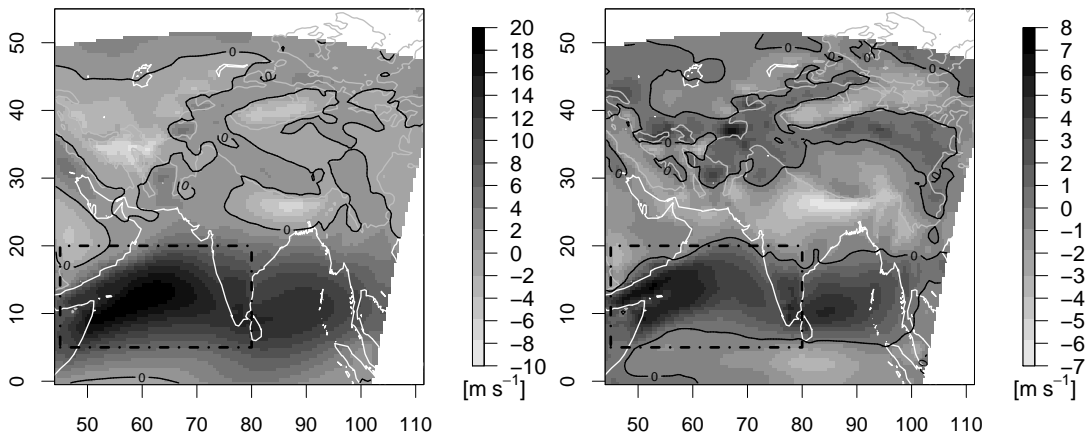
Figure 3.8:   As for Fig. 3.7, but for CLM_{ERA} (left) and CLM_{ERA} minus NCEP (right) zonal winds.

For the meridional winds a good representation of the MWSI in the models is very difficult, as the mean value was only about 2 m s^{-1}. Contrary to the ZWSI, the MWSI was not dominated by the lower or upper level winds, which are of about the same speed (1 m s^{-1}). Thus, even small errors in the field averages (as was the case for CLM_{EC5}) can lead to large deviations in the index (e.g., an error of 1 m s^{-1} could lead to a deviation of 100%). Here, our analysis of the COSMO-CLM bias for single fields revealed no detectable spatial patterns.

3.6.3   Convection

We used OLR data for the period 1974-1999 to measure convection, where low (high) OLR values corresponded to high (low) convective activity. The observed values are shown in Fig. 3.10, where convective regions can be seen over the eastern parts of the Bay of Bengal and the Arabian Sea. Results of the convection index based on OLR (COLR) for the simulations and the NOAA reference data are summarized in Table 3.4. CLM_{ERA} overestimated convection over the target
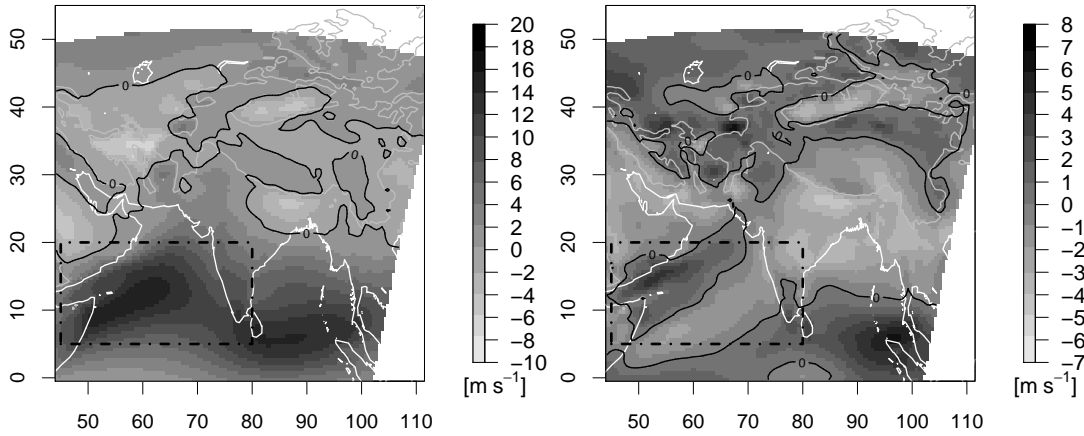
Figure 3.9: As for Fig. 3.8, but for CLM$_{EC5}$.

area, whereas the variability was close to that of the reference. The CLM$_{EC5}$ data showed the opposite behavior. For both driving models the convective activity was too low, and the COSMO-CLM introduced additional convection.

Table 3.4: As for Table 3.1, but for COLR and the time period 1974-1999 using NOAA as reference.

Data	Mean [W m^{-2}]	sd [W m^{-2}]	R
NOAA	209	4.67	1
ERA40	225	3.69	0.72
CLM$_{ERA}$	186	3.87	(0.22)
ECHAM5	218	5.78	
CLM$_{EC5}$	206	8.72	

Figure 3.11 shows the spatial variability of the OLR and correlations with the NOAA OLR data in the various model datasets over the index area. The datasets were interpolated to the coarse resolution (2.5°) of the reference data to make a direct comparison possible. The correlations of the CLM$_{EC5}$, ERA40, and ECHAM5 with the reference data were high, but the spatial variability in all models (except for ECHAM5) was much too high, with the CLM$_{ERA}$ having the greatest values. Overall (i.e., considering also the mean value and temporal variability; Table 3.4), the ECHAM5 model showed surprisingly good agreement with reference data.

Figures 3.12 and 3.13 show the spatial distribution of the OLR in the two COSMO-CLM runs and the differences to the NOAA data. Common features
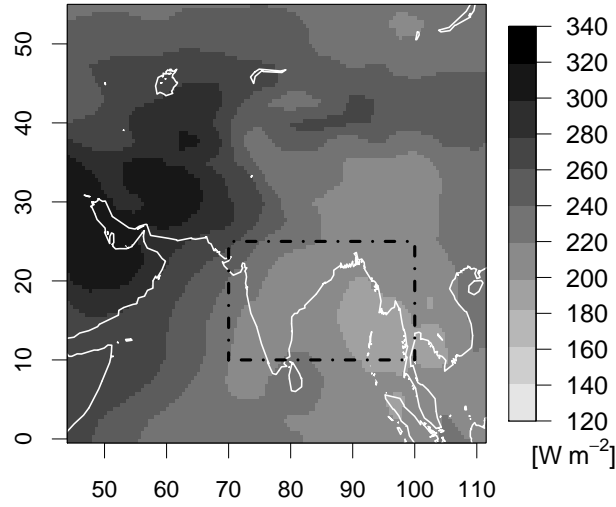
Figure 3.10: Mean NOAA outgoing longwave radiation in JJAS 1974-1999. The COLR area is denoted by the dash-dotted line.
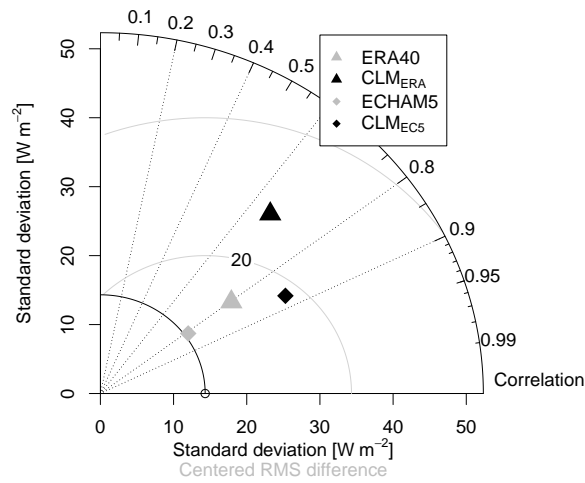
Figure 3.11: Similarities of the spatial OLR patterns between NOAA and different model datasets within the COLR area.

include an overestimation of convection over the west coasts of India, Sri Lanka, and Thailand, and the coasts of Bangladesh and Myanmar (Burma), and underestimation over large parts of India and in the Himalayan foothills. Again, compensation for errors within the COLR averaging area yielded a mean value

for CLM_{EC5} that was close to the reference value.
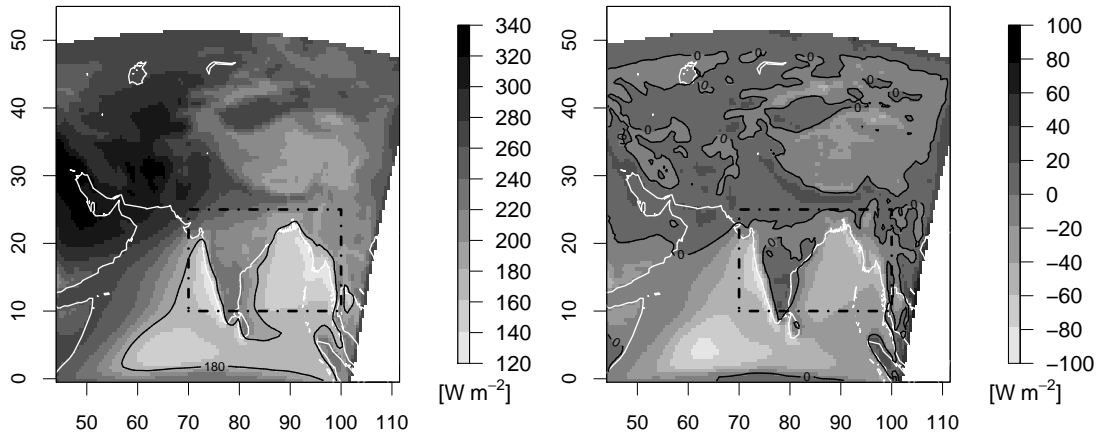
Figure 3.12: As for Fig. 3.10 but for CLM_{ERA} (left) and CLM_{ERA} minus NOAA outgoing longwave radiation (right).
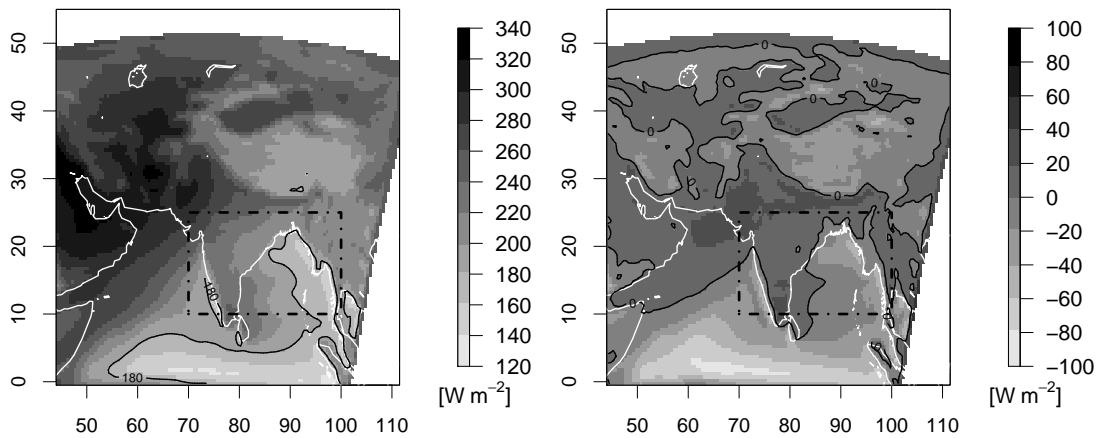
Figure 3.13: As for Fig. 3.12, but for CLM_{EC5}.

CLM_{ERA} underestimated the OLR by more than 70 W m^{-2} for the west coast of India, and by more than 50 W m^{-2} over the Bay of Bengal. The large overestimation of convection in these areas were associated with too many days with high convective activity (i.e., days with an OLR < 180 W m^{-2}). As can be seen in Fig. 3.14, the CLM_{ERA} data showed more than 25 such days per month over the west coast of India, and about 20 such days over the Bay of Bengal; for the NOAA

data the relevant conditions occurred on only about 5-10 days each month, and
for CLM$_{EC5}$ on only 15 days a month (data not shown).
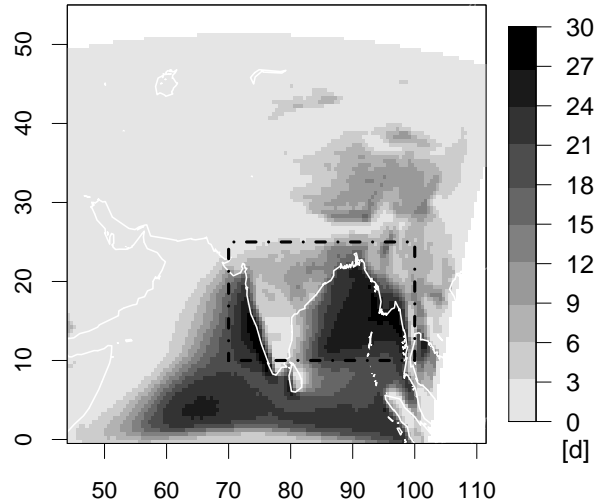
Figure 3.14: Mean number of days per month with OLR < 180 W m^{-2} in
CLM$_{ERA}$ in JJAS 1974-1999.

Calculating the mean OLR only in days with high convective activity, we
found values of about 160 W m^{-2} for the NOAA data and an underestimation of
about 30 W m^{-2} for both CLM$_{ERA}$ (Fig. 3.15) and CLM$_{EC5}$ (data not shown),
indicating that the model simulated high convective activity on too many days.

3.6.4   Index correlations

Table 3.5 shows pairwise temporal correlations of the AIMR, MWSI, ZWSI,
and COLR index, and the variance (R^2) of AIMR explained by the three other
indices for their common time periods. Overall, the ECHAM5 data showed the
strongest intra-model correlations, followed by CLM$_{EC5}$, CLM$_{ERA}$, the reference
datasets, and finally ERA40.

The correlations between the AIMR and wind shear indices in both COSMO-
CLM simulations were close to reference correlations. The ERA40 data showed
correlations that were too low and the ECHAM5 data correlations that were too
high. Thus, the regional model revealed an improvement of both large-scale driv-
ing models in assessing dynamical contribution to the AIMR. An improvement
was also found in the variance of AIMR explained by the other indices (Table
3.5) for CLM$_{EC5}$.

The reference correlations of ZWSI with AIMR and COLR were close to the
values reported by Wang and Fan (1999). However, the correlations with MWSI
determined here differ from the values shown in Wang and Fan (1999). Small
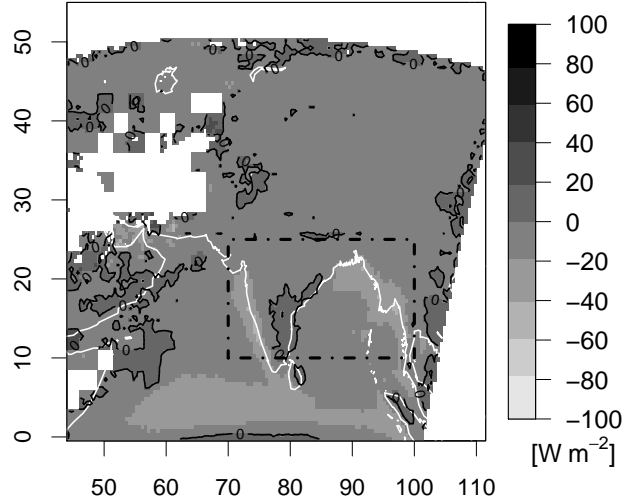
Figure 3.15: Mean CLM_{ERA} minus NOAA OLR in JJAS 1974-1999 for days with OLR < 180 W m^{-2}. White pixels inside the simulation domain are areas with zero days with OLR < 180 W m^{-2}.

Table 3.5: Correlations of the different indices in the reference datasets and the models, and explained variance (R^2) in AIMR by MWSI, ZWSI and COLR.

Data	AIMR& MWSI	AIMR& ZWSI	AIMR& COLR	MWSI& ZWSI	MWSI& COLR	ZWSI& COLR	R^2
Ref.	0.71	0.62	-0.43	0.64	-0.61	-0.61	0.38
ERA40	0.54	0.40	-0.57	0.58	-0.82	-0.63	0.37
CLM_{ERA}	0.65	0.62	-0.75	0.51	-0.61	-0.57	0.59
ECHAM5	0.87	0.81	-0.87	0.63	-0.78	-0.85	0.88
CLM_{EC5}	0.76	0.68	-0.80	0.64	-0.86	-0.81	0.70

differences would be expected because of the use in the present study of different time periods, index areas, and a newly corrected NOAA dataset. The differences are mainly a result of the smaller averaging area used in this study (data not shown). Interestingly, the MWSI index defined in the present study showed a higher correlation with the AIMR than did the index proposed by Goswami et al. (1999) and used by Wang and Fan (1999).

The greatest differences between the models and the reference datasets lay in the anti-correlation of AIMR with COLR (Table 3.5); in all model simulations the anti-correlation was higher than in the reference data. Thus, precipitation over India was overly influenced in models by convection over the Arabian Sea

and the Bay of Bengal.

3.6.5 Influence of sea surface temperature

Our findings above suggest that shortcomings in the COSMO-CLM were largely associated with the parametrization of convection; however, the reasons for overestimation of convective activity over the sea are not clear. Especially, the better agreement of CLM_{EC5} than that of CLM_{ERA} with OLR and rainfall observations is in general contrast to other downscaling studies. A comparison of the two driving datasets revealed large differences in the sea surface temperature (SST), with about 1℃ colder ECHAM5 SST over large parts of the Arabian Sea and the Bay of Bengal (not shown). Note that the SST data are directly fed into the COSMO-CLM, as the model does not include an ocean model on its own.

A short experiment for the years 1958-1965 was carried out to evaluate the impact of the SST difference, replacing SST in the driving ERA40 data with ECHAM5 SST. The reduced SST affected evaporation over sea and led to a better agreement of the rainfall distribution in the 8-year period (not shown).

Alternatively to the artificial reduction of SST, the evaporation over sea can be reduced in the COSMO-CLM model setup (Hollweg et al., 2008). The setup modification decreases the heat fluxes over water and shows the same positive effects as a reduction of SST in the spatial distribution of rainfall and OLR (not shown).

3.6.6 Monsoon and ENSO

The relationship between the El Niño Southern Oscillation (ENSO) and the Indian summer monsoon has been extensively discussed in literature (Walker, 1923; Rasmusson and Carpenter, 1982; Ju and Slingo, 1995). As in our RCM simulations the ENSO region was not wholly included in the domain, we were able to analyse how the boundary information of the ENSO-monsoon relationship was passed from the driving models to the RCM.

Table 3.6 shows the correlations of the JJAS mean of the Niño3.4 index with the AIMR, MWSI, ZWSI and COLR, respectively. We used the Niño 3.4 index as it is better correlated to AIMR than is the Niño 3 index (Gadgil et al., 2004). However, results for the Niño 3 index were found to be similar (not shown). Niño 3.4 and Niño 3 data was obtained from Climate Prediction Center, National Oceanic and Atmospheric Administration, USA (`http://www.cpc.noaa.gov/data/indices`).

As can be seen, the (anti-)correlations between ENSO and all indices were weaker in the COSMO-CLM runs than in the driving models. This had been expected as the Niño 3.4 index was calculated using the data from the driving models only. For the dynamical indices MWSI and ZWSI, the weakening was only small. Similar to AIMR and COLR, the correlation between ENSO and COLR

was in all model simulations higher than in the reference data. However, the weakening of the correlation between ENSO and COLR was much stronger than for the dynamical indices. The variance of AIMR explained by MWSI, ZWSI, COLR and ENSO (Table 3.6) was close to the values given in Table 3.5.

Table 3.6: Correlations of the JJAS mean of the Niño 3.4 index with the different indices in the reference datasets and models. Also shown is the explained variance R^2 in AIMR by MWSI, ZWSI, COLR and Niño 3.4.

Data	AIMR	MWSI	ZWSI	COLR	R^2
Ref.	-0.5	-0.49	-0.67	0.29	0.39
ERA40	-0.32	-0.54	-0.68	0.59	0.39
CLM$_{ERA}$	-0.28	-0.42	-0.61	0.36	0.60
ECHAM5	-0.59	-0.40	-0.70	0.64	0.88
CLM$_{EC5}$	-0.36	-0.33	-0.66	0.43	0.70

3.7   Conclusion and Outlook

We analysed the representation of the Indian summer monsoon (ISM) in the regional climate model (RCM) COSMO-CLM in comparison to its larger-scale driving data. For this purpose, two simulations, one driven by ERA40 re-analysis data, the other by the global climate model (GCM) ECHAM5/MPIOM were used.

In a first step, the representation of the ISM was investigated using indices based on precipitation, vertical wind shear and outgoing longwave radiation. These indices are mainly measures of the large-scale phenomena associated with the ISM. We expected the COSMO-CLM to perform better than the large-scale data, as for instance the orography of the Tibetan Plateau was better represented in the RCM due to the higher resolution. However, our results showed, that the COSMO-CLM was not able to improve the ISM representation with respect to means and temporal variability of most indices.

But, an evaluation of models based only on the discussed ISM indices is incomplete, as errors may compensate for each other, resulting in an areal average in good agreement with reference data sets. Thus, we included the spatial distributions of the various fields involved in index calculations in our analysis. This showed that the COSMO-CLM was generally able to reproduce the observed spatial rainfall patterns, but tended to overestimate precipitation over the west coast of India, and to underestimate precipitation over large areas of India, especially in the Himalayan foothills. When applied to ERA40 data the COSMO-CLM

showed no overall improvements in the spatial distribution of precipitation over India, vertical wind shear or outgoing longwave radiation, either.

Contrary, the COSMO-CLM was able to improve the spatial patterns for precipitation and vertical wind shear when using ECHAM5 driving data. Thus, downscaling of large-scale ECHAM5 data yielded additional information that is necessary for regional utilization of results (Beck et al., 2004). This is a promising result consistent with the findings of Hagemann and Jacob (2007) that RCMs can compensate problems of the driving GCM on the local scale. Thus, the analysis of various climate projections using ECHAM5 driven COSMO-CLM simulations is planned. The substantially different results of the two simulations in relation to the driving data imply that it is difficult to assess the added value of dynamical downscaling of re-analyses, as in re-analyses the problems on the local scale can be compensated by the assimilation of observational data.

The principal deficiencies of the model were located in the parametrization of convection. The simulations showed too much of convective activity near the west coast of India. For the dynamical properties, the COSMO-CLM showed good agreement with NCEP re-analysis data in terms of 200 hPa zonal and meridional winds. However, when driven by ERA40 data, the model tended to simulate westerly winds that were too strong at 850 hPa over the Arabian Sea and the Bay of Bengal. This may be another explanation for the overestimates of precipitation on the west coast of India, as stronger winds are associated with enhanced moisture transport towards land. A model sensitivity study showed that the atmosphere-ocean interaction is a key factor for a good model performance in this region. Further investigations and developments in this area or the coupling of the COSMO-CLM to an ocean model could lead to significant improvements.

In both COSMO-CLM simulations, the correlations of the all-India monsoon rainfall (AIMR) with the wind shear indices were more accurate than in the driving models. For the correlation of AIMR with the convection index and the variance of AIMR explained by the other indices we found high values in the ECHAM5 and the COSMO-CLM model. As shown by Patra et al. (2005), the interannual variability in aerosol content over the Indian subcontinent can have a significant influence on the AIMR. As the applied ECHAM5 and COSMO-CLM model versions did not include an aerosol microphysics component, other explaining parameters like aerosol variability were not well represented. This, to some part, may have led to the too strong correlations in the models.

We conclude that the transfer of a RCM to different regions is not straight forward and needs severe testing before application. With this work we have proposed a framework which may help in finding an accurate setup for RCM simulations in the region of the ISM. In a future study we will test the transferability of our methods to other monsoon systems (for instance the West African monsoon).

3.8 Appendix

Based on the work of Goswami et al. (2006), a temperature based ISM index can be defined taking the mean 200-600 hPa temperature difference between 15°N-35°N x 40°E-110°E and 10°S-15°N x 40°E-110°E averaged over JJAS. This index however, is highly correlated to the meridional wind sheer index. This may be expected, since a horizontal temperature gradient and a vertical geostrophic wind shear can be related by the thermal wind equation

$$-\frac{\partial \mathbf{v}_g}{\partial p} = \frac{R}{pf}\mathbf{k} \times \nabla_p T$$

where p is the pressure, $\mathbf{v}_g = (U_g, V_g, 0)^T$ the geostrophic wind vector, f the Coriolis parameter, R the gas constant for air, $\mathbf{k}$ the vertically directed unit vector, T the temperature and ∇_p the isobaric del operator. Thus, the vertical shear of the meridional geostrophic wind $-\frac{\partial U_g}{\partial p}$ is proportional to the north-south isobaric temperature gradient $\frac{\partial T}{\partial_p y}$.

Chapter 4

Four climate change scenarios for the Indian summer monsoon by the regional climate model COSMO-CLM

4.1   Abstract

This paper discusses projections of the Indian summer monsoon (ISM) for the time period 1960-2100 by the regional climate model (RCM) COSMO-CLM. The RCM simulations follow four different future greenhouse gas emission scenarios (SRES A2, A1B, B1 and commitment) and are driven by the global atmosphere-ocean model ECHAM5/MPIOM. To quantify the evolution of the ISM, the all-Indian monsoon rainfall (AIMR) index, two vertical wind shear indices and an estimation of convection via outgoing longwave radiation is used.

The COSMO-CLM simulations show significantly decreasing future ISM trends in all indices for the scenarios A2, A1B and B1. Parts of north-western India are projected to face a decrease in rainfall during the monsoon season of over 70% within this century. For the wind shear indices, the projected decrease is shown to be mainly due to changes in the upper troposphere winds at 200 hPa. At 850 hPa, the changes are limited to decreasing westerlies of 20% to 30% at the southern parts of the Arabian Sea and the Bay of Bengal. The ECHAM5/MPIOM shows similar results for all indices except for the AIMR. Here, the ECHAM5/MPIOM shows positive trends in all scenarios. Considering that COSMO-CLM and ECHAM5/MPIOM overestimate currently observed low predictability values of AIMR, but with a lesser overestimation by the regional model, and that a simultaneous evolution of the ISM indices is more consistent with long-term index correlations than opposite trends, we conclude that the COSMO-CLM is able to add value on the global ISM projections.

4.2 Introduction

Daily live, agriculture yields and profitability in many countries in the South Asian region are highly influenced by the Indian summer monsoon (ISM). About 75% of the yearly amount of rainfall falls during the monsoon season (this is, from June to September) providing water that is necessary for irrigation, electric power production and drinking water. The yearly amount of rainfall during the monsoon season has a strong influence on the economy of the South Asian region. A variety of indices have thus been defined to measure and to predict the yearly variations and future developments of the monsoon's strength. The most commonly used indices are based on rainfall (Parthasarathy et al., 1992; Goswami et al., 1999), the vertical wind shear over certain pressure levels (Webster and Yang, 1992; Chen et al., 2007; Goswami et al., 1999) or the estimation of convection (Wang and Fan, 1999) in certain areas. While all of these indices are correlated by some degree to each other, there is no single best index in estimating the ISM strength (Wang and Fan, 1999; Goswami, 2000; Wang, 2000).

This study gives an overview of the transient projections of different ISM indices by the regional climate model (RCM) COSMO-CLM for the time period of 1960-2100. As a small ensemble of possible future developments, the scenarios A1B, B1, A2, and the commitment scenario as given in the IPCC Special Report on Emissions Scenarios (SRES, Nakicenovic and Swart, 2000) have been used here. This paper focuses on future climate projections and the ability of the RCM to provide an added value to the ISM projections of the driving global model. The ability of the COSMO-CLM to represent the ISM during the time period of 1960-2000 has been evaluated in a previous study (Dobler and Ahrens, 2010).

Most earlier studies on the topic of ISM projections (e.g., IPCC, 2007b; Annamalai et al., 2007) are based on general circulation model (GCM) simulations. While the GCMs already provide some insight in the large-scale trends, the spatial distribution of the fields involved can be better resolved by the application of RCMs. Furthermore, there are indications that RCMs are able to resolve climate extremes better than GCMs (e.g., Duffy et al., 2003).

Thus, due to the increasing availability of computational power, RCM projections have become a popular tool for investigating the fine-scale behavior of the climate system in reaction to enhanced greenhouse gas emissions (e.g., Giorgi, 2006; Kumar et al., 2006; Ashfaq et al., 2009). However, most of these studies are limited to time-slice experiments, simulating about 30 years in the late 20th and 21st centuries, or include one emission scenario only.

4.3 Model and model setup

The COSMO-CLM is a non-hydrostatic regional climate model (RCM) based on the COSMO (Consortium for Small-scale Modeling) model (`http://www.cosmo-model.org`), which is currently used by seven European weather services for their operational numerical weather prediction (NWP). In this work, we applied the COSMO-CLM (version 2.4.11) in a South Asian domain (Fig. 4.1) to simulate regional climate projections within the time period between 1960-2100. Details on the model can be found on the CLM web page `http://www.clm-community.eu/`. The main differences between the NWP and RCM version are given in Böhm et al. (2006).
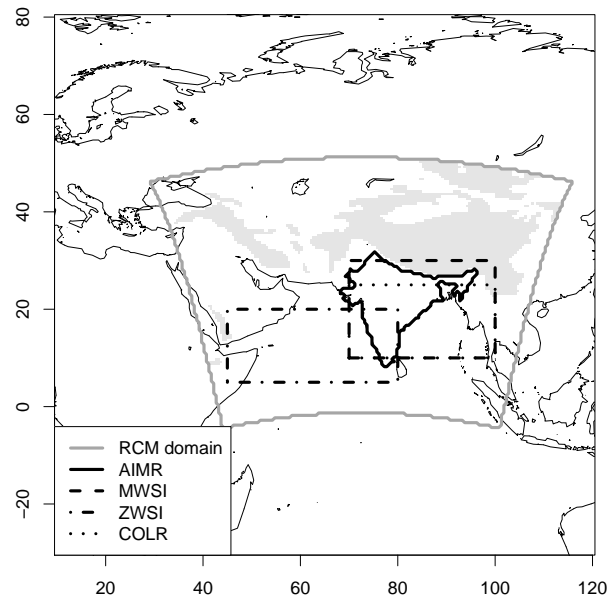
Figure 4.1: Simulation domain and the areas used for the different indices. The gray region denotes the area where the 850 hPa surface is below the model orography.

The lateral boundary conditions were provided by the atmosphere-ocean general circulation model ECHAM5/MPIOM which has a resolution of 1.875° (T63). The COSMO-CLM simulations were carried out on a 0.44° rotated grid with 20 vertical layers. Due to the transient simulation of four different scenarios from 1960 to 2100, a higher resolution was not affordable.

Although the COSMO-CLM configuration includes physical parametrizations that are mainly tested in European domains (Hollweg et al., 2008; Jaeger et al., 2008; Kothe et al., 2010), Dobler and Ahrens (2010) showed that, by using the same setup, the model is still able to improve the spatial distribution of precipitation and wind shear as compared to the ECHAM5/MPIOM driving data in

the South Asian region. The model parametrizations include a radiation scheme following Ritter and Geleyn (1992), a Kessler-type (Kessler, 1969) micro-physic scheme with ice-phase processes for cloud water, rain and snow, the Tiedtke (Tiedtke, 1989) convection scheme and a multilayer soil model (Schrodin and Heise, 2002). Numerical integration was done by a leapfrog scheme using a time step of 240s.

4.4   Indian summer monsoon indices

The analysis of trends in the projections of the ISM was carried out for a set of indices. These indices were obtained by averaging the model data over the areas shown in Fig. 4.1 and the monsoon months from June to September. To make the single indices comparable, we standardized the time series with respect to the reference period of 1971-2000. The index approach provides good information on the projected ISM strength but masks the spatial distribution of the projected changes. Therefore, our analysis also includes the linear trends for the fields involved in the index calculations at the single model grid points.

4.4.1   All-India monsoon rainfall

The all-India monsoon rainfall (AIMR) index was defined by Parthasarathy et al. (1992) as the total rainfall amount from June to September over India excluding four hilly meteorological sub-divisions. Its inter-annual standard deviation is about ten per cent of the long-term average only. Nevertheless, severe floods or droughts have been observed in years with high (low) values (Webster et al., 1998; Krishnan et al., 2003). A long-time series of observational data for the homogeneous all-India monsoon rainfall (Parthasarathy et al., 1994) is available for the years 1871-2009 by the Indian Institute of Tropical Meteorology at `http://www.tropmet.res.in/`.

4.4.2   Meridional and zonal wind shear

The wind shear indices were calculated as the difference between the lower troposphere winds at 850 hPa and the upper troposphere winds at 200 hPa. The meridional wind shear index (MWSI) was calculated over 10°N-30°N x 70°E-100°E. This area includes almost all of India, the Bay of Bengal and a part of the Indian Ocean close to the west coast of India. The zonal wind shear index (ZWSI) was obtained over 5°N-20°N x 45°E-80°E including the region of the Somali Jet and a large part of the Arabian Sea.

Because of the model's domain size, the two wind shear averaging domains (Fig. 4.1) were slightly smaller than the original domains given in Goswami et al. (1999) and Wang and Fan (1999). To reduce boundary effects, no data within 3.5°

(i.e., eight grid points) distance from the boundary was used. Furthermore, winds extrapolated to pressure levels below the ground should be handled carefully. The region where the COSMO-CLM orography is higher than the model's reference atmosphere at 850 hPa is shown in Fig.4.1. However, only about nine per cent of the grid points within the MWSI area are in this region, and the effects on the overall MWSI are negligible (not shown). Thus, these points were not treated specially.

The reference wind data for the time period of 1948-2009 at 200 hPa and 850 hPa were taken from the National Centers for Environmental Prediction/National Center for Atmospheric Research (NCEP/NCAR) reanalysis 1 (Kalnay et al., 1996). The wind fields in NCEP are highly influenced by observations and are in the most reliable class of output variables (Kalnay et al., 1996). NCEP reanalysis data were obtained from the NOAA/OAR/ESRL PSD (Boulder, Colorado, USA) web site `http://www.cdc.noaa.gov/` at 2.5° resolution.

4.4.3 Convection

A convection index based on outgoing longwave radiation (COLR) was defined over 10°N-25°N x 70°E-100°E, which is similar to the MWSI averaging area. As shown by Wang and Fan (1999), outgoing longwave radiation (OLR) yields a good estimation of convection in which a low OLR value (in upward direction) corresponds to high convective activity. To simplify the comparison to the other indices, we used downward directed OLR. Thus, a low value corresponds to low convective activity.

Observational data were taken from NOAA (Liebmann and Smith, 1996). The data are corrected for varying satellite equatorial crossing times (Lucas et al., 2001). As these data are satellite-based, they cover the time period of June 1974 to December 1999 only, with missing data from 17 March 1978 to 31 December 1978. The data was provided by the Research Data Archive at `http://dss.ucar.edu` in dataset ds684.1 at NCAR with a resolution of 2.5°.

4.5 Results

For a detailed analysis of the different ISM indices as observed and simulated by the COSMO-CLM and the ECHAM5/MPIOM for the time period of 1960-2000, we refer to Dobler and Ahrens (2010). In the following subsections, we show the results of climate projections over the time period of 1960-2100 considering the same indices.

4.5.1 Rainfall

Figure 4.2 shows the 21-year running means of the standardized AIMR. There are large long-time variations in the observations and projections, and the negative trend observed in the past 50 to 60 years is within the natural variability. However, there is clear evidence of a low AIMR by the end of the 21st century in the higher-emission scenarios of A1B and A2 in the COSMO-CLM. In the B1 scenario, the projected decrease at the end of the time series is less pronounced. Contrary to the COSMO-CLM, the ECHAM5/MPIOM shows an increase in AIMR for all scenarios by the end of the 21st century.
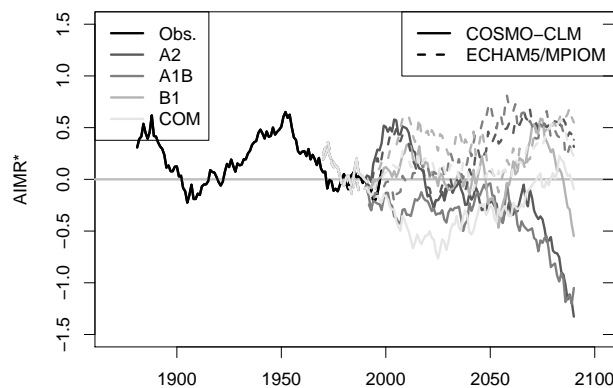
Figure 4.2: Centered 21-year running means of the standardized AIMR index for observation data, COSMO-CLM (solid lines) and ECHAM5/MPIOM (dashed) projections according to different SRES scenarios.

The very low AIMR values at the end of the COSMO-CLM projections are a result of a decrease in monsoon precipitation throughout most of India. Figure 4.3 gives the distribution of the linear trends of monsoon precipitation in the South Asian region according to the A2, A1B and the B1 scenario. Especially in the north-western parts of India and the adjacent regions, a significant decrease is projected. For A1B and B1, the drying pattern is similar to A2, but with reduced amplitudes in accordance with the overall AIMR trend. Furthermore, there is some increase in monsoon precipitation at the south-eastern edge of the Indian peninsula. The commitment scenario shows almost no significant trends (not shown). Although it is clear from Fig. 4.2 that the assumption of linear trends in the monsoon precipitation is a simplification, it is helpful to summarize the projected trends and their statistical significance.

The changes in the rainfall climatology in the COSMO-CLM projections from the time period of 1971-2000 to 2071-2100 are shown in Fig. 4.4. Although there is a reduced annual rainfall in all scenarios, an increase of October and post-monsoon season precipitation (October and November) can be seen in all scenarios.
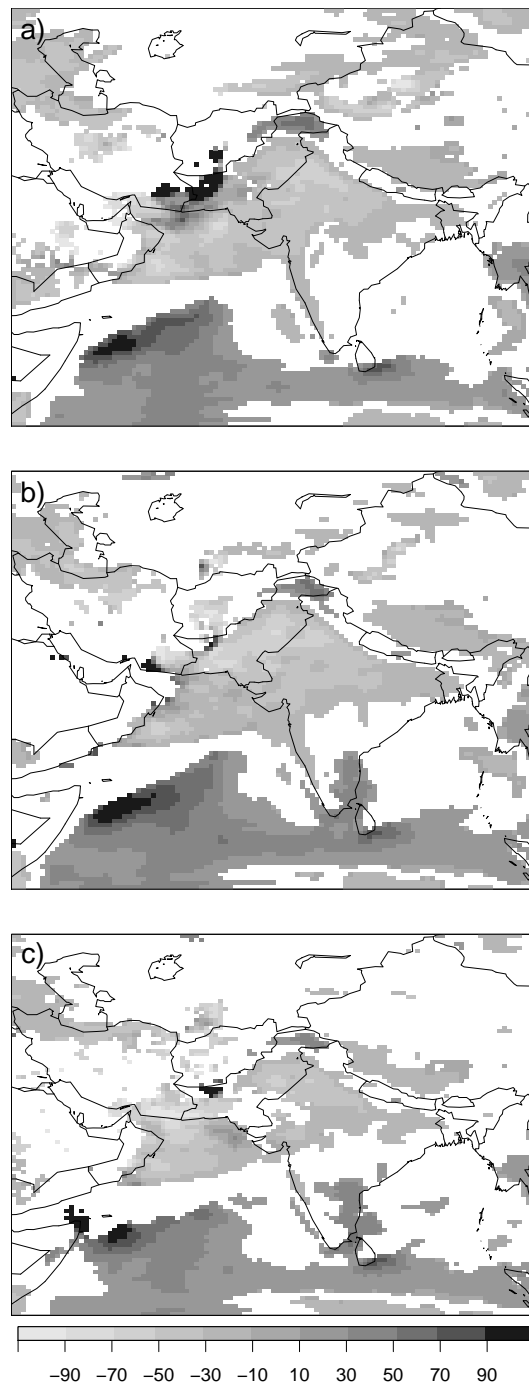
Figure 4.3: Linear trends in monsoon rainfall (%/cent.) during the time period 1960-2100 in a) the A2, b) the A1B and c) the B1 COSMO-CLM run. Colored areas show significant trends (at the 5% significance level).
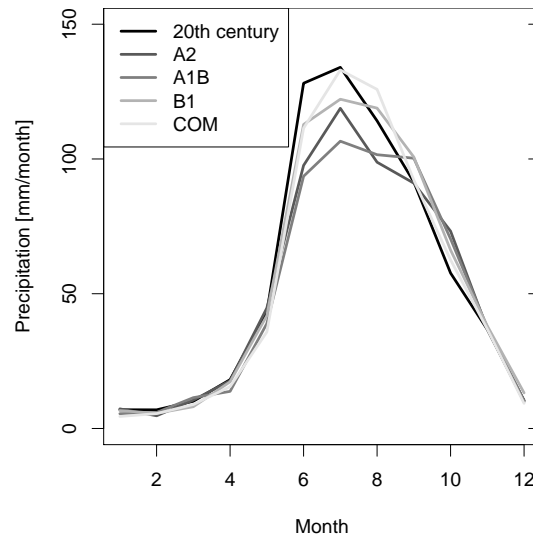
Figure 4.4: Annual cycle of monthly precipitation in the time periods 1971-2000 and 2071-2100 for the different COSMO-CLM scenario runs.

4.5.2 Wind shear

The 21-year running means of the standardized MWSI and ZWSI are shown in Figs. 4.5 and 4.6, respectively. For the MWSI, the long-time variations and trends are similar to the AIMR index (Fig. 4.2) in the COSMO-CLM runs. For the ZWSI, the variations are much smaller, and the decreasing trends in the A2 and A1B scenario are striking. In the single scenarios, there is a high agreement in the temporal evolution of the wind shear indices and the AIMR index.
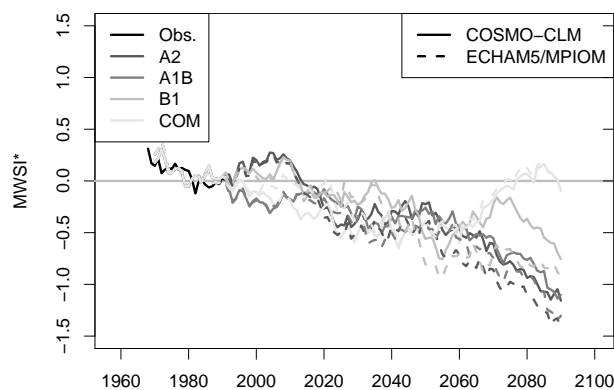
Figure 4.5: As for Fig. 4.2, but for the meridional wind shear index.

While the observations show a negative trend for MWSI (Fig. 4.5) in accordance with the observed AIMR trend over the past 60 years, no trend can

be seen in the corresponding ZWSI (Fig. 4.6). The differences between the
ECHAM5/MPIOM and COSMO-CLM projections are larger in the MWSI than
in the ZWSI, especially in the B1 scenario. However, as for the COSMO-CLM,
the trends in both wind shear indices in the ECHAM5/MPIOM projections are
negative for the A2, A1B and B1 scenario.
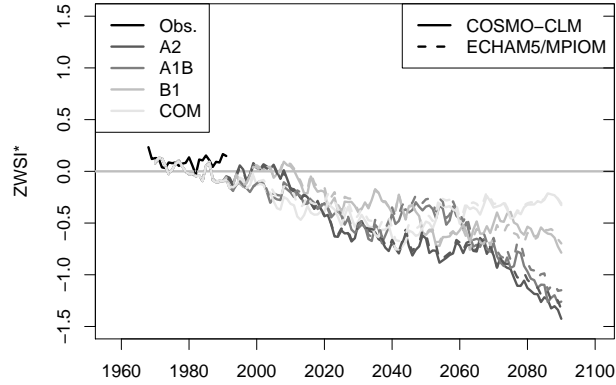
Figure 4.6: As for Fig. 4.2, but for the zonal wind shear index.

The spatial distributions of the horizontal wind fields in the COSMO-CLM,
averaged over the monsoon season from 1971 to 2000, are shown in Fig. 4.7 for
a) 850 hPa and b) 200 hPa. Within the ZWSI area, there is a large shear of the
zonal winds visible from 850 hPa to 200 hPa, while the shear of the meridional
winds in the MWSI area is small. Furthermore, an anti-clockwise rotation can
be seen to the west of Bangladesh at 850 hPa, and a clockwise rotation at 200
hPa over the Himalayan ridge.

Figures 4.8 a) and b) show the linear trends in the wind fields from the
COSMO-CLM A2 simulation. Significant wind changes at 850 hPa are restricted
to a decrease of eastward winds in the southern part of the simulation domain.
These changes have a size of about 2-3 m/s in A2 (Fig. 4.8) and A1B, and about
$2 m/s$ in B1 (not shown). The reduced MWSI and ZWSI projected at the end
of the 21st century are thus mainly a result of shifts in the upper troposphere
winds. They result in a decrease of the southward shear in the eastern part of
the MWSI area and a decrease of westward shears in the ZWSI area (Fig. 4.8).
At 200 hPa, there is also an increased convergence visible over the Bay of Bengal
(Fig. 4.8). In all four scenarios, the distribution of the trends is again similar,
with the generally highest amplitudes in A2 followed by A1B, B1 and almost no
trends in the commitment scenario (not shown).

4.5.3   Convection

Note again that the OLR in this work is measured as being downward directed.
Thus, a lower value of the COLR index corresponds to less convective activity. In
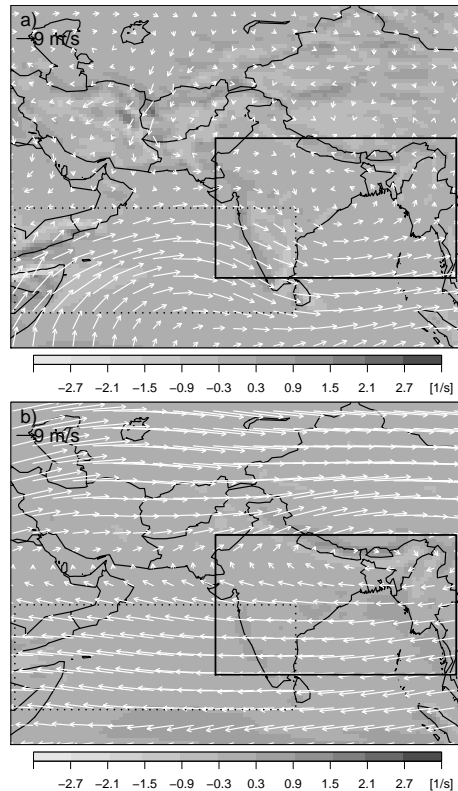
Figure 4.7: Divergence (colored areas) and directions (arrows) of wind fields at a) 850 hPa and b) 200 hPa for the monsoon season from 1971-2000 as simulated by the COSMO-CLM. The MWSI and ZWSI areas are given by a solid and dotted rectangle, respectively.

Fig. 4.9 the 21-year running means of the standardized COLR index are given. Although the trends are less clear than they are for the MWSI, ZWSI and AIMR indices, the low values at the end of the A2 and A1B scenario are again evident. There is a large difference between the ECHAM5/MPIOM and the COSMO-CLM commitment projection. The reason for this is unclear. Due to its shortness, the observed time series shows mainly that there are some variations in COLR as well, but does not reveal any valuable information on an observable trend.

The decreasing COLR in A1B and A2 are a consequence of negative OLR trends in large parts of the averaging area (Fig. 4.10). Furthermore, an OLR decrease is visible in almost the complete upper half of the simulation domain. Overall, there is a good agreement of the COLR trends with the trends in the monsoon precipitation.
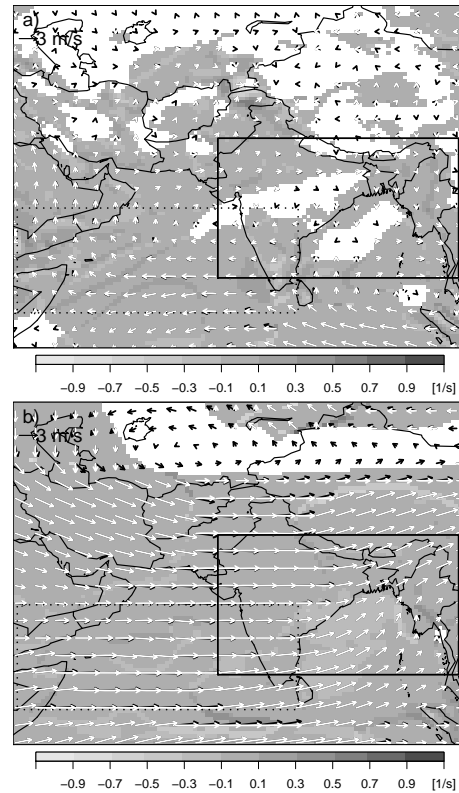
Figure 4.8:   Linear trends (per century) in the divergence and directions of the winds at a) 850 hPa and b) 200 hPa during the time period 1960-2100 in the COSMO-CLM A2 simulation. Colored areas and white arrows show significant trends (at the 5% significance level). Black arrows show non-significant wind changes.
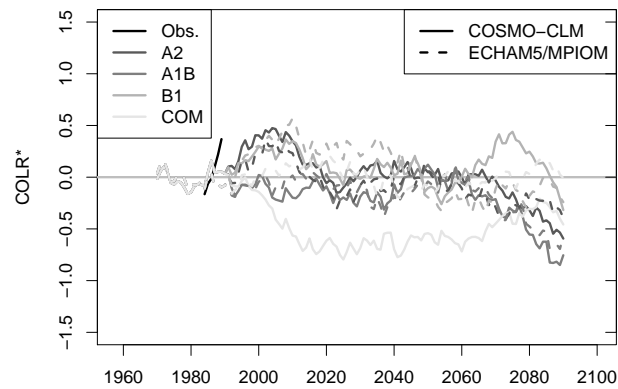
Figure 4.9:   As for Fig. 4.2, but for COLR.
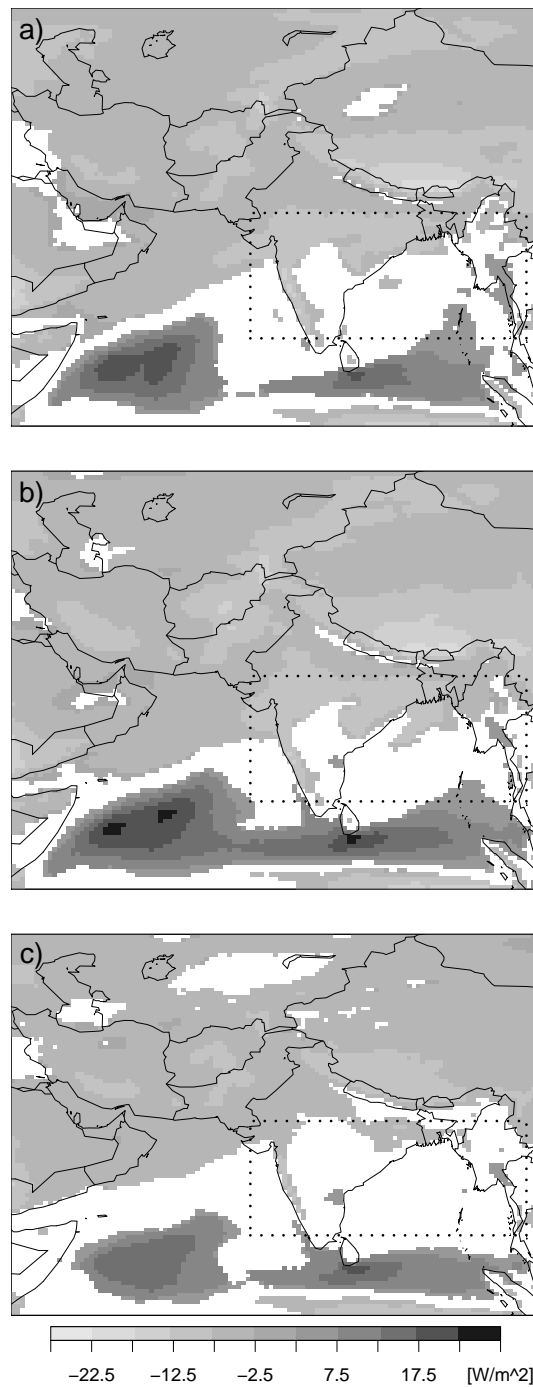
Figure 4.10: Linear trends in outgoing longwave radiation (W/m^2 per century) during the time period 1960-2100 in a) the A2, b) the A1B and c) the B1 COSMO-CLM run. Colored areas show significant trends (at the 5% significance level) and the COLR area is indicated by a dotted rectangle.

4.5.4   Index correlations

A teleconnection between the ISM and the El Niño Southern Oscillation is well-documented (Walker, 1923; Rasmusson and Carpenter, 1982; Ju and Slingo, 1995) but has weakened in recent decades (e.g., Kripalani and Kulkarni, 1997; Kumar et al., 1999). As shown in Fig. 4.11, the observed 21-year sliding explained variance (R^2_{21}) of AIMR by the NINO3.4 index drops below 0.1 at the starting year of 1989. The NINO3.4 data were obtained from the Climate Prediction Center, National Oceanic and Atmospheric Administration, USA Web site `http://www.cpc.noaa.gov/data/indices`. The dataset starts in 1871 and is updated continuously. For the whole time period, no value of R^2_{21} below 0.1 can be observed before 1989-2009 (not shown).

For the ten to 14-year sliding R^2, however, the data show values above 0.1 for the last few years (Fig. 4.11), indicating a new strengthening of the relationship. Note that sliding windows below ten years are excluded from this study due to brevity, and OLR data are excluded due to the short observation time period.

Figure 4.11 further includes the explained variance of AIMR by ZWSI and MWSI for different sliding window sizes. Here also, a clear decrease of R^2_{21} during the last decades is evident but no further decrease is apparent in the last years.
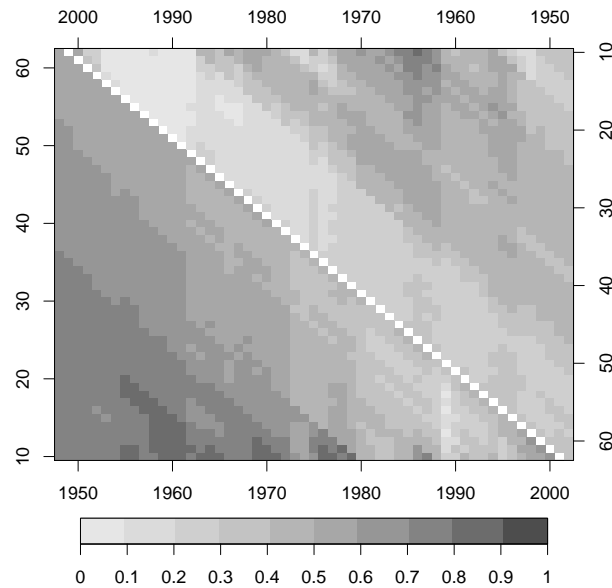
Figure 4.11: Observed explained variance (R^2) in AIMR by Niño 3.4 (upper-right part) and by MWSI and ZWSI (lower-left part) for different sliding window sizes (left and right axes) over the time period from 1948 to 2009. The years on the top and bottom axes denote the starting year of the sliding window.
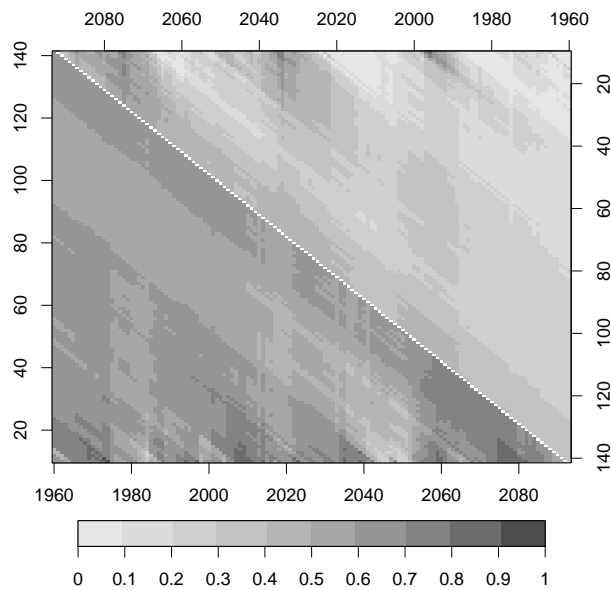
Figure 4.12: As for Fig. 4.11, but for the COSMO-CLM A2 simulation over the time period from 1960 to 2100.

The sliding explained variances of the COSMO-CLM and ECHAM5/MPIOM A2 scenario runs are given in the Figs. 4.12 and 4.13 for the years of 1960-2100. Contrary to the ECHAM5/MPIOM, the COSMO-CLM simulation shows values of R_{21}^2 below 0.1 for AIMR explained by NINO3.4. Note that the NINO3.4 index for the COSMO-CLM projections has been calculated using the data from the ECHAM5/MPIOM because the NINO3.4 averaging region is outside the regional simulation domain. Thus, the correlation between the AIMR and the NINO3.4 index in the COSMO-CLM is expected to be smaller than that in the driving model. This clearly biases this evaluation to some extent.

However, for the explained variance of AIMR by ZWSI and MWSI, there are no such limitations. During the time period common with the observations (1960-2009), the resulting R^2 is 0.60 for the COSMO-CLM, 0.84 for the ECHAM5/MPIOM and 0.55 for the observations. The values in the ECHAM5/MPIOM are generally higher than in the COSMO-CLM, and the regional model is closer to the observed values (Figs. 4.12 and 4.13). For instance, R_{21}^2 shows a mean value of 0.63 for COSMO-CLM, 0.70 for ECHAM5/MPIOM and 0.59 for the observations. The minimum (maximum) values of R_{21}^2 are 0.33 (0.79) for COSMO-CLM, 0.44 (0.93) for ECHAM5/MPIOM and 0.27 (0.79) for the observations. Thus, while both models show an overestimation of the explained variance, the COSMO-CLM is closer to the observations than the ECHAM5/MPIOM. For the other SRES scenarios, the improvement in the index correlations is similar (not shown). This is also in agreement with the findings in

Dobler and Ahrens (2010) for the present climate.
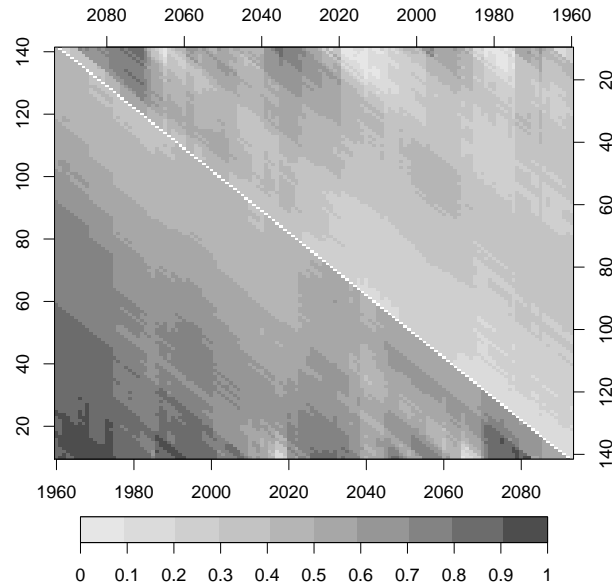
Figure 4.13: As for Fig. 4.12, but for the ECHAM5/MPIOM A2 simulation.

Noteworthy is the large area of low values of R^2 in the ECHAM5/MPIOM simulations (Fig. 4.13) at the end of the simulation time with a sliding window size of over 70 years. These low values are the result of an increase in the AIMR and a simultaneous decrease in the ZWSI and MWSI or in the Niño 3.4 index at the end of the simulations.

4.6   Conclusions

Four indices used to investigate the projected change in the Indian summer monsoon (ISM) during the 21st century show decreasing trends for the SRES scenarios A2, A1B and B1 in the regional climate model COSMO-CLM. Generally, the trends are most negative in A2, followed by A1B and B1. Almost no trends can be found in the commitment scenario. This suggests a negative influence of greenhouse gas emissions on the ISM strength.

The use of transient climate simulations from 1960 to 2100 allows us to include long-term variations in the analysis. Although there are large variabilities in all time series, the trends in rainfall, outgoing longwave radiation, and meridional and zonal wind shear are statistically significant in many regions of the simulation domain. For the north-western part of India, the simulations show highly negative trends in monsoon precipitation amounts of up to more than -70% per century.

For the global coupled atmosphere-ocean model ECHAM5/MPIOM the trends in the indices are similar to the COSMO-CLM simulations with the exception of the all-India monsoon rainfall (AIMR) for which the ECHAM5/MPIOM shows positive trends in all scenarios (Fig. 4.2). According to the current knowledge on the ISM system represented through the applied indices (Wang and Fan, 1999; Goswami, 2000), a simultaneous decrease in all indices, as in the COSMO-CLM, is more realistic.

An investigation of the explained variance of AIMR by MWSI and ZWSI or the NINO3.4 index shows that the currently observed lack in predictability of the AIMR is below the simulated minimum values. The average explained variances in the COSMO-CLM and the ECHAM5/MPIOM are higher than in the observations. This indicates that in both models an essential part in the interaction of dynamics and physics affecting the ISM is missing. In the COSMO-CLM this may for instance be the lack of an atmosphere-ocean coupling. However, the values in the COSMO-CLM are closer to the observations than those in the driving ECHAM5/MPIOM model, and the index correlations are improved by the regional climate model.

Although we used an RCM approach with a tested setup (Dobler and Ahrens, 2010) and four different SRES forcing, there are some limitations to our approach. First, a broader ensemble of different GCMs would provide more information on the uncertainties in the projected changes. Second, the tested setup shows some non-negligible biases (Dobler and Ahrens, 2008, 2010; Lucas-Picher et al., 2010) of which we can only assume, that they are constant in the model projections and thus removed by the standardization of the indices. However, a similar study using the RCM RegCM3 (Ashfaq et al., 2009) showed that the simulated change of ISM rainfall is insensitive to the choice of the driving GCM, vertical resolution and initial conditions. This is further supported by the similarity of the results found therein and in this study for the A2 scenario.

Chapter 5

Regional climate projections in two alpine river basins: Upper Danube and Upper Brahmaputra

5.1 Abstract

Projections from coarse-grid global circulation models are not suitable for regional estimates of water balance or trends of extreme precipitation and temperature, especially not in complex terrain. Thus, downscaling of global to regionally resolved projections is necessary to provide input to integrated water resources management approaches for river basins like the Upper Danube River Basin (UDRB) and the Upper Brahmaputra River Basin (UBRB).

This paper discusses the application of the regional climate model COSMO-CLM as a dynamical downscaling tool. To provide accurate data the COSMO-CLM model output was post-processed by statistical means. This downscaling chain performs well in the baseline period 1971 to 2000. However, COSMO-CLM performs better in the UDRB than in the UBRB because of a longer application experience and a less complex climate in Europe.

Different climate change scenarios were downscaled for the time period 1960-2100. The projections show an increase of temperature in both basins and for all seasons. The trends are generally larger in the UBRB with the highest values occurring in the region of the Tibetan Plateau. Annual precipitation shows no substantial change. However, seasonal amounts show clear trends, for instance an increasing amount of spring precipitation in the UDRB. Again, the largest trends for different precipitation statistics are projected in the region of the Tibetan Plateau. Here, the projections show up to 50% longer dry periods in the months June to September with a simultaneous increase of about 10% for the maximum amount of precipitation on five consecutive days. For the Assam region in India, the projections also show an increase of 25% in the number of consecutive dry days during the monsoon season leading to prolonged monsoon breaks.

5.2 Introduction and objectives

The Danube and the Brahmaputra River have their headwaters in mountainous regions where massive glacier retreat and permafrost thaw have been observed in recent times. Thus, further climate warming is likely to impact water availability and hydrological dynamics in both river-basins. In this regard climate model projections can be used to gain some estimate of possible future impacts.

To estimate the impact of future climate change on the hydrology at the basin scale, climate projections with a suitable temporal and spatial resolution are essential input to hydrological models. However, projections from current global circulation models (GCMs) have a grid resolution of about 200 km or more. Further, these projections mostly agree on the global and continental scale of precipitation and temperature change in the 21st century, but the projections for precipitation changes diverge with decreasing spatial scales (Bates et al., 2008).

Thus, GCM projections are inappropriate to assess the impact of climate change on a regional scale related to integrated water resources management (IWRM) in the UDRB and the UBRB. A downscaling of the large-scale simulations to a resolution of 50 km or less is necessary (Ahrens, 2003; Beck et al., 2004; Frei et al., 2003; Salathé, 2003). To this end, it is essential to find a well suited GCM and to apply an appropriate downscaling method to the GCM projections.

In this paper we discuss the comparison and enhancement of existing downscaling methods, their validation by means of observational data sets and the application to different GCM scenarios in the UDRB and UBRB.

5.3 Role within the integrated project

As glacier and permafrost melting are natural system processes with long response times, the respective impact models should be driven by transient regional climate projections. However, due to limited available computational power, there has been a lack of transient projections, especially in South Asia where earlier studies (e.g., Kumar et al., 2006) mostly were based on time slice experiments.

Within the BRAHMATWINN project (`http://www.brahmatwinn.uni-jena.de`) downscaled GCM projections were used as input to the hydrological model DANUBIA to simulate historical and future water balances of the UDRB and the UBRB (Prasch et al., 2010). Furthermore the data were used in snow glacier and permafrost modelling (Lang et al., 2010) and, to assess the question of a changing climate directly, in the calculation of climate change indicators (Giannini and Giupponi, 2010; Giannini et al., 2010).

To cope with these necessities, we provided transient climate projections for the UDRB and the UBRB covering the years 1960-2100. The A1B, B1, A2, and the commitment scenario, as given in the IPCC Special Report on Emissions

Scenarios (SRES, Nakicenovic and Swart, 2000), were used to generate a small ensemble of possible future developments.

5.4   Scientific methods applied

The testing and further development of existing downscaling techniques is an important first step in the generation of regional climate projections with a high temporal and spatial resolution. The latter is a prerequisite to evaluate the use of these data for the estimation of the regional impact of future climate change.
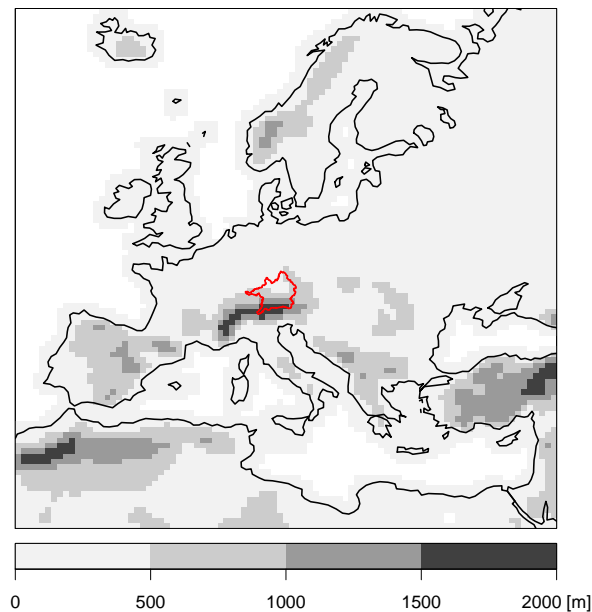

Figure 5.1: Model orography used in the European computational domain with the UDRB (red).

Generally, two different classes of downscaling methods may be applied (Murphy, 1999; Xu, 1999): a) dynamical downscaling methods based on simulations of physical processes at a fine scale, typically using a regional climate model (RCM) and b) statistical downscaling methods that employ observed statistical relationships between the coarse and the fine scale. Dobler and Ahrens (2008) tested different statistical, dynamical and combined downscaling methods on global ERA40 re-analysis data (Uppala et al., 2005) in Europe and South Asia with respect to rain day frequency and intensity. For this study, one of the proposed combined downscaling methods was further developed and implemented for application on GCM data at different high-performance computing sites.

As the dynamical downscaling method we applied the RCM COSMO-CLM (`http://www.clm-community.eu`) in a European (Fig. 5.1) and a South Asian
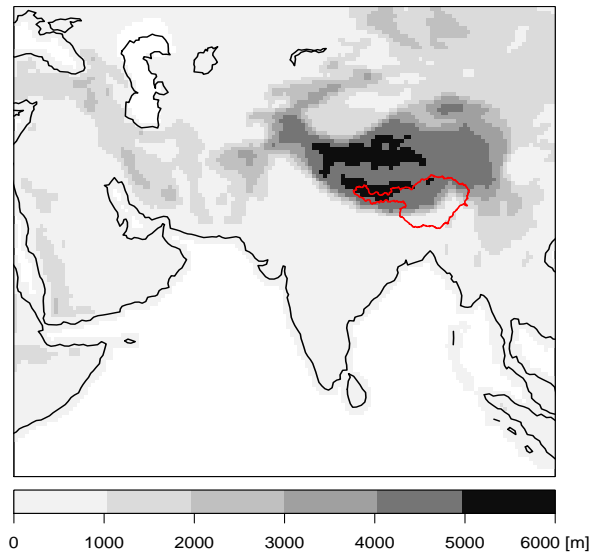
Figure 5.2: As for Fig. 5.1, but for the South Asian computational domain
with the UBRB (red).

region (Fig. 5.2). The COSMO-CLM is based on the COSMO (COnsortium for
Small scale MOdeling) model originally called Lokal Modell (LM) which was de-
veloped by the *German meteorological service* (DWD) in 1999 (Steppeler et al.,
2003). A detailed documentation of the LM (Doms and Schättler, 1999) is avail-
able at `http://www.cosmo-model.org`. More information on the model setup
and results of regional climate simulations over Europe and South Asia are given
in Dobler and Ahrens (2008, 2010) and Kothe et al. (2010).

Observational data was needed for the two basins for evaluation and for sta-
tistical downscaling methods. As in-situ measurements are sparse in the UBRB,
they were replaced with the following gridded, observational data sets, which in
most cases are globally available.

- CRU TS 2.1 (Mitchell and Jones, 2005): monthly temperature and precip-
  itation data on a global 0.5° grid for the years 1901-2002

- UDEL version 1.02 (Legates and Willmott, 1990): monthly temperature
  and precipitation data on a global 0.5° grid for the years 1950-1999

- GPCC full data product version 4 (Schneider et al., 2008): monthly pre-
  cipitation data on a global 0.5° grid for the years 1901-2007

- F&S version 4.1 (Frei and Schär, 1998): daily precipitation data on a
  1/6° grid covering the European Alps for the years 1971-1999

- EAD v0804 (Xie et al., 2007): daily precipitation data on a 0.5° grid covering South East Asia for the years 1980-2002

- ZGIS: a newly developed daily temperature data set on a 0.5° grid covering the two basins based on observational data retrieved from the NCDC web page `http://www.ncdc.noaa.gov/cgi-bin/res40.pl?page=gsod.html`, controlled and mapped by the Centre for Geoinformatics, Salzburg (Kienberger et al., 2008).

To quantify the uncertainty of the observational data sets in the basins, a comparison of the climatological annual cycle in temperature and precipitation was carried out, including ERA40 re-analysis data.

The downscaling approach developed for and tested on ERA40 re-analysis data were applied to GCM data. The GCM selection was based on the evaluation of models used in the fourth IPCC assessment report (IPCC, 2007a). van Ulden and van Oldenborgh (2006) have investigated 23 GCMs on the quality of simulated global sea level pressure patterns. Further, Kripalani et al. (2007) have tested 22 GCMs for their performance in the South Asian region. Amongst these 22 models, they found no best model and a multi model ensemble (MME) mean was proposed as benchmark. Unfortunately, a multi driving-model ensemble was not feasible in the time frame of BRAHMATWINN and a single GCM had to be selected.

Projections from the selected GCM were then downscaled to a resolution of about 50 km. The dynamical downscaling of four SRES scenarios was followed by a bias correction of the downscaled precipitation and temperature fields taking into account the limited availability of observational data in the UBRB. For other hydro-meteorological fields no bias correction was applied due to lack of quality proofed observational data sets. Further, the impact models used within the BRAHMATWINN framework are assumed to show the highest sensitivity to precipitation and temperature.

5.5 Results achieved and deliverables provided

5.5.1 Observation uncertainties

The investigation of different observation data sets in the two basins shows that for precipitation, the uncertainties in the UDRB are relatively small with less than 20 mm/month (Fig. 5.3). Contrary, in the UBRB the data sets differ with a maximum range of 70 mm/month in the monsoon months June to September as shown in Fig. 5.4. However, only small uncertainties appear in the temperature data sets, both in the UDRB (up to 2.2°C, Fig. 5.3) and the UBRB (up to 1.2°C, Fig. 5.4). As the CRU data set also includes the information on rain

day frequency, it was chosen as the observational reference for temperature and precipitation in both basins.
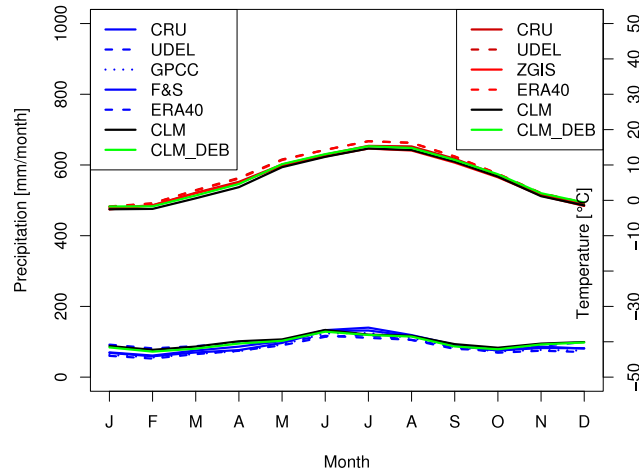
Figure 5.3: ERA40, observations and ERA40 driven COSMO-CLM simulations with (DEB) and without bias correction in the UDRB for the present climate.
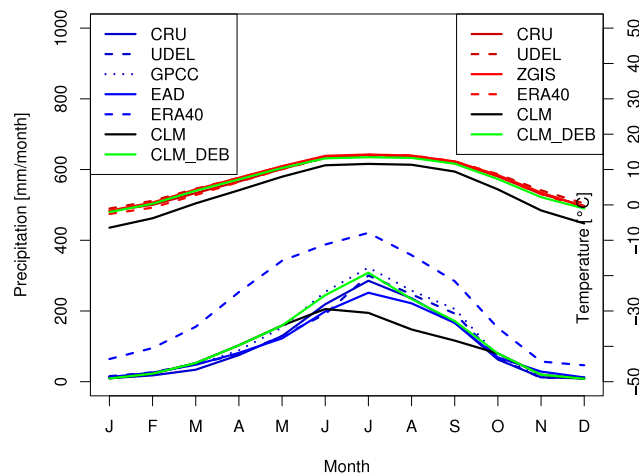
Figure 5.4: As for Fig. 5.3, but for the UBRB.

5.5.2 Downscaling method

To firstly identify an appropriate downscaling method, ERA40 re-analysis data rather than data from a general GCM simulation have been downscaled from

about $1.125°$ grid spacing to about $0.5°$. This minimises the influence of large scale circulation uncertainties on the downscaling results.

Figures 5.3 and 5.4 show the climatology from ERA40 re-analysis, COSMO-CLM simulations and different observations for the UDRB and UBRB, respectively. While the European region shows a generally temperate climate (Fig. 5.3), the climate in South Asia is dominated by a monsoon system which supplies the region with up to 80% of the annual rainfall total (Fig. 5.4). The main deficiencies of the COSMO-CLM in the South Asian domain are apparent from June to September. As shown in Dobler and Ahrens (2008) the model tends to underestimate the observed rain day intensity in these months. For temperature, the COSMO-CLM shows a cold bias in the UDRB of up to $1.5°C$ in April and of up to $5°C$ in the UBRB in December.

As can be seen, the COSMO-CLM performs clearly better in the UDRB than in the UBRB. However, this has been expected, since the model was developed in Europe and adapted to this region. Nevertheless, considering the big uncertainties in the observations of precipitation, the COSMO-CLM performance in the UBRB is acceptable. Overall, the accuracy of COSMO-CLM precipitation at the $0.5°$ scale is comparable with that of the ERA40 precipitation, and, as shown by Dobler and Ahrens (2008), in most places it is also comparable with that of statistically downscaled ERA40 precipitation. In the UBRB, the COSMO-CLM shows much better results than the ERA40 precipitation. This has also been expected, since the orography represented by ERA40 is very coarse and deficiencies in this region are well known (Hagemann et al., 2005).

As the downscaled data was used as input for hydrological modelling (Prasch et al., 2010), a set of hydro-meteorological data (temperature, precipitation, humidity, surface radiation, wind, etc.) was needed. Generating such data sets with statistical downscaling methods is highly limited by the sparseness of long term observations which focus mainly on precipitation and temperature. Therefore, the dynamical downscaling method is preferable.

5.5.3   Bias correction

An additional post-processing bias correction has been applied to precipitation and temperature. For precipitation this showed to be problematic in the UBRB, where a high seasonality in the COSMO-CLM bias and a large uncertainty in the bias estimation for non-monsoon months have negative impacts on the tested methods (Dobler and Ahrens, 2008). The uncertainties in the bias estimation were found to result from the few rain days in the dry months. To reach the proposed minimum number of rain days (about 500) a statistical approach based on local rain day intensity scaling (Schmidli et al., 2006) was developed which corrects the frequency of wet days and the mean wet day precipitation to fit the observed values in a specific calibration period. The method uses monthly rainfall amounts and number of rain days, both obtained from the CRU data set.

This allows for a longer calibration period (44 years) than using the EAD data set in the South Asian region. However, to guarantee a robust bias estimation (and thus correction) the calibration period for the method must still include sufficient rain days. Therefore, the method was applied on a monthly basis only to the months June to September in the UBRB. In the UDRB, the method was applied without monthly splitting as there is almost no seasonality in the COSMO-CLM precipitation bias.

For the 2m temperature a simple Gaussian bias correction was applied at each grid point. To this end, the simulated 2m temperature time series (3 hourly) T_i^S were corrected by fitting the monthly annual cycle to observations by eq. 5.1.

$$T_i^* = \frac{T_i^S - \overline{T^S}}{\sigma^S} \cdot \sigma^O + \overline{T^O}. \tag{5.1}$$

Through this the mean $\overline{T^S}$ and the variance σ^S are linearly corrected to be equal to those of the observation data ($\overline{T^O}$ and σ^O, respectively). Here again, we used the CRU temperature data set as reference.

Figures 5.3 and 5.4 show the positive effects of the applied bias correction methods in both twinning basins.

5.5.4 Downscaling of GCM data

After testing the downscaling approach on ERA40 forcing data, the method was applied to GCM data from the coupled atmosphere-ocean model ECHAM5/MPIOM (Jungclaus et al., 2006). The ECHAM5/MPIOM was selected for the following reasons to provide the necessary GCM data.

1. It is among the top models simulating a realistic 20th century South Asian monsoon climate (Kripalani et al., 2007).

2. The simulated pressure field has a high skill in the mean spatial correlation and in the mean explained spatial variance for Europe as well as globally (van Ulden and van Oldenborgh, 2006).

3. There is broad experience with the model in downscaling applications in Europe (e.g., `http://ensembles-eu.metoffice.com` and `http://prudence.dmi.dk`).

4. It is in good agreement with known large-scale features of the Asian summer monsoon including the re-establishing of the westerly jets south of the Himalayas and the decay of the anticyclone on the Tibetan Plateau after the monsoon season (data not shown).

5. The COSMO-CLM is able to provide the information necessary for the assessment of regional climate change impacts when driven by the ECHAM5/MPIOM (Dobler and Ahrens, 2010).

Note that while current GCMs projections mostly agree in positive regional and global temperature trends during the 21st century, there is still much disagreement in the projections of precipitation, especially on the regional scale (IPCC, 2007a). Therefore, the selection of a GCM for dynamical downscaling based on projected precipitation changes on the regional scale is inappropriate. For instance in the UBRB, the HadCM3 (Jones et al., 2004) model shows an increase of annual precipitation of about 14% from 1971-2000 to 2071-2100 while the ECHAM5/MPIOM shows an increase of 3% only during this time period (data not shown).

5.5.5 Regional climate projections

To assess the issue of changing climates in the two basins, seasonal trends of daily precipitation and temperature indicators (Tab. 5.1) were calculated for the simulation period 1960-2100. For the European regions the seasons are spring (SP, March to May), summer (SU, June to August), autumn (AU, September to November) and winter (WI, December to February). As suggested by Basistha et al. (2009) for the South Asian regions these are summer (SU, March to May), monsoon (MO, June to September), post-monsoon (PM, October to November) and winter (WI, December to February).

Table 5.1: Description of climate change indicators for precipitation and temperature. The wet/dry day threshold used was 1 mm/d.

Acronym	Description	Unit
PFRE	Fraction of wet days	1
PREC	Total precipitation amount	mm
PINT	Mean precipitation amount on wet days	mm/d
PQ90	90% quantile of wet days precipitation	mm/d
PX5D	Max. 5-day precipitation amount	mm
PCDD	Longest period of consecutive dry days	d
T2M	Mean 2m temperature	°C
T2MIN	Mean daily minimum 2m temperature	°C
T2MAX	Mean daily maximum 2m temperature	°C

The projections were normalized with respect to the reference period 1971-2000. This is an easy way to remove constant model biases and a comparison to more complex bias correction methods has shown no significant differences in the resulting trends (data not shown). The trends were tested for statistical significance at the 5% level using a linear model.

To give a general summary of the indicator trends is very difficult. The single projections show big regional and seasonal differences. But overall, the commitment scenario shows the smallest trends up to the year 2100, followed by the B1, A1B and finally the A2 scenario. However, up to the year 2080 most A1B trends are higher than those of the A2 scenario (data not shown). This can be explained by the higher emissions of the A1B scenario at the beginning of the 21st century. Thus, the magnitude of the trends is generally in direct relation to the amount of greenhouse gas emissions of the single scenarios.

We will concentrate our evaluations on the results from the scenarios A1B and B1 in the following subsections as they were within the main focus of the BRAHMATWINN project: A1B was considered as the most likely one and B1 as a more optimistic one. However, the projected trends of the A1B and A2 scenario are close to each other. In the commitment scenario, constant greenhouse gas concentrations are assumed after the year 2000. Thus, it may be used as a control experiment to estimate the impacts of anthropogenic forcings on the climates in the two regions. This is however out of the scope of this study.

5.5.5.1 Temperature changes

Figures 5.5 and 5.6 show the annual temperature trends for the four SRES scenarios in the two basins. For the A1B scenario, the temperature increase until the year 2100 is projected around 4°C in the UDRB and 5°C in the UBRB. For B1 the increase is around 2°C in the UDRB and 4°C in the UBRB .
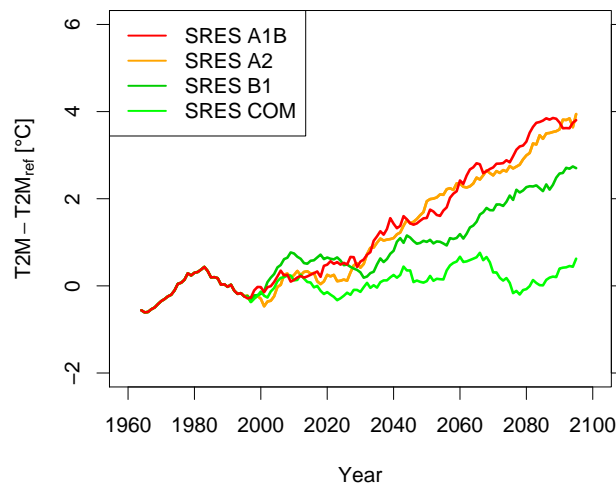
Figure 5.5: Ten year running means of temperature increase in the UDRB for four SRES scenarios.

For A1B the temperature trends are around +3 to +4°C within the UDRB (Fig. 5.7) and up to more than +6°C within the UBRB (Fig. 5.8). In both basins,
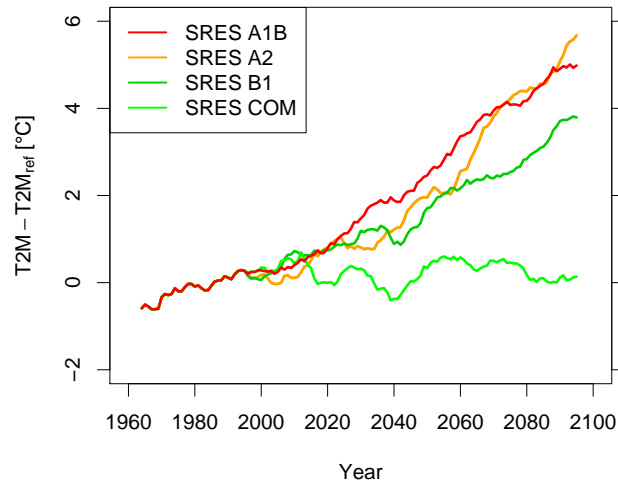
Figure 5.6: As for Fig. 5.5, but for the UBRB.

the temperature increase in higher elevated areas is larger than in low level areas and the largest trends appear in the region of the Tibetan Plateau. In B1, the trends are about 1°C smaller than in A1B throughout both basins (data not shown).
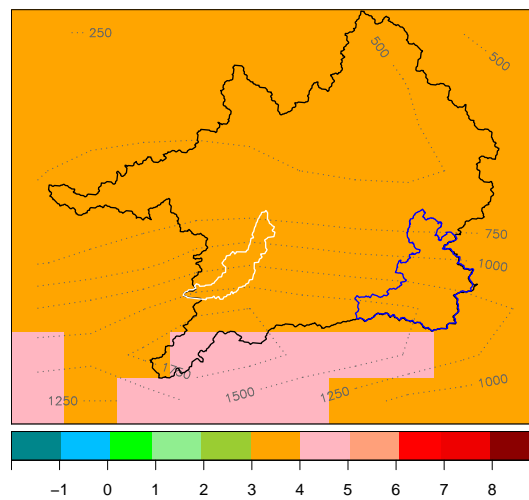
Figure 5.7: Linear trends of the annual mean temperature (°C/cent.) in the UDRB during the time period 1960-2100 following the A1B scenario. Coloured areas show significant trends (at the 5% level). The grey dotted lines denote isohypses in m a.s.l. Also shown are the Lech (white) and the Salzach (blue) river basin.
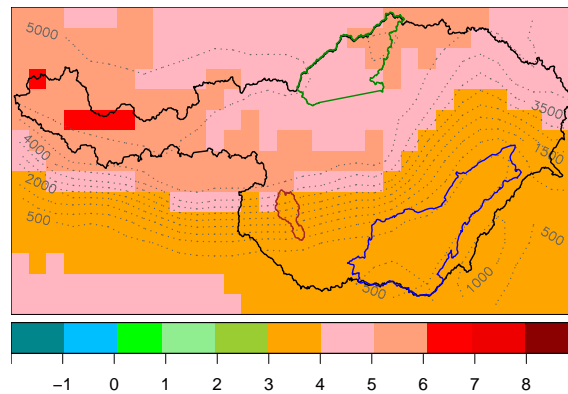
Figure 5.8: As for Fig. 5.7, but for the UBRB with the Assam region (blue),
the Lhasa (green) and the Wang-Chu (brown) river basin.

Figures 5.9 and 5.10 show the seasonal temperature trends and the spatial variability of the trends in A1B for the UDRB and the UBRB, respectively. Spatially averaged trends that are statistically significant are indicated by a red cross for the A1B scenario and a green cross for the B1 scenario. As can be seen, both scenarios show significant positive trends for all seasons in temperature, as well as daily minimum and maximum temperature in both basins. The increase of the maximum daily temperature is generally highest, followed by the increase of mean temperature and the increase of the daily minimum temperature suggesting an increase in temperature variability. However, there are also exceptions to this, for instance during the post-monsoon season in the UBRB and spring in the UDRB.

5.5.5.2 Precipitation changes

The projected precipitation trends are less unanimous than the temperature trends. No significant trends were found in the two basins for the annual precipitation amounts (Figs. 5.11 and 5.12). This is however a result of trends compensating each other in the different seasons and areas.

Figures 5.13-5.16 show the trends of precipitation-based indicators in the UDRB and UBRB. In A1B, the summer precipitation amount in the UDRB is decreasing with about 20%/century (Fig. 5.13) and the monsoon precipitation amount in the UBRB with about 10%/century (Fig. 5.15). Simultaneously, there is a decrease in the number of precipitation days (PFRE), an increase in the rain-day intensity (PINT) as well as an increase in the length of consecutive dry days (PCDD) in both basins.

In the UDRB there is further an increase of PX5D (Fig. 5.14) and of PREC (Fig. 5.13) in spring. As can be seen, there are less significant precipitation trends
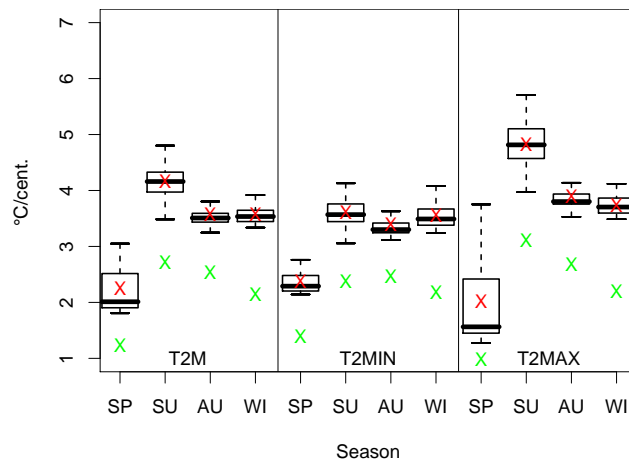
Figure 5.9: Spatial variability of seasonal trends in T2M, T2MIN and T2MAX in the UDRB for the A1B scenario. Red and green crosses show statistically significant spatial mean trends for the A1B and the B1 scenario, respectively.
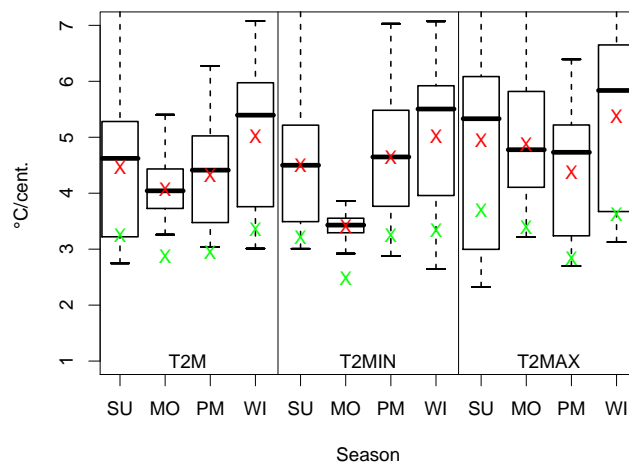
Figure 5.10: As for Fig. 5.9, but for the UBRB.

in the UBRB than in the UDRB which is due to a larger inter-annual variability (data not shown). In both basins, the PQ90 trends agree to a large extend with the trends in PINT for all seasons.

At sub-basin scales the trends are even more varying. In the monsoon season for instance, there is an increasing trend in the A1B scenario for PX5D of 9% in the Lhasa river basin (Fig. 5.17). Simultaneously, PCDD increases by 53% in the Lhasa river basin and by 20% in Assam (Fig. 5.18). For B1, these trends are about 50% smaller but the spatial distribution is similar (data not shown).

Figures 5.17 and 5.18 and the high temperature increases shown above indicate
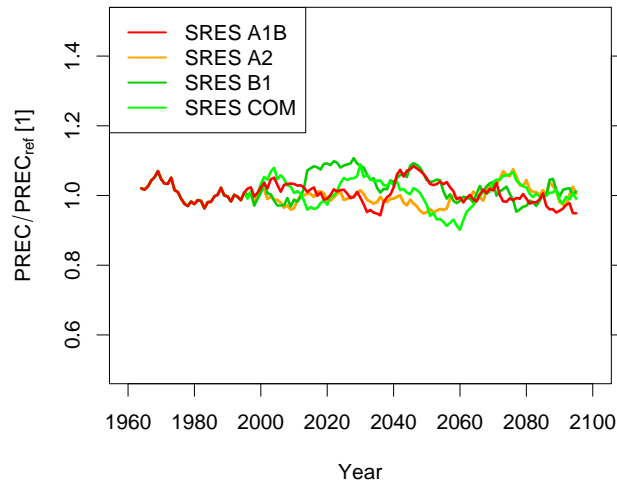
Figure 5.11: Ten year running means of precipitation change in the UDRB for four SRES scenarios.
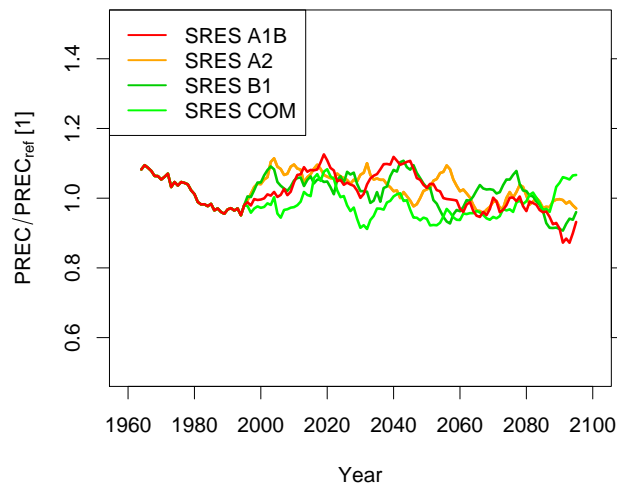
Figure 5.12: As for Fig. 5.11, but for the UBRB.

that the Tibetan Plateau is a region highly sensitive to future climate changes. For Assam, the positive trend in PCDD implies longer monsoon breaks, which in the current climate show a typical length of 15 days.
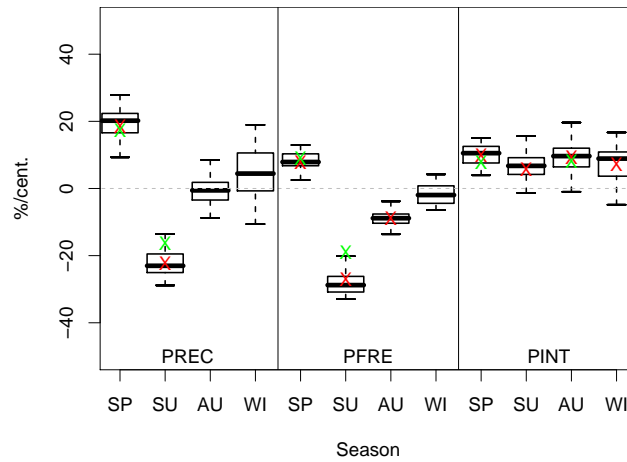
Figure 5.13: As for Fig. 5.9, but for PREC, PFRE and PINT.
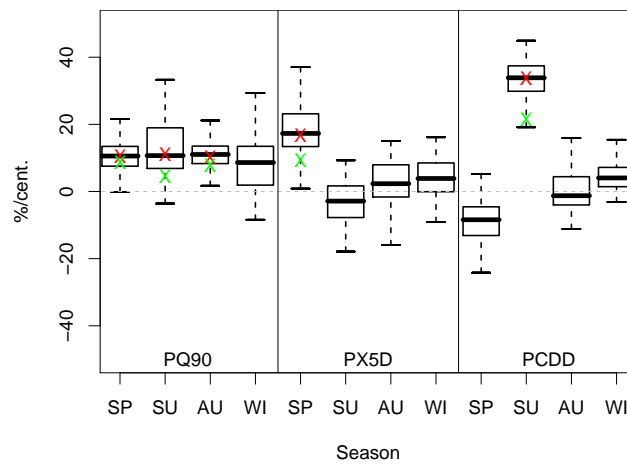
Figure 5.14: As for Fig. 5.9, but for PQ90, PX5D and PCDD.

5.6   Contributions to sustainable IWRM

The presented GCM downscaling approach provided the basis for the integrated water resources management system comprising the DANUBIA hydrological model, the river basin information system (RBIS) and the network analysis and creative modelling decision support system NetSyMoD which is building a sustainable development based on stakeholder negotiations within the framework of the BRAHMATWINN project.

The results shown in this paper provide sound evidence about likely climate change dynamics which will impact the hydrological process dynamics and runoff generation at present active within both twinning basins. They provide a scenario
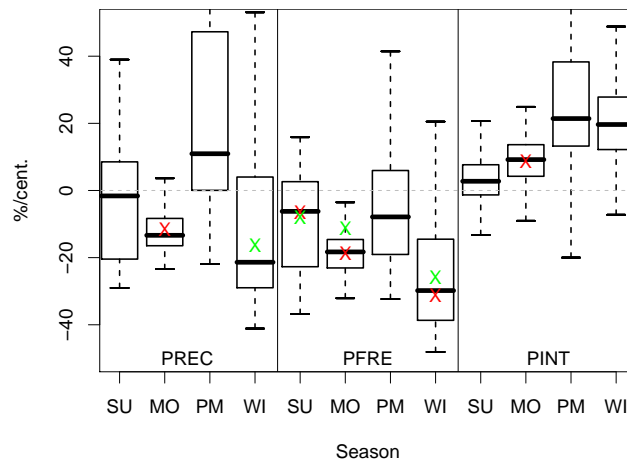
Figure 5.15: As for Fig. 5.9, but in the UBRB and for PREC, PFRE and PINT.
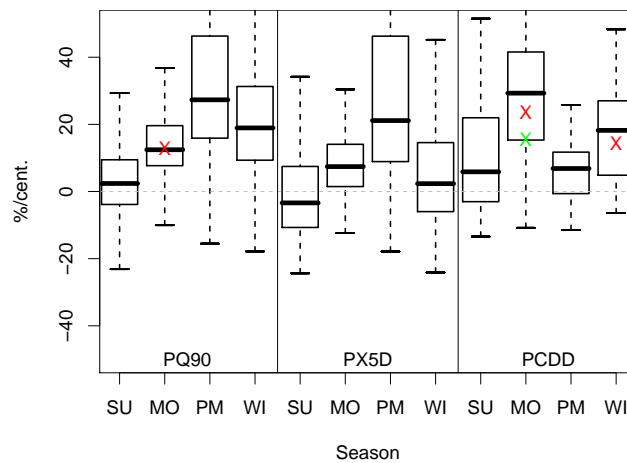
Figure 5.16: As for Fig. 5.9, but in the UBRB and for PQ90, PX5D and PCDD.

based framework setup within which adaptive management options for sustainable IWRM can be developed and evaluated.

The results discussed focus on the most pronounced trends in the UDRB and the UBRB during the years 1960-2100. A complete set of time series for all scenarios, seasons, areas of interest (see Figs. 5.7 and 5.8) and the indicators PREC, PX5D, PCDD, T2M, T2MIN and T2MAX (Tab. 5.1) for the years 1960-2100 are available through the RBIS of the BRAHMATWINN project.
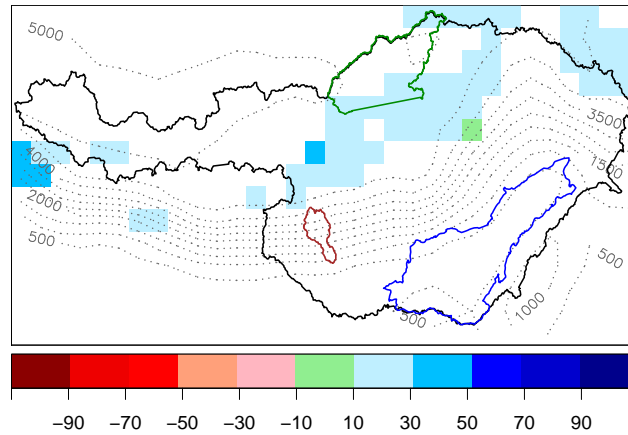
Figure 5.17: Linear trends of PX5D (%/cent.) in the UBRB in monsoon from 1960 to 2100 following the A1B scenario. White areas show non-significant trends (at the 5% level). The grey dotted lines denote isohypses in m a.s.l. Coloured lines show the Assam region (blue), the Lhasa (green) and the Wang-Chu (brown) river basin.
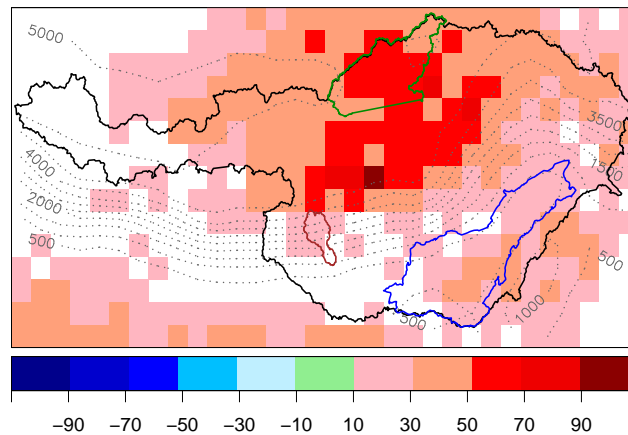
Figure 5.18: As for Fig. 5.17, but for PCDD.

5.7   Conclusions and recommendations

Using regional climate projections from the COSMO-CLM allows analysing the impact of the climate change signal on the regional water balance in the UDRB and the UBRB. To generate several likely scenarios for the time period 1960-2100, the COSMO-CLM was driven by the GCM ECHAM5/MPIOM with four different SRES forcings. The model output was for instance used as input to the hydrological model DANUBIA.

The temperature is projected to increase in both basins in the coming decades with the higher values in the region of the Tibetan Plateau. Thus, parameters directly dependent on temperature, like potential evapotranspiration, are also assumed to show clear trends. This will have a severe impact on the hydrology of the river basins.

Precipitation trends are less clear. Annual precipitation is projected not to change significantly, but seasonal amounts are. Different climate change indicators, like the length of the longest dry periods, indicate more frequent and prolonged droughts. However, there is no simultaneous tendency to less flooding events. The projected increasing amount of (1-day and 5-day) spring precipitation in the UDRB in combination with increased spring snow melt due to higher temperatures in the Alps might even yield more intense and frequent flooding events.

An increase in the number of consecutive dry days and in the maximum 5-day precipitation amount in the region of the Tibetan Plateau for the monsoon season, as well as large temperature trends indicate a highly sensitive region to future climate changes. For Assam, the positive trend in the number of consecutive dry days in the monsoon season indicate longer monsoon breaks.

In this study a specific model combination was used, and applying a different GCM to drive the COSMO-CLM would most likely result in slightly changed regional projections. As discussed above, the HadCM3 projects larger increases of precipitation in the UBRB than the ECHAM5/MPIOM. Thus, the COSMO-CLM may be expected to project slightly larger precipitation trends too, if driven by the HadCM3. This uncertainty clearly has to be considered. Although comparing to the different SRES scenarios the uncertainty is expected to be small, driving the COSMO-CLM with different GCMs would be preferable and reveal more insight on the influence of the driving model to the results.

Chapter 6

Conclusions

In this thesis, the application of the regional climate model COSMO-CLM in a European and a South Asian region is analyzed. The model is compared to two statistical downscaling methods on the basis of daily precipitation statistics. It is further evaluated using various parameters of the climate system to answer the question of a better representation of regional patterns in the downscaled data than in the large-scale driving models.

The investigations carried out lead to the conclusion that the COSMO-CLM provides the ability to regionalize global climate models (GCMs) in both regions and to yield additional regional information. For instance, the accuracy of the COSMO-CLM rainfall data on the 0.5° scale is comparable with ERA40 precipitation, and in most regions also comparable with statistically downscaled ERA40 precipitation. For the central European region, a dynamical downscaling with the COSMO-CLM provides a suitable method to generate accurate rainfall and temperature fields.

To generate unbiased input data for hydrological or other impact models, an additional bias correction of precipitation and temperature may be applied. However, in statistical downscaling methods and bias corrections, the estimation of statistical correlations between simulations and observations includes large uncertainties in the case of a low number of data points (such as in extreme events). The results of this thesis show that about 500 rain days are necessary to give an adequate degree of security in the estimation of statistical relations for rain day frequency and intensity. Thus, the application of statistical methods based on these relations in dry or seasonally dry climates is very limited. Although regional climate models do technically not have this disadvantage, the model evaluation and fine-tuning do have the same limitations.

The results in South Asia show some significant deviations from observed data. In this region (and other ones the model has not been designed for directly) a detailed examination of the results is required before the model data may be used, for instance as input to impact models. Due to current model limitations, bias corrections are necessary to provide suitable data in the South Asian re-

gion. However, to overcome the limitation of too few rain days, a correction of precipitation should be applied for the months from June to September only.

Nevertheless, the COSMO-CLM is able to compensate for problems of the driving model at the local scale considering the Indian summer monsoon (ISM). Although the regional model provides no added value in the representation of the ISM by large-scale indices, spatial rainfall and wind patterns and index correlations are more accurate than in the ECHAM5/MPIOM model, showing that the regional model is able to improve the GCM projections.

The COSMO-CLM projections partly show a decrease of rainfall from June to September of more than 70% per century in northwest India for the years 1960-2100. The decrease rates of various ISM indices in four different emission scenarios are generally in the same order as the greenhouse gas (GHG) concentrations. This points to a negative impact of GHG concentrations on the strength of the ISM.

Projections for the upper Danube and the upper Brahmaputra river basin reveal that the climate of the Tibetan Plateau is highly sensitive to future GHG emissions. Furthermore, the projections show a significant extension of monsoon breaks in the region of Assam in India. This would have a severe impact on agriculture in that region. In the upper Danube river basin, the spring precipitation is projected to increase. In conjunction with an increase in snow melt due to higher temperatures this would lead to more intense and more frequent floods during spring.

A general answer to the question which of the investigated methods is best suited to downscale GCMs can not be given in this work. Although the application on reanalyses provides the possibility of a quantitative ranking and testing of the methods, the ranking is not transferable to the application on GCMs. Results from this work show that a successful application on reanalyses is not sufficient to ensure a successful application on GCMs.

When using bias corrections, the model error must be constant in time to allow a robust error estimate and a successful application. Large model errors in the calibration time lead to large corrections of the model data in the application period and include a high risk of deterioration of the model data. Therefore, further developments in global and regional climate models are also necessary to generate adequate data for statistical methods, as the current models often do not meet these requirements. For the COSMO-CLM the investigations in this work show that a change in the parametrization of convection and the coupling to an ocean model would probably yield improved results.

Kapitel 7

Deutsche Zusammenfassung

7.1 Einleitung

Mit der zunehmenden Verfügbarkeit günstiger Rechenressourcen sind allgemeine Zirkulationsmodelle und regionale Klimamodelle sehr populär geworden und an vielen wissenschaftlichen Institutionen weltweit im Einsatz. Sie stellen hilfreiche Werkzeuge dar, um klimatische Prozesse zu verstehen sowie zur Simulation von historischen und zukünftigen Klimata unter verschiedenen Annahmen wie Konzentrationen von Treibhausgasen, Landnutzung, etc.

Die meisten der aktuell durchgeführten Klimaprojektionen verwenden Szenarien, die im Sonderbericht über Emissionsszenarien (SRES, Nakicenovic und Swart, 2000) des *International Panel on Climate Change* (IPCC, `http://www.ipcc.ch`) definiert sind. Innerhalb der dritten Phase des *Coupled Model Intercomparison Projects* (Meehl et al., 2007, `http://cmip-pcmdi.llnl.gov/`) wurden die Projektionen von mehr als 20 gekoppelten Ozean-Atmosphäre Zirkulationsmodellen nach den SRES-Szenarien gesammelt. Diese Daten bildeten die Grundlage für einen großen Teil der Forschungsergebnisse, welche im vierten IPCC-Sachstandsbericht vorgelegt wurden.

Die derzeit verfügbaren globalen Projektionen haben jedoch eine horizontale Auflösung von etwa zwei Grad (ca. 200 km am Äquator). Zur Abschätzung der regionalen Wasserbilanz ist diese Auflösung zu grob, weshalb eine Regionalisierung auf eine Auflösung von 0.5° (50 km) oder weniger notwendig ist, um regionale Niederschlagsmuster zu generieren (Ahrens, 2003; Beck et al., 2004; Dobler und Ahrens, 2008; Frei et al., 2003; Salathé, 2003). Dies gilt insbesondere für Regionen mit einer komplexen Orographie. Darüber hinaus sind sich zwar die meisten globalen Zirkulationsmodelle einig über die globalen und kontinentalen Temperaturänderungen im 21. Jahrhundert, unterscheiden sich aber substantiell in den Projektionen des Niederschlags auf regionaler Skala (Annamalai et al., 2007; IPCC, 2007b).

Die Zielsetzung dieser Arbeit ist die Untersuchung der Möglichkeiten und
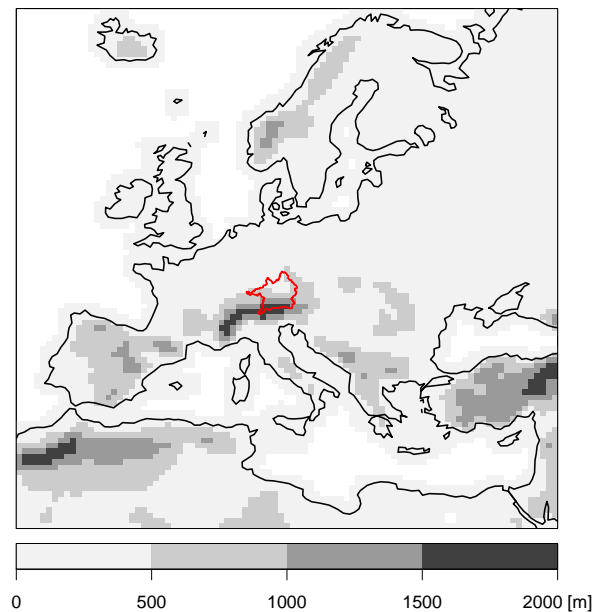
Abbildung 7.1: Europäisches Modellgebiet und Orographie mit dem Einzugsgebiet der oberen Donau (rot).

Grenzen von hochauflösenden Klimaprojektionen in orographisch stark beeinflussten Gebieten an den Beispielen der europäischen Alpen und des Himalajas. Zu diesem Zweck wurden regionale Klimasimulationen in einem europäischen und einem südasiatischen Gebiet (Abb. 1 und 2) erstellt. Die regionalen Klimasimulationen werden mit statistischen Regionalisierungsmethoden verglichen und anhand unterschiedlicher Parameter des Klimasystems evaluiert. Für das südasiatische Gebiet ist die Wiedergabe eines realistischen Monsunsystems von hoher Relevanz, insbesondere die Fragestellung, ob sich dieses im regionalen Modell besser darstellen lässt als im antreibenden globalen Modell.

Im Rahmen des Projekts BRAHMATWINN der Europäischen Union wurde des Weiteren eine Klimaänderungsstudie für die Einzugsgebiete der oberen Donau (Abb. 1) und des oberen Brahmaputra (Abb. 2) erstellt. Diese basiert auf Veränderungen täglicher Niederschlags- und Temperaturindikatoren in den einzelnen Jahreszeiten während der Zeitspanne 1960 bis 2100. In der europäischen Region wurden die Jahreszeiten Frühling (März bis Mai), Sommer (Juni bis August), Herbst (September bis November) und Winter (Dezember bis Februar) verwendet. Für Südasien wurde das Jahr unterteilt in Sommer (März bis Mai), Monsun (Juni bis September), Post-Monsun (Oktober und November) und Winter (Dezember bis Februar), wie von Basistha et al. (2009) vorgeschlagen. Die untersuchten Indikatoren sind in Tabelle 1 zusammengefasst.

Um verschiedene zukünftige Klimaentwicklungen abzudecken, wurden vier
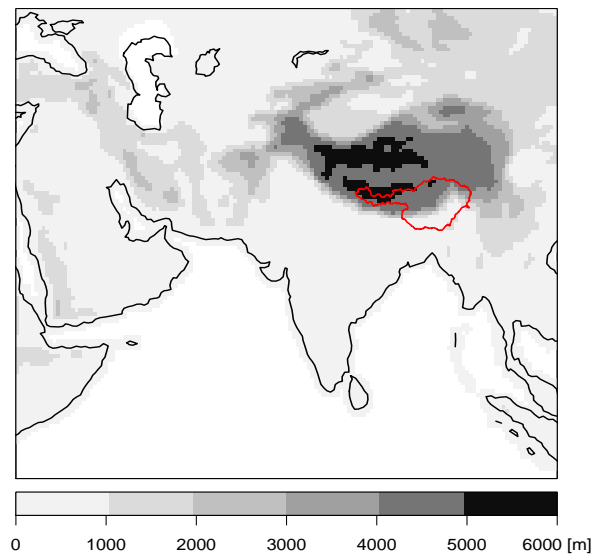
Abbildung 7.2: Südasiatisches Modellgebiet und Orographie mit dem Einzugsgebiet des oberen Brahmaputra (rot).

Projektionen für die Jahre 1960 bis 2100 anhand unterschiedlicher SRES-Szenarien durchgeführt. Die gewählten Szenarien und deren grundlegenden Annahmen sind wie folgt.

- A1B: ein schnelles wirtschaftliches Wachstum und eine moderate Zunahme der Weltbevölkerung mit Spitzenwerten in der Mitte des 21. Jahrhunderts, sowie eine schnelle Einführung von neuen und effektiveren Technologien mit einem ausgeglichenen Anteil an fossilen und nicht fossilen Energiequellen

- B1: Zunahme der Weltbevölkerung wie in A1B jedoch mit einer schnellen Einführung von sauberen und energieeffizienten Technologien

- A2: langsamer und heterogener Wirtschaftswachstum mit einer monoton zunehmenden Weltbevölkerung

- Commitment: konstante Treibhausgaskonzentrationen auf dem Niveau des Jahres 2000

Als weitere Anwendung wurden die regionalisierten Projektionen innerhalb des BRAHMATWINN Projekts als Antrieb für hydrologische Simulationen von historischen und zukünftigen Wasserbilanzen der oberen Donau und des oberen Brahmaputra (Prasch et al., 2010), zur Gletscher- und Permafrostmodellierung (Lang et al., 2010) und in der Berechnung von Indikatoren des Klimawandels (Giannini und Giupponi, 2010; Giannini et al., 2010) verwendet.

Tabelle 7.1: Klimaäanderungsindikatoren für Niederschlag und Temperatur.
Der verwendete Schwellwert für Regentage ist 1 mm/d.

Abkürzung	Erklärung	Einheit
PFRE	Anteil Regentage	1
PREC	Gesamtniederschlagsmenge	mm
PINT	Durchschnittliche Niederschlagsmenge an Regentagen	mm/d
PQ90	90% Quantil der Niederschlagsmenge an Regentagen	mm/d
PX5D	Maximale 5-Tages Niederschlagsmenge	mm
PCDD	Längste Trockenperiode	d
T2M	Durchschnittliche 2m-Temperatur	°C
T2MIN	Durchschnittliche tägliche 2m Minimaltemperatur	°C
T2MAX	Durchschnittliche tägliche 2m Maximaltemperatur	°C

7.2 Datengrundlage

Im Folgenden werden die Daten beschrieben, welche dieser Arbeit zugrunde liegen. Es handelt sich hierbei einerseits um modellgenerierte Daten und andererseits um aus Beobachtungen generierte Daten.

7.2.1 Modelldaten

Um die regionalen Klimasimulationen zu erstellen, wurde das COSMO-CLM verwendet. Das COSMO-CLM basiert auf dem COSMO-Modell, ursprünglich als Lokal Modell vom Deutschen Wetterdienst im Jahr 1999 entwickelt (Doms und Schättler, 1999; Steppeler et al., 2003). Das COSMO Modell wird derzeit von sieben europäischen Wetterdiensten für die operationelle numerische Wettervorhersage verwendet. Eine ausführliche Dokumentation ist unter `http://www.cosmo-model.org` verfügbar. Die hier verwendete Modellkonfiguration entspricht der aus den CLM-Konsortialläufen (Hollweg et al., 2008), mit Ausnahme einer gröberen horizontalen und vertikalen Auflösung. Eine höhere Auflösung war aufgrund der Anzahl durchgeführter Simulationen nicht realisierbar. Bei den Simulationen des A1B und des B1 Szenarios im europäischen Rechengebiet wird auf die CLM-Konsortialläufe zurück gegriffen.

Um die Randbedingungen des regionalen Modells zu definieren, werden globale Modelldaten benötigt. Diese wurden entweder aus ERA40 Reanalyse Daten (Uppala et al., 2005) des *European Centre for Medium-range Weather Forecasts (ECMWF)* oder aus globalen Simulationen des gekoppelten Ozean-Atmosphäre-Modells ECHAM5/MPIOM (Roeckner et al., 2003; Jungclaus et al., 2006) gewonnen. Bei den ECHAM5/MPIOM Daten handelt es sich jeweils um den ersten Lauf der für den vierten IPCC-Sachstandsbericht verwendeten Simulationen (Roeckner et al., 2006b,c,d,e).

7.2.2 Beobachtungen

Beobachtungsdaten werden zur Modellevaluierung sowie in den untersuchten statistischen Regionalisierungsverfahren benötigt. Da in-situ-Messungen besonders in der asiatischen Region schwierig zu erhalten sind, wurden folgende, aus Stationsdaten gewonnene, Temperatur- und Niederschlagsdaten verwendet. Die meisten dieser Daten sind für wissenschaftliche Zwecke frei verfügbar und haben eine weltweite Abdeckung.

- *Climate Research Unit time-series*, Version 2.1 (CRU, Mitchell und Jones, 2005): Monatliche Temperatur- und Niederschlagsdaten auf einem globalen 0.5° Gitter für die Jahre 1901 bis 2002

- *University of Delaware* Daten, Version 1.02 (UDEL, Legates und Willmott, 1990): Monatliche Temperatur- und Niederschlagsdaten auf einem globalen 0.5° Gitter für die Jahre 1950 bis 1999

- *Global Precipitation Climatology Centre* Daten, Version 4 (GPCC, Schneider et al., 2008): Monatliche Niederschlagsdaten auf einem globalen 0.5° Gitter für die Jahre 1901 bis 2007

- Frei und Schär Datensatz, Version 4.1 (F&S, Frei und Schär, 1998): Tagesniederschlagsdaten auf einem 1/6° Gitter für die europäischen Alpen von 1971 bis 1999

- *East Asia daily precipitation data*, Version 0804 (EAD, Xie et al., 2007): Tagesniederschlagsdaten auf einem 0.5° Gitter für Ostasien für die Jahre 1980 bis 2002

- Daten des Zentrum für Geoinformatik, Salzburg (ZGIS, Kienberger et al., 2008): Ein neu entwickelter Tagestemperaturdatensatz auf einem 0.5° Gitter für beide Regionen für die Jahre 1975 bis 2000, basierend auf Stationsdaten von der Web-Seite des *National Climatic Data Center* `http://www.ncdc.noaa.gov/cgi-bin/res40.pl?page=gsod.html`, kontrolliert und kartiert durch ZGIS

Des Weiteren wurden in der Untersuchung des Indischen Monsuns folgende zusätzlichen Datensätze als Referenz verwendet:

- Beobachtungsdaten des jährlichen Monsunniederschlags in Indien (Parthasarathy et al., 1994) für die Jahre 1871 bis 2009, erstellt durch das *Indian Institute of Tropical Meteorology* (`http://www.tropmet.res.in`)

- Ausgehende langwellige Strahlung von der *National Oceanic and Atmospheric Administration* (NOAA, Lucas et al., 2001) für den Zeitraum von Juni 1974 bis Dezember 1999

- *El Niño Southern Oscillation index 3.4* Daten vom *Climate Prediction Center, NOAA, USA* (`http://www.cpc.noaa.gov/data/indices`) für die Jahre 1871 bis 2009

- Winddaten für den Zeitraum 1948 bis 2009 auf 200 hPa und 850 hPa aus dem Reanalysedatensatz 1 (Kalnay et al., 1996) der *National Centers for Environmental Prediction/National Center for Atmospheric Research*

7.3   Resultate

In einem ersten Schritt (Kapitel 2, Dobler und Ahrens, 2008) werden die Methoden anhand von täglichen Niederschlagsstatistiken in jeweils drei Regionen mit unterschiedlicher Klimatologie und Orographie in den beiden Rechengebieten (Abb. 1 und 2) verglichen. Zur Minimierung des Einflusses der Unsicherheiten im antreibenden Modell, werden die Methoden auf die globalen Reanalysedaten ERA40 des ECMWF angewendet. Aus ERA40 Daten gewonnene Antriebsdaten besitzen wesentlich kleinere Fehler als aus allgemeinen Zirkulationsmodellen gewonnene und bilden daher eine ideale Testumgebung zur Bewertung der verschiedenen Methoden.

Die statistischen Regionalisierungsverfahren sind generell erfolgreich. Die größten Fehler in den COSMO-CLM Simulationen treten während der Monsunzeit in der südasiatischen Region auf, in der das Modell die Niederschlagsintensitäten unterschätzt. Dieser Befund ist nicht überraschend, da das Modell nicht für dieses Klima und diese Region entwickelt wurde. Dennoch ist die Genauigkeit der COSMO-CLM Niederschlagsdaten auf der 0.5° Skala vergleichbar mit dem ERA40 Niederschlag und in den meisten Regionen sogar vergleichbar mit dem statistisch regionalisierten ERA40 Niederschlag.

Das COSMO-CLM ist daher eine viel versprechende Regionalisierungsmethode. Darüber hinaus besteht der Vorteil gegenüber statistischen Methoden darin, dass es eine physikalisch konsistente Reihe von verschiedenen meteorologischen Parametern erzeugt, die z.B. verwendet werden können um ein hydrologisches Modell anzutreiben.

Eine Fehlerkorrektur der COSMO-CLM Simulationen basierend auf den statistischen Methoden funktioniert sehr gut in den europäischen Testgebieten, schlägt aber fehl in Südasien. Eine genauere Untersuchung zeigt eine große Abhängigkeit der Robustheit der Modellfehlerschätzung von der beobachteten und simulierten Regentaghäufigkeit. Dies hat zur Folge, dass eine ausreichend große Anzahl Regentage in der Kalibrationsperiode der statistischen Methoden vorliegen muss, um eine bestimmte Sicherheit in der Fehlerschätzung zu gewährleisten und eine erfolgreiche Anwendung zu ermöglichen. Die Untersuchungen liefern dabei einen Schwellwert von ca. 500 Regentagen. Dadurch wird die Anwendung der statistischen Methoden in trockenen oder saisonal trockenen Klimatas stark ein-

geschränkt.

In einer zweiten Studie (Kapitel 3, Dobler und Ahrens, 2010a) wird die Darstellung des indischen Sommermonsuns (ISM) im COSMO-CLM im Vergleich zu den globalen Antriebsmodellen ERA40 und ECHAM5/MPIOM analysiert. Dazu werden diverse großskalige Indizes für den ISM untersucht. Diese basieren auf Niederschlag, vertikaler Windscherung und ausgehender langwelliger Strahlung.

Die Ergebnisse zeigen, dass bezüglich dieser Indizes die COSMO-CLM Simulationen nicht genauer sind als die antreibenden Modelle. Eine Bewertung der Modelle nur aufgrund der ISM-Indizes ist jedoch unvollständig. Fehler innerhalb der einzelnen Mittelungsregionen können einander ausgleichen und zu einer guten Übereinstimmung mit den Beobachtungsdaten führen. In der räumlichen Verteilung der Niederschläge zeigen z.B. die durch ERA40 angetriebenen COSMO-CLM Simulationen große Überschätzungen (ca. 100%) für die Westküste von Indien und Unterschätzungen (ca. 50 %) an den Ausläufern des Himalajas, welche zu einem gut mit den Beobachtungen übereinstimmenden Mittel über Indien führen. Große Modellfehler können zudem in der ausgehenden langwelligen Strahlung über dem Arabischen Meer und dem Golf von Bengalen gefunden werden. Hier zeigt das COSMO-CLM hohe konvektive Aktivität an etwa drei Mal so vielen Tagen während der Monsunzeit wie beobachtet.

In den ECHAM5/MPIOM angetriebenen Simulationen wird der Niederschlag am Fuße des Himalajas ebenfalls unterschätzt. Jedoch können die räumlichen Muster für Niederschlag und vertikale Windscherung sowie die zeitliche Korrelation der modellierten ISM-Indizes gegenüber dem ECHAM5/MPIOM verbessert werden. Diese Anwendung des COSMO-CLM liefert demnach zusätzliche Informationen, die notwendig sind für die regionale Interpretation der Ergebnisse (Beck et al., 2004). Hinsichtlich der Erstellung von regionalen Klimaprojektionen ist dies ein vielversprechendes Ergebnis, das mit den Erkenntnissen von Hagemann und Jacobs (2007) übereinstimmt, dass regionale Klimamodelle Probleme der antreibenden Modelle auf lokaler Skala kompensieren können.

Eine Sensitivitätsanalyse mit dem COSMO-CLM in der südasiatischen Region führt zum Schluss, dass die Wechselwirkung von Atmosphäre und Ozean ein entscheidender Faktor für die Modellergebnisse ist. Eine Reduktion der Meeresoberflächentemperatur im Arabischen Meer in den ERA40 angetriebenen Simulationen führt zu einer Reduktion der simulierten Westwinde in der unteren Troposphäre und dadurch zu einer geringeren Niederschlagsüberschätzung an der indischen Westküste. Weitere Untersuchungen und Entwicklungen in diesem Bereich oder die Kopplung des COSMO-CLM an ein Ozean-Modell könnten daher zu spürbaren Verbesserungen der Simulationen führen.

Um die Änderung des ISM in den COSMO-CLM und ECHAM5/MPIOM Projektionen für das 21. Jahrhundert zu untersuchen, wurden verschiedene Indizes analysiert (Kapitel 4, Dobler und Ahrens, 2010b). In den COSMO-CLM Simulationen zeigen alle Indizes eine signifikant negative Tendenz, und damit eine wesentlich geringere Stärke des ISM für die SRES-Szenarien A2, A1B und B1.

Generell können die negativsten Trends in A2 gefunden werden, gefolgt von A1B und B1. Fast keine Trends sind hingegen im *commitment* Szenario zu finden. Dies deutet auf einen negativen Einfluss der Treibhausgaskonzentrationen auf die ISM Stärke hin.

Die Verwendung von transienten Klimasimulationen von 1960 bis 2100 ermöglicht es, langfristige Variabilitäten in die Analyse mit einzubeziehen. Obwohl große jährliche Schwankungen bestehen, sind die Trends im COSMO-CLM für Niederschlagsmenge, ausgehende langwellige Strahlung und meridionale und zonale Windscherung in vielen Regionen des südasiatischen Simulationsgebietes statistisch signifikant. Für Nordwest-Indien zeigen die Projektionen teilweise einen Rückgang der Niederschläge während der Monsunzeit von über 70% während 100 Jahren. Es ist zudem zu sehen, dass die Abnahme in den Windscherungindizes hauptsächlich auf Veränderungen in der oberen Troposphäre bei 200 hPa basieren und die Veränderungen in der unteren Troposphäre nur gering sind.

Im globalen Model ECHAM5/MPIOM sind die Trends der ISM-Indizes ebenfalls negativ, mit Ausnahme des Monsunregens über Indien. Gemäß der Definitionen und aktuellen Kenntnissen über die Monsunindizes sind synchrone Trends, wie in den COSMO-CLM Simulationen, wahrscheinlicher und das regionale Model liefert hier einen weiteren Mehrwert im Vergleich zum Globalmodell.

Die COSMO-CLM Projektionen in den Einzugsgebieten der oberen Donau und des oberen Brahmaputra (Kapitel 5, Dobler et al., 2010) weisen einen signifikanten Anstieg der Temperatur für alle Jahreszeiten über den Zeitraum 1960-2100 auf. Die Temperaturzunahmen sind in der Regel größer im Brahmaputragebiet, mit den größten Werten in der Region des tibetanischen Plateaus.

Die Änderungen in den Niederschlagsstatistiken sind weniger deutlich. Es werden keine wesentlichen Veränderung in den jährlichen Niederschlagsmengen in beiden Gebieten gefunden. Allerdings zeigen die saisonalen Anteile klare Trends, beispielsweise eine Zunahme im Frühjahrsniederschlag im Einzugsgebiet der oberen Donau. In Kombination mit der projizierten erhöhten Schneeschmelze aufgrund höherer Temperaturen, würde dies intensivere und häufigere Überschwemmungen im Frühjahr bedeuten.

Die größten Trends im Niederschlag werden erneut in der Region des tibetanischen Plateaus projiziert. Hier zeigen die Simulationen einen Anstieg von bis zu 50% in der Länge der Trockenperioden in den Monaten Juni bis September, mit einem gleichzeitigen Anstieg von etwa 10% für die maximale Niederschlagsmenge an fünf aufeinander folgenden Tagen. Für die Region Assam in Indien zeigen die Projektionen eine Zunahme von 25% in der Anzahl der aufeinander folgenden trockenen Tage während der Monsunzeit und somit eine signifikante Verlängerung der Monsunpausen.

7.4 Schlussfolgerungen

Die in dieser Arbeit angestellten Untersuchungen führen zum Schluss, dass die Anwendung des COSMO-CLM die Möglichkeit liefert, globale Klimamodelle in den beiden untersuchten Gebieten zu regionalisieren und zusätzliche regionale Informationen bereit zu stellen. Für Mitteleuropa stellt das COSMO-CLM eine geeignete Methode dar, um Niederschlags- und Temperaturfelder zu erzeugen.

Um akkurate Antriebsdaten für hydrologische oder andere Anschlussmodelle zu generieren, kann zudem eine statistische Fehlerkorrektur von Niederschlag und Temperatur verwendet werden. Für statistische Regionalisierungsverfahren und Fehlerkorrekturen gilt jedoch, dass im Falle weniger Datenpunkte (wie z.B. bei Extremereignissen) eine große Unsicherheit in der Schätzung der statistischen Zusammenhänge zwischen Simulationen und Beobachtungen entsteht. Regionale Klimamodelle besitzen diesen Nachteil zwar nicht, eine Modellevaluierung und Feinabstimmung wird dadurch aber ebenfalls erschwert.

Für Südasien ist eine Fehlerkorrektur von Niederschlag und Temperatur aufgrund momentan vorliegender Modelleinschränkungen im COSMO-CLM notwendig, um z.B. geeignete hydrologische Antriebsdaten zu erstellen. Im Falle des Niederschlags sollte diese aber nur für die Monate Juni bis September angewendet werden, um die Limitierung durch wenige Regentage zu überwinden.

Eine allgemeine Aussage darüber, welche der untersuchten Methoden am besten geeignet ist für die Regionalisierung globaler Klimamodelle, lässt sich nicht treffen. Die Anwendung der Methoden auf Reanalysedaten liefert zwar die Möglichkeit einer quantitativen Einordnung der Methoden, diese Einordnung ist jedoch nicht auf allgemeine Klimamodelle übertragbar. Die Evaluierung anhand Reanalysedaten ist notwendig um die Methoden zu testen aber nicht ausreichend um eine erfolgreiche Anwendung zu gewährleisten.

Bei statistischen Methoden mit Fehlerkorrekturen führen große Modellfehler in der Kalibrationszeit zu einer starken Korrektur der Modelldaten in der Anwendungsperiode und beinhalten so ein hohes Risiko einer Verschlechterung der modellierten Daten. Damit die Methoden erfolgreich angewendet werden können, müssen die Modellfehler zudem zeitlich konstant sein, um eine robuste Fehlerschätzung zu ermöglichen. Eine Weiterentwicklung von globalen und regionalen Klimamodellen ist daher auch notwendig, um adäquate Daten für statistische Methoden zu generieren, da die heutigen Modelle diesen Anforderungen oft nicht genügen. Für das COSMO-CLM zeigen die Untersuchungen dieser Arbeit, dass eine Änderung in der Parametrisierung der Konvektion und das Koppeln an ein Ozeanmodell wahrscheinlich zu verbesserten Resultaten führen würden.

References

Ahrens, B.: Evaluation of precipitation forecasting with the limited area model ALADIN in an alpine watershed, Meteor. Z., 12, 245–255, 2003.

Ahrens, B., Jasper, K., and Gurtz, J.: On ALADIN precipitation modeling and validation in an Alpine watershed, Ann. Geophys., 21, 627–637, 2003.

Aksoy, H.: Use of gamma distribution in hydrological analysis, Turk. J. Engin. Environ. Sci., 24, 419–428, 2000.

Annamalai, H., Hamilton, K., and Sperber, K. R.: The South Asian Summer Monsoon and its Relationship with ENSO in the IPCC AR4 Simulations, J. Climate, 20, 1071–1092, doi:10.1175/JCLI4035.1, 2007.

Ashfaq, M., Shi, Y., Tung, W. W., Trapp, R. J., Gao, X., Pal, J. S., and Diffenbaugh, N. S.: Suppression of south Asian summer monsoon precipitation in the 21st century, Geophys. Res. Lett., 36, doi:10.1029/2008GL036500, 2009.

Basistha, A., Arya, D. S., and Goel, N. K.: Analysis of historical changes in rainfall in the Indian Himalayas, Int. J. Climatol., 29, 555–572, doi:10.1002/joc.1706, 2009.

Bates, B., Kundzewicz, Z., Wu, S., and Palutikof, J., eds.: Climate change and water, IPCC Technical Paper, IPCC Secretariat, Geneva, Switzerland, 2008.

Beck, A., Ahrens, B., and Stadlbacher, K.: Impact of nesting strategies in dynamical downscaling of reanalysis data, Geophys. Res. Lett., 31, doi:10.1029/2004GL020115, 2004.

Böhm, U., Kücken, M., Ahrens, W., Block, A., Hauffe, D., Keuler, K., Rockel, B., and Will, A.: CLM - the climate version of LM: Brief description and long-term applications, Tech. Rep. 6, COSMO Newsletter, 2006.

Chen, H., Ding, Y. H., and He, J. H.: Reappraisal of Asian summer monsoon indices and the long-term variation of monsoon, Acta Meteor. Sinica, 21, 168–178, 2007.

Dobler, A. and Ahrens, B.: Precipitation by a regional climate model and bias correction in Europe and South Asia, Meteor. Z., 17, 499–509, 2008.

Dobler, A. and Ahrens, B.: Analysis of the Indian summer monsoon system in the regional climate model COSMO-CLM, J. Geophys. Res., 115, D16101, doi:10.1029/2009JD013497, 2010.

Dobler, A., Yaoming, M., Sharma, N., Kienberger, S., and Ahrens, B.: Regional climate projections in two alpine river basins: Upper Danube and Upper Brahmaputra, Adv. Sci. Res., submitted, 2010.

Doms, G. and Schättler, U.: The nonhydrostatic limited-area model LM of DWD. Part 1: Scientific documentation, available at: http://www.cosmo-model.org, 1999.

Duffy, P. B., Govindasamy, B., Iorio, J. P., Milovich, J., Sperber, K. R., Taylor, K. E., Wehner, M. F., and Thompson, S. L.: High-resolution simulations of global climate, part 1: Present climate, Clim. Dynam., 21, 371–390, 2003.

Flohn, H.: Elements of a synoptic climatology of the Indo-Pakistan subcontinent, in: Investigations on the Indian monsoon climate, edited by Flohn, H., vol. 14 of *Bonn. Meteor. Abh.*, pp. 5–28, Ferd. Dümmlers Verlag, 1970.

Frei, C. and Schär, C.: A precipitation climatology of the Alps from high-resolution rain-gauge observations, Int. J. Climatol., 18, 873–900, 1998.

Frei, C., Christensen, J., Deque, M., Jacob, D., Jones, R., and Vidale, P.: Daily precipitation statistics in regional climate models: Evaluation and intercomparison for the European Alps, J. Geophys. Res., 108, doi:10.1029/2002JD002287, 2003.

Gadgil, S.: The Indian monsoon and its variability, Annu. Rev. Earth Planet. Sci., 31, 429–467, 2003.

Gadgil, S., Vinayachandran, P. N., Francis, P. A., and Gadgil, S.: Extremes of the Indian summer monsoon rainfall, ENSO, and equatorial Indian Ocean oscillation, Geophys. Res. Lett., 31, doi:10.1029/2004GL01973, 2004.

Giannini, V. and Giupponi, C.: Integration by identification of indicators, Adv. Sci. Res., submitted, 2010.

Giannini, V., Giupponi, C., Hutton, C., Allan, A. A., Kienberger, S., Flügel, W. F., Ceccato, L., et al.: Development of likely "what if?" IWRM scenarios, Adv. Sci. Res., submitted, 2010.

Giorgi, F.: Regional climate modeling: Status and perspectives, J. Phys. IV France, 139, 101–118, doi:10.1051/jp4:2006139008, 2006.

Giorgi, F., Hewitson, B., Christensen, J. H., Hulme, M., von Storch, H., Whetton, P., Jones, R., Mearns, L., and Fu, C.: Regional climate information – Evaluation and projections, pp. 583–638, Climate Change 2001: The scientific basis, contribution of working group I to the third assessment report of the Intergovernmental Panel on Climate Change (IPCC), Cambridge University Press, 2001.

Goswami, B. N.: Comments on Choice of south Asian summer monsoon indices, Bull. Amer. Meteor. Soc., 81, 821–822, 2000.

Goswami, B. N., Krishnamurthy, V., and Annamalai, H.: A broad-scale circulation index for the interannual variability of the Indian summer monsoon, Quart. J. Roy. Meteor. Soc., 125, 611–633, 1999.

Goswami, B. N., Wu, G., and Yasunari, T.: The Annual Cycle, Intraseasonal Oscillations, and Roadblock to Seasonal Predictability of the Asian Summer Monsoon, J. Climate, 19, 5078–5099, 2006.

Hagemann, S. and Jacob, D.: Gradient in the climate change signal of European discharge predicted by a multi-model ensemble, Climate Change, 81, Supplement 1: 309–327, 2007.

Hagemann, S., Arpe, K., and Bengtsson, L.: Validation of the hydrological cycle in ERA-40, Tech. rep., ECMWF, 2005.

Hay, L. E., Wilby, R. L., Gutowski, W. J., Leavesley, G. H., Pan, Z., Arritt, R. W., Takle, E. S., and Clark, M. P.: Use of Regional Climate Model Output for Hydrologic Simulations, J. Hydrometeor., 3, 571–590, 2002.

Hollweg, H. D., Böhm, U., Fast, I., Hennemuth, B., Keuler, K., Keup-Thiel, E., Lautenschlager, M., Legutke, S., Radtke, K., Rockel, B., Schubert, M., Will, A., Woldt, M., and Wunram, C.: Ensemble simulations over Europe with the regional climate model CLM forced with IPCC AR4 global scenarios, Tech. Rep. 3, SGA-ZMAW Hamburg, 2008.

Ines, A. V. M. and Hansen, J. W.: Bias correction of daily GCM rainfall for crop simulation studies, Agric. For. Meteor., 138, 44–53, 2006.

IPCC: Climate Change 2007: Synthesis Report. Contribution of Working Groups I, II and III to the Fourth Assessment Report of the Intergovernmental Panel on Climate Change [Core Writing Team, Pachauri, R.K , A. Reisinger (eds.)], IPCC, 2007a.

IPCC: Climate Change 2007: The Physical Science Basis, Contribution of Working Group I to the Fourth Assessment Report of the Intergovernmental Panel on Climate Change [Core Writing Team, Solomon, S., Qin, D., Manning, M.,

Chen, Z., Marquis, M., Averyt, K. B., Tignor, M., and Miller, H. L (eds.)], IPCC, 2007b.

Jaeger, E. B., Anders, I., Luethi, D., Rockel, B., Schär, C., and Seneviratne, S. I.: Analysis of ERA40-driven CLM simulations for Europe, Meteor. Z., 17, 349–367, 2008.

Jones, C., Gregory, J., Thorpe, R., Cox, P., Murphy, J., Sexton, D., and Valdes, H.: Systematic optimization and climate simulation of FAMOUS, a fast version of HADCM3, Hadley Centre Technical Note, 60, 33, 2004.

Ju, J. and Slingo, J. M.: The Asian summer monsoon and ENSO, Quart. J. Roy. Meteor. Soc., 121, 1133–1168, 1995.

Jungclaus, J. H., Keenlyside, N., Botzet, M., Haak, H., Luo, J. J., Latif, M., Marotzke, J., Mikolajewicz, U., and Roeckner, E.: Ocean circulation and tropical variability in the coupled model ECHAM5/MPI-OM, J. Climate, 19, 3952–3972, 2006.

Kain, J. S. and Fritsch, J. M.: A one-dimensional entraining de-training plume model and its application in convective parameterization, J. Atmos. Sci., 23, 2784–2802, 1993.

Kalnay, E., Kanamitsu, M., Kistler, R., Collins, W., Deaven, D., Gandin, L., Iredell, M., Saha, S., White, G., Woollen, J., Zhu, Y., Chelliah, M., Ebisuzaki, W., Higgins, W., Janowiak, J., Mo, K. C., Ropelewski, C., Wang, J., Leetmaa, A., Reynolds, R., Jenne, R., and Joseph, D.: The NCEP/NCAR 40-year reanalysis project, Bull. Amer. Meteor. Soc., 77, 437–471, 1996.

Kessler, E.: On the Distribution and Continuity of water substance in the atmospheric circulations, Meteor. Monogr. 10, Amer. Met. Soc., Boston, 1969.

Kienberger, S., Tiede, D., Ungersböck, M., Klug, H., and Ahrens, B.: Interpolation of daily temperature values for european and asian test-areas, in: Geospatial Crossroads @ GI_Forum '08., edited by Car, A., Griesebner, G., and Strobl, J., pp. 164–169, Wichmann Verlag, 2008.

Kothe, S., Dobler, A., Beck, A., and Ahrens, B.: The radiation budget in a regional climate model, Clim. Dynam., doi:10.1007/s00382-009-0733-2, in press, 2010.

Kripalani, R. and Kulkarni, A.: Climatic impact of El Niño/La Nina on the Indian monsoon: A new perspective, Weather, 52, 39–46, 1997.

Kripalani, R., Oh, J. H., Kulkarni, A., Sabade, S. S., and Chaudhari, H. S.: South Asian summer monsoon precipitation variability: Coupled climate model

simulations and projections under IPCC AR4, Theor. Appl. Clim., 90, 133–159, doi:10.1007/s00704-006-0282-0, 2007.

Krishnan, R., Mujumdar, M., Vaidya, V., Ramesh, K. V., and Satyan, V.: The abnormal Indian summer monsoon of 2000, J. Climate, 16, 1177–1194, 2003.

Kumar, K. K., Rajagopalan, B., and Cane, M. A.: On the weakening relationship between the Indian monsoon and ENSO, Science, 284, 2156–2159, 1999.

Kumar, K. R., Sahai, A. K., Kumar, K. K., Patwardhan, S. K., Mishra, P. K., Revadekar, J. V., Kamala, K., and Pant, G. B.: High-resolution climate change scenarios for India for the 21st century, Curr. Sci., 90, 334–345, 2006.

Lang, S., Kääb, A., Pechstädt, J., Flügel, W. A., Zeil, P., Lanz, E., Kahuda, D., Frauenfelder, R., Casey, K., Füreder, P., Sossna, I., Wager, A., Janauer, G., Exler, N., Boukalova, Z., Tapa, R., Lui, J., and Sharma, N.: Assessing components of the Natural Environment of Upper Danube and Upper Brahmaputra River Basins, Adv. Sci. Res., submitted, 2010.

Legates, D. R. and Willmott, C. J.: Mean seasonal and spatial variability in gauge-corrected, global precipitation, Int. J. Climatol., 10, 111–127, 1990.

Liebmann, B. and Smith, C. A.: Description of a complete (interpolated) outgoing longwave radiation dataset, Bull. Amer. Meteor. Soc., 77, 1275–1277, 1996.

Lim, Y. K., Kim, K. Y., and Lee, H. S.: Temporal and Spatial Evolution of the Asian Summer Monsoon in the Seasonal Cycle of Synoptic Fields, J. Climate, 15, 3630–3644, 2002.

Lucas, L. E., Waliser, D. E., Xie, P., Janowiak, J. E., and Liebmann, B.: Estimating the satellite equatorial crossing time biases in the daily, global outgoing longwave radiation dataset, J. Climate, 14, 2583–2605, 2001.

Lucas-Picher, P., Christensen, J. H., Saeed, F., Kumar, P., Asharaf, S., Ahrens, B., Wiltshire, A., Jacob, D., and Hagemann, S.: Can regional climate models represent the Indian monsoon?, J. Hydrometeor., submitted, 2010.

Meehl, G. A., Covey, C., Delworth, T., Latif, M., McAvaney, B., Mitchell, J. F. B., Stouffer, R. J., and Taylor, K. E.: The WCRP CMIP3 multi-model dataset: A new era in climate change research, Bull. Amer. Meteor. Soc., 88, 1383–1394, 2007.

Mitchell, T. D. and Jones, P. D.: An improved method of constructing a database of monthly climate observations and associated high-resolution grids, Int. J. Climatol., 25, 693–712, 2005.

Murphy, J.: An evaluation of statistical and dynamical techniques for downscaling local climate, J. Climate, 12, 2256–2284, 1999.

Nakicenovic, N. and Swart, R.: Special Report on Emissions Scenarios, Cambridge, UK: Cambridge University Press, p. 612, 2000.

Parthasarathy, B., Kumar, K. R., and Kothawale, D. R.: Indian-summer monsoon rainfall indexes - 1871-1990, Meteor. Mag., 121, 174–186, 1992.

Parthasarathy, B., Munot, A. A., and Kothawale, D. R.: All-India monthly and seasonal rainfall series - 1871-1993, Theor. Appl. Clim., 49, 217–224, 1994.

Patra, P. K., Behera, S. K., Herman, J. R., Maksyutov, S., Akimoto, H., and Yamagata, T.: The Indian summer monsoon rainfall: interplay of coupled dynamics, radiation and cloud microphysics, Atmos. Chem. Phys., 5, 2181–2188, 2005.

Prasch, M., Marke, T., Strasser, U., and Mauser, W.: Large scale integrated hydrological modelling of the impact of climate change on the water balance with DANUBIA, Adv. Sci. Res., submitted, 2010.

Rasmusson, E. M. and Carpenter, T. H.: Variations in tropical sea surface temperature and surface wind fields associated with the Southern Oscillation/El Niño, Mon. Wea. Rev., 110, 354–384, 1982.

Ritter, B. and Geleyn, J. F.: A comprehensive radiation scheme for numerical weather prediction models with potential applications in climate simulations, Mon. Wea. Rev., 120, 303–325, 1992.

Rockel, B. and Geyer, B.: The performance of the regional climate model CLM in different climate regions, based on the example of precipitation, Meteor. Z., 17, 487–498, doi:10.1127/0941-2948/2008/0297, 2008.

Roeckner, E., Bäuml, G., Bonaventura, L., Brokopf, R., Esch, M., Giorgetta, M., Hagemann, S., Kirchner, I., Kornblueh, L., Manzini, E., Rhodin, A., Schlese, U., Schulzweida, U., and Tompkins, A.: The atmospheric general circulation model ECHAM 5. PART I: Model description, 2003.

Roeckner, E., Lautenschlager, M., and Schneider, H.: IPCC-AR4 MPI-ECHAM5_T63L31 MPI-OM_GR1.5L40 20C3M run no.1: atmosphere monthly mean values MPImet/MaD Germany, Tech. rep., World Data Center for Clim., doi:10.1594/WDCC/EH5-T63L31_OM-GR1.5L40_20C_1_MM, 2006a.

Roeckner, E., Lautenschlager, M., and Schneider, H.: IPCC-AR4 MPI-ECHAM5_T63L31 MPI-OM_GR1.5L40 SRESA1B run no.1: atmosphere 6 HOUR values MPImet/MaD Germany, Tech. rep., World Data Center for Clim., doi:10.1594/WDCC/EH5-T63L31_OM-GR1.5L40_A1B_1_6H, 2006b.

Roeckner, E., Lautenschlager, M., and Schneider, H.: IPCC-AR4 MPI-ECHAM5_T63L31 MPI-OM_GR1.5L40 SRESA2 run no.1: atmosphere 6 HOUR values MPImet/MaD Germany, Tech. rep., World Data Center for Clim., doi:10.1594/WDCC/EH5-T63L31_OM-GR1.5L40_A2_1_6H, 2006c.

Roeckner, E., Lautenschlager, M., and Schneider, H.: IPCC-AR4 MPI-ECHAM5_T63L31 MPI-OM_GR1.5L40 SRESB1 run no.1: atmosphere 6 HOUR values MPImet/MaD Germany, Tech. rep., World Data Center for Clim., doi:10.1594/WDCC/EH5-T63L31_OM-GR1.5L40_B1_1_6H, 2006d.

Roeckner, E., Lautenschlager, M., and Schneider, H.: IPCC-AR4 MPI-ECHAM5_T63L31 MPI-OM_GR1.5L40 20C3M run no.1: atmosphere 6 HOUR values MPImet/MaD Germany, Tech. rep., World Data Center for Clim., doi: 10.1594/WDCC/EH5-T63L31_OM-GR1.5L40_20C_1_6H, 2006e.

Salathé, E. P.: Comparison of various precipitation downscaling methods for the simulation of streamflow in a rainshadow river basin, Int. J. Climatol., 23, 887–901, doi:10.1002/joc.922, 2003.

Schmidli, J., Frei, C., and Vidale, P. L.: Downscaling from GCM precipitation: A benchmark for dynamical and statistical downscaling methods, Int. J. Climatol., 26, 679–689, doi:10.1002/joc.1287, 2006.

Schneider, U., Fuchs, T., Meyer-Christoffer, A., and Rudolf, B.: Global Precipitation Analysis Products of the GPCC, DWD internet publication, GPCC, 2008.

Schrodin, E. and Heise, E.: A New Multi-Layer Soil Model, Tech. Rep. 2, COSMO Newsletter, 2002.

Steppeler, J., Doms, G., Schättler, U., Bitzer, H., Gassmann, A., Damrath, U., and Gregoric, G.: Meso-gamma scale forecasts using the nonhydrostatic model LM, Meteor. Atmos. Phys., 82, 75–96, doi:10.1007/s00703-001-0592-9, 2003.

Takle, E. S., Roads, J., Rockel, B., Gutowski, J. W. J., Arritt, R. W., Meinke, I., Jones, C. G., and Zadra, A.: Transferability intercomparison - An opportunity for new insight on the global water cycle and energy budget, Bull. Amer. Meteor. Soc., 88, 375–384, doi:10.1175/BAMS-88-3-375, 2007.

Taylor, K. E.: Summarizing multiple aspects of model performance in a single diagram, J. Geophys. Res., 106, 7183–7192, 2001.

Tiedtke, M.: A comprehensive mass flux scheme for cumulus parameterization in large-scale models, Mon. Wea. Rev., 117, 1779–1800, 1989.

Uppala, S. M., Kallberg, P. W., Simmons, A. J., Andrae, U., Bechtold, V. D., Fiorino, M., Gibson, J. K., Haseler, J., Hernandez, A., Kelly, G. A., Li, X., Onogi, K., Saarinen, S., Sokka, N., Allan, R. P., Andersson, E., Arpe, K., Balmaseda, M. A., Beljaars, A. C. M., Van De Berg, L., Bidlot, J., Bormann, N., Caires, S., Chevallier, F., Dethof, A., Dragosavac, M., Fisher, M., Fuentes, M., Hagemann, S., Holm, E., Hoskins, B. J., Isaksen, L., Janssen, P. A. E. M., Jenne, R., McNally, A. P., Mahfouf, J. F., Morcrette, J. J., Rayner, N. A., Saunders, R. W., Simon, P., Sterl, A., Trenberth, K. E., Untch, A., Vasiljevic, D., Viterbo, P., and Woollen, J.: The ERA-40 re-analysis, Quart. J. Roy. Meteor. Soc., 131, 2961–3012, 2005.

van Ulden, A. P. and van Oldenborgh, G. J.: Large-scale atmospheric circulation biases and changes in global climate model simulations and their importance for climate change in Central Europe, Atmos. Chem. Phys., 6, 863–881, 2006.

von Storch, H., Langenberg, H., and Feser, F.: A spectral nudging technique for dynamical downscaling purposes, Mon. Wea. Rev., 128, 3664–3673, 2000.

Walker, G. T.: Correlation in seasonal variations of weather II, Mem. of Ind. Meteor. Dep., 21, 22–45, 1910.

Walker, G. T.: Correlation in seasonal variations of weather VIII: A preliminary study of world weather, Mem. of Ind. Meteor. Dep., 24, 75–131, 1923.

Wang, B.: Comments on Choice of south Asian summer monsoon indices - Reply, Bull. Amer. Meteor. Soc., 81, 822–824, 2000.

Wang, B. and Fan, Z.: Choice of south Asian summer monsoon indices, Bull. Amer. Meteor. Soc., 80, 629–638, 1999.

Webster, P. J. and Yang, S.: Monsoon and ENSO - selectively interactive systems, Quart. J. Roy. Meteor. Soc., 118, 877–926, 1992.

Webster, P. J., Magana, V. O., Palmer, T. N., Shukla, J., Tomas, R. A., Yanai, M., and Yasunari, T.: Monsoons: Processes, predictability, and the prospects for prediction, J. Geophys. Res., 103, 14 451–14 510, 1998.

Widmann, M., Bretherton, C., and Salathe, E.: Statistical precipitation downscaling over the Northwestern United States using numerically simulated precipitation as a predictor, J. Climate, 16, 799–816, 2003.

Wilby, R. L. and Wigley, T. M. L.: Downscaling general circulation model output: a review of methods and limitations, Prog. Phys. Geo., 21, 530–548, 1997.

Wood, A., Leung, L., Sridhar, V., and Lettenmaier, D.: Hydrologic implications of dynamical and statistical approaches to downscaling climate model outputs, Climate Change, 62, 189–216, 2004.

Xie, P., Yatagai, A., Chen, M., Hayasaka, T., Fukushima, Y., Liu, C., and Yang, S.: A gauge-based analysis of daily precipitation over East Asia, J. Hydrometeor., 8, 607–627, 2007.

Xu, C.: From GCMs to river flow: a review of downscaling methods and hydrologic modelling approaches, Prog. Phys. Geo, 23, 229–249, 1999.

List of Figures

List of Tables

Appendix
The radiation budget in a regional climate model

The radiation budget in a regional climate model

Steffen Kothe · A. Dobler · A. Beck ·
B. Ahrens

Abstract The long- and short-wave components of the
radiation budget are among the most important quantities
in climate modelling. In this study, we evaluated the
radiation budget at the earth's surface and at the top of
atmosphere over Europe as simulated by the regional cli-
mate model CLM. This was done by comparisons with
radiation budgets as computed by the GEWEX/SRB
satellite-based product and as realised in the ECMWF re-
analysis ERA40. Our comparisons show that CLM has a
tendency to underestimate solar radiation at the surface and
the energy loss by thermal emission. We found a clear
statistical dependence of radiation budget imprecision on
cloud cover and surface albedo uncertainties in the solar
spectrum. In contrast to cloud fraction errors, surface
temperature errors have a minor impact on radiation budget
uncertainties in the long-wave spectrum. We also evaluated
the impact of the number of atmospheric layers used in
CLM simulations. CLM simulations with 32 layers per-
form better than do those with 20 layers in terms of the
surface radiation budget components but not in terms of the
outgoing long-wave radiation and of radiation divergence.
Application of the evaluation approach to similar simula-
tions with two additional regional climate models

confirmed the results and showed the usefulness of the
approach.

Keywords Regional climate modelling ·
Radiation budget · Evaluation

1 Introduction

Regional climatic features such as the orography, lakes,
complex coastlines, and heterogeneous land use are better
captured by regional climate models (RCMs) than by
global climate models (GCMs). Therefore RCMs provide
better understanding of regional climatic processes
(Giorgi et al. 1990; Frei et al. 2003; Leung et al. 2003;
Beck et al. 2004; Dobler and Ahrens 2008). In the present
study, we evaluate CLM (the COSMO-model in climate
version; see http://www.clm-community.eu/), a regional
non-hydrostatic limited-area climate model, in terms of
the radiation budget.

The long- and short-wave components of the earth's
radiation budget are important terms in climate modelling,
describing the sources and sinks of energy in the earth-
atmosphere system. These terms govern the energy balance
of the earth and control daily and annual cycles. Thus, it is
necessary to evaluate the radiation budget of regional cli-
mate models and to identify sources of uncertainties.

Many studies use ground station data to evaluate the
results of RCMs or GCMs because of their well-known
accuracy (e.g. Wyser et al. 2008; Markovic et al. 2008;
Tjernström et al. 2008; Wild 2008). For example, the
accuracy of Baseline Surface Radiation Network direct solar
irradiance measurements is ± 2 W/m^2 (Ohmura et al. 1998).
But, there are only a limited number of radiation stations
with climatic time series of the short- and long-wave

S. Kothe (✉)
LOEWE Biodiversity and Climate Research Centre,
Frankfurt am Main, Germany
e-mail: kothe@iau.uni-frankfurt.de

S. Kothe · A. Dobler · B. Ahrens
Institute for Atmospheric and Environmental Sciences,
Goethe-University Frankfurt, Frankfurt am Main, Germany

A. Beck
Central Institute for Meteorology and Geodynamics,
Vienna, Austria

components of radiation and thus only a poor spatial data coverage. Other studies employ re-analysis data, whose main advantage is the spatial coverage and the availability of surface (SFC) and top of atmosphere (TOA) parameters (e.g. Vidale et al. 2003; Hagemann et al. 2004; Marras et al. 2007; Jaeger et al. 2008). For ERA15 data (Gibson et al. 1997), the predecessor of the European Centre for Medium-Range Weather Forecasts (ECMWF) ERA40 re-analysis (Uppala et al. 2005), Wild et al. (1998) demonstrate good agreement of surface radiation with ground station data. Reichler and Kim (2008) investigate different re-analysis datasets and show that there are uncertainties especially in radiative quantities, but that the ERA40 dataset agrees best with ground station observations.

In the present study, we use the ERA40 and additionally the satellite-based GEWEX/SRB datasets as references. The GEWEX/SRB dataset has previously been used to evaluate model results (e.g. Shmakin et al. 2002; Winter and Eltahir 2008), and we anticipate that the additional use of the quasi-observational SRB dataset, in this study, provides more robust conclusions.

A comparison of CLM simulations and ERA15 re-analysis data indicates a significant underestimation of the net short- and long-wave radiation at the surface (downward radiation counts positive and upward radiation negative), which is attributed to an overestimation of cloud cover (Jaeger et al. 2008). Another study that compares the surface radiation budget over North America of an RCM with ground station measurements also associates uncertainties in incoming short-wave radiation with imprecision in cloud cover simulations (Markovic et al. 2008). For downwelling long-wave radiation, Markovic et al. (2008) conclude that all-sky errors are significantly influenced by cloud-free radiation, cloud emissivity, and cloud cover errors. Wild et al. (2001) report similar results in their comparison of the downwelling long-wave radiation of different GCMs and ground-based measurements under cloud-free and all-sky conditions. They attribute biases in all-sky conditions primarily to errors in the clear-sky downwelling long-wave radiation. Hence, besides interactions with clouds the absorption within the atmosphere has also a significant effect on uncertainties in radiation modelling. The absorption in the atmosphere is strongly determined by water vapour, which is closely linked to the temperature in the lower troposphere and thus correlated with the surface temperature.

Besides errors in cloud cover and surface temperature we expect an important impact of errors in the simulation of surface albedo on the radiation budget. Thus, in addition to quantification of errors in the simulated radiation budget components, we also investigate the impact of errors in parameters such as cloud cover, surface albedo, and surface temperature. Additionally, we compare CLM

simulations using either 20 or 32 vertical atmospheric layers. Using 20 or 32 vertical layers is a relative small change in model setup, but of potentially large impact. First of all it is believed that better vertical resolution with 32 layers improves the results. But, most of the parameterizations in the model, for example the Tiedtke mass flux scheme (Tiedtke 1989), were originally developed and tested for smaller layer numbers. Therefore, it is of interest to evaluate both setups and check if our evaluation approach is sensitive to the differences in the simulations.

First, we provide a brief description of the model setup and datasets and afterwards present in Sect. 4 comparisons of CLM20 (20 layers), CLM32 (32 layers), ERA40, and GEWEX/SRB. In Sect. 5 we then describe our investigation of the relationship between net radiation errors and errors in cloud fraction, surface albedo, and surface temperature. In the last section, we discuss the significance of our results for regional climate modelling. Attached are two appendices, which generalise our results. The first appendix applies simulations by two additional RCMs and the second one applies a conceptual model.

2 Model description and setup

The CLM is a state-of-the-art non-hydrostatic regional climate model developed for application in climate simulations up to several centuries in duration with spatial grid spacings from 50 to 1 km. The CLM is the climate version of the COSMO-model (see http://www.cosmo-model.org) that is used for operational mesoscale weather forecasting. Since completion of the first climate version of the CLM (summer of 2002), there has been a steadily growing community of users and developers (see http://www.clm-community.eu).

In this study we investigated two climate simulations done with version 2.4.11 of the CLM. Except for the horizontal resolution and number of vertical layers, the setup for these two simulations was identical to that used for the so-called CLM consortial runs (Hollweg et al. 2008). Both simulations were driven by ERA40 at the lateral boundaries for the years 1958–2001. The computational domain covered Europe and parts of Northern Africa, with a grid dimension of 91×97 grid points and a grid spacing of $0.44°$. This was the computational domain applied as a standard domain in the EU-project ENSEMBLES (Hewitt and Griggs 2004; www.ensembles-eu.org). The only difference between the two simulations was the number of atmospheric layers: 20 for CLM20 and 32 for CLM32.

Radiative transfer in the CLM is parameterized with a δ-two-stream radiation scheme (Ritter and Geleyn 1992) for short- and long-wave fluxes in a plane parallel and

horizontally homogeneous atmosphere. It is solved for three intervals in the solar spectrum and five intervals in the thermal spectrum. In the radiative transfer calculation of CLM, the influence of cloud water droplets, cloud ice crystals, water vapour, ozone, carbon dioxide, and other minor trace gases and aerosols is accounted for. Radiative transfer depends strongly on input provided by other model components such as the cloud scheme. The fractional cloud cover, which significantly influences radiation, is determined by an empirical function that depends on the relative humidity, height of the model layer, and convective activity. The effective radii of the hydrometeors are prescribed. For cloud microphysics, the CLM offers four different variants. For the applied CLM simulations, we used a microphysical scheme with snow but without cloud ice or graupel. Convection is parameterized following Tiedtke (1989).

Parameters, such as soil type, soil moisture, and plant cover, determine the CLM solar surface albedo. These parameters were derived from datasets such as CORINE, GLC2000, GLOBE, or the Digital Soil Map of the World from the FAO (see Smiatek et al. 2008). The maximum of the surface albedo is set to 0.7 (snow cover and sea ice) and the minimum to 0.07 (water). Further details on the dynamics and physics of the model are given in Böhm et al. (2006), Steppeler et al. (2003) and in the model documentation (www.cosmo-model.org).

3 Reference data

3.1 ERA40

ERA40 is a re-analysis data product of the ECMWF. It is a global gridded dataset with a horizontal spectral resolution of T159 (about 125 km) and 60 vertical levels. ERA40 produces analyses at 6 h intervals from 1958 to 2001 (Uppala et al. 2005). In the present study, we used monthly means that were derived from 18 h forecasts starting at 00 UTC and 12 UTC from the re-analyses and discarding the leading 6 h to account for model spin-up. In addition to monthly mean radiation fluxes, we also used monthly means of ERA40 cloud fraction, surface albedo, and surface temperature. In the evaluation of short-wave fluxes, we applied a monthly mean cloud fraction derived from daylight values (averages data where the sun is above the horizon, just as short-wave fluxes).

3.2 GEWEX/SRB

The GEWEX/SRB (Surface Radiation Budget) project provides a satellite-based dataset of short- and long-wave radiation components at the earth surface and TOA on a global scale (Pinker and Laszlo 1992). Here, we used version 2.81 of the dataset (which covers July 1983 to June 2005 with 3-hourly, daily, monthly/3-hourly (e.g. monthly mean 12 UTC), and monthly averages) with a global grid spacing of 1° (Gupta et al. 2006). The surface radiation fluxes were evaluated in a variety of studies with data of the BSRN (Baseline Surface Radiation Network) or the GEBA (Global Energy Balance Archive) project, which provided good agreement with monthly data, i.e. within 5 W/m^2 for long-wave fluxes and within 5–20 W/m^2 for short-wave fluxes (Gupta et al. 1999; Zhang et al. 2006, 2007, 2009). In the present study, we used SRB radiation and cloud fraction data. The surface albedo was determined as the ratio of up- and downwelling solar surface fluxes. Cloud fraction data were averaged over the daylight periods for comparisons with the short-wave radiative components, and were averaged over the whole day for comparisons with long-wave radiative components. The cloud fraction data, included in SRB, originate from the ISCCP (International Satellite Cloud Climatology Project) and were already used in other climate model evaluation studies (Ahrens et al. 1998). Monthly means were derived by averaging 3-hourly instantaneous values.

3.3 CRU

For SRB, no consistent temperature dataset was available. Thus, we employed the ERA40 surface temperatures over sea and CRU (Climate Research Unit) temperatures over land. The CRU dataset (version TS 2.1) provides monthly mean global gridded surface temperature data with 0.5° resolution (Mitchell and Jones 2005).

3.4 Comparison OF GEWEX/SRB and ERA40 data

We compared the monthly fluxes of SRB and ERA40 in Europe (from 1983 to 2001) to estimate the uncertainty of the reference data, which was essential to know to assess the comparisons with CLM. Because of the different grid spacing of SRB (1°), ERA40 (about 125 km), and CLM (0.44°), we interpolated all data to the same grid with 1° grid spacing. This interpolation was performed with simple inverse distance weighting. SRB monthly means of radiation fluxes were calculated by averaging 3-hourly instantaneous values, but ERA40 and CLM monthly means were calculated by accumulated values. This yielded sampling differences, which were approximately corrected by application of a factor to the SRB data. This factor is the ratio of the 1-hourly and 3-hourly averaged local solar irradiance at TOA assuming that the hourly average is a much better approximation of the means from accumulated fluxes than a 3-hourly average.

For surface net short-wave radiation (SNS), the comparison of SRB and ERA40 mostly showed small monthly mean differences within ±10 W/m^2, with slightly higher values for SRB fluxes. The total mean differences are small, as displayed in Fig. 1. This figure illustrates the biases of SRB and ERA40 in reference to the mean of SRB and ERA40. In general the difference was small, but SRB showed larger SNS values than ERA40 especially in the Mediterranean area. ERA40 realised larger TOA net short-wave radiation fluxes (TNS) than SRB.

The agreement of ERA40 and SRB for surface net long-wave radiation (SNL) was quite good, generally within about ±1 W/m^2 (Fig. 1). In most parts of Europe the differences were close to zero. The SRB data had less negative values than ERA40 over the Mediterranean Sea, while ERA40 had less negative values over the Iberian Peninsula and North Africa. The difference between SRB and ERA40 for TOA net long-wave radiation (TNL) was largest in the winter, with a mean difference of −12 W/m^2. Thus, on average, SRB outgoing long-wave radiation at TOA is higher than for ERA40, except for Southern Europe and North Africa, where ERA40 had similar or higher values.

Therefore, there was a substantial uncertainty in the reference data, especially in the TOA fluxes (Fig. 1). A comparison of cloud fraction showed that SRB predicted more clouds than ERA40, with a maximum spatial mean difference of 0.1 in summer. However, regional differences could be as large as 0.25. Throughout the year, there was a clear meridional gradient in the differences, with larger ERA40 values in northern regions and larger SRB values in southern regions (especially over the Mediterranean Sea).
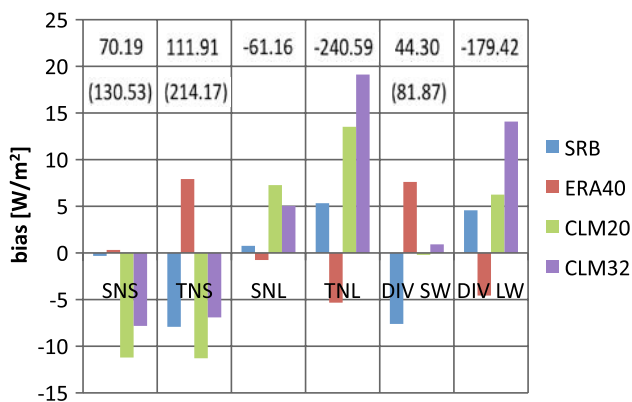
The SRB surface albedo was slightly larger than the ERA40 surface albedo in most parts of Europe.

4 Radiation budget evaluation

In this section we compared the CLM20, CLM32, GEWEX/SRB, and ERA40 datasets by using monthly mean data from 1983 to 2001 on a 1° grid. The CLM simulation domain placed limits on the area of comparison. We excluded a five-degree lateral boundary buffer zone of the CLM domain from all comparisons. Furthermore, as indicated by the comparison to ERA40 data, there were some uncertain pixels in the SRB dataset in the northern parts of the domain during winter, which were excluded from the comparisons. Because of the viewing geometry of satellites in northern regions in winter, we believed that satellite-based algorithms could produce some unrealistic values in these regions.

Figure 1 provides a general overview of our results. It provides the biases with reference to the average of SRB and ERA40 data. The short-wave components in Fig. 1 were derived from whole-day means just as the long-wave components. This simplifies the direct comparison of short- and long-wave biases and their potential compensation. The numbers in Fig. 1 show the mean values of the reference and additionally in brackets for short-wave the corresponding values for daylight means. All other short-wave values shown below were derived from daytime means. The displayed biases of short- and long-wave divergences given in the figure indicate biases in the differences between TOA and SFC fluxes.

4.1 Surface net short-wave radiation (SNS)

Figure 1 shows that SRB and ERA40 had a larger long-term mean SNS than CLM20 and CLM32. The underestimation by CLM was highest from April to August with spatial mean differences up to −30 W/m^2. In the winter months, the underestimation decreased to differences less than −10 W/m^2. Throughout the year, the largest differences (up to −60 W/m^2) were over the Mediterranean Sea. This can be seen in Fig. 2 (left and middle), but the differences are smaller compared to ERA40 than to SRB. These results are consistent with those of Jaeger et al. (2008), who found summer biases in SNS of up to −60 W/m^2 using 32 levels, at least compared to ERA15.

Overall, the values of CLM32 were larger than those of CLM20. The spatial mean difference ranged from less than 4 W/m^2 (January and December) to more than 8 W/m^2 (April). Again, the largest differences occured over the Mediterranean Sea in Winter and over the Atlantic Ocean in Summer (more than 25 W/m^2; Fig. 2, right). In

Fig. 1 Biases of SRB, ERA40, CLM20, CLM32 relative to (ERA40 + SRB)/2 for SNS, TNS, SNL, TNL, short-wave divergence, and long-wave divergence (for the whole investigation area and time period 07/1983–12/2001). Short-wave values were derived from whole-day means just as long-wave. The numbers show the mean value of the reference in W/m^2. For short-wave there are in brackets the mean values for daylight means
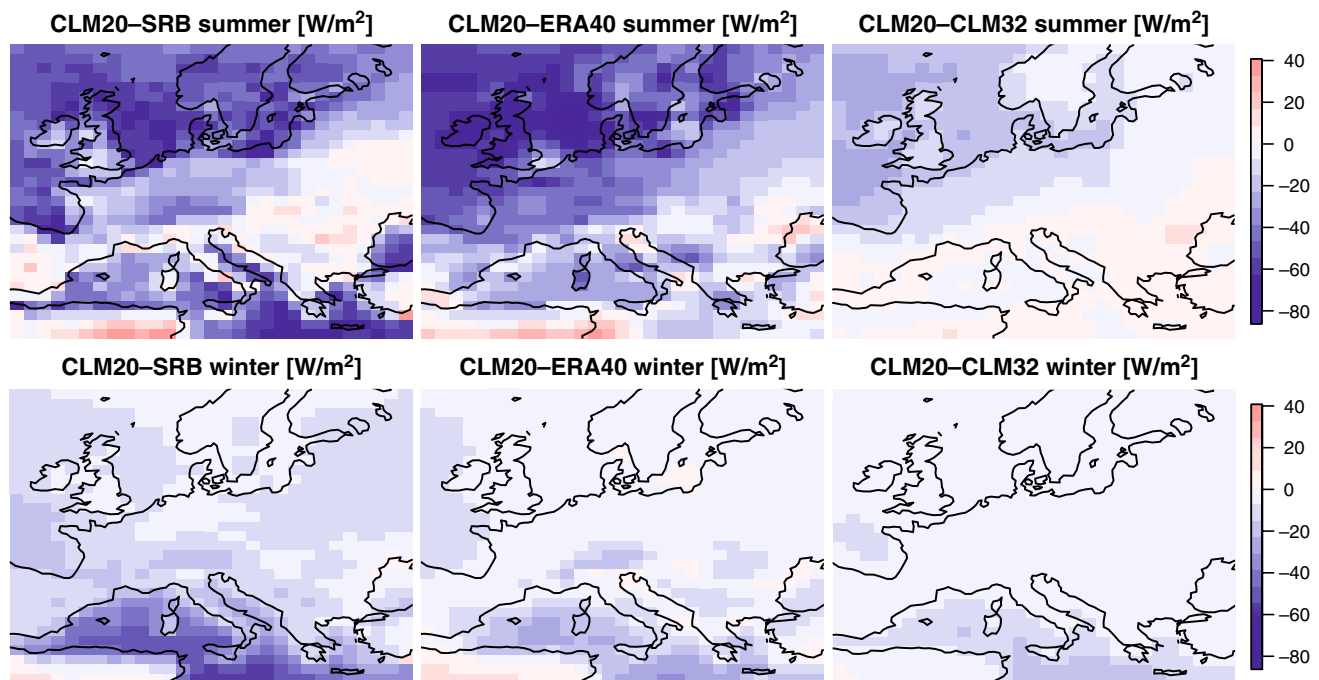
Fig. 2 Differences of SNS [W/m²] (derived from daytime means) in summer (JJA, *upper row*) and winter (DJF, *lower row*) for CLM20 minus SRB (*left*), CLM20 minus ERA40 (*middle*), and CLM20 minus CLM32 (*right*). All values are means for the whole time period 07/1983–12/2001

consequence the CLM32 underestimation compared to the reference was more than 30% smaller than the CLM20 underestimation (Fig. 1).

4.2 TOA net short-wave radiation (TNS)

The TNS reference was much more uncertain than the SNS reference as discussed above. The shown biases in Fig. 1 indicate that the mean TNS of CLM and SRB agrees very well, whereas ERA40 has a much higher mean. But, despite the reference uncertainty, Fig. 1 shows that CLM tends to underestimate TNS. The spatial mean differences were much larger compared to ERA40 (about −11 W/m² in January and December; more than −50 W/m² in April to June) than to SRB (about −2 W/m² in January and December; about −12 W/m² in April to August). In autumn and winter, the largest differences were over the Mediterranean Sea; in spring and summer, the greatest differences were in Northern Europe, in the area around the British Islands, and in Scandinavia (Fig. 3, left and middle). Because satellites directly observe TOA radiation, we expected SRB TNS to be more reliable than ERA40 TNS. Therefore, the CLM performance seemed to be better than the ERA40 performance.

The TNS differences between CLM20 and CLM32 were similar to the SNS differences. With an about 40% lower mean underestimation with respect to the reference (see Fig. 1), CLM32 yielded better results than CLM20.

4.3 Surface net long-wave radiation (SNL)

Figure 1 indicates that the mean SNL difference between CLM and the reference data was relatively small. CLM slightly overestimates SNL indicating that CLM underestimated thermal loss of energy at the surface.[1] The spatial mean difference ranged from about 2–12 W/m², whereas the mean difference compared to SRB had a minimum in winter and a maximum in September, while compared to ERA40 the largest differences occured in April and October and the minimum in July.

There was good agreement between CLM20 and CLM32, with spatial mean differences ranging from 4 W/m² (winter) to −2 W/m² (July). The largest differences were around the British Islands (Fig. 4, right). Over the Mediterranean Sea, differences of about 10 W/m² occured only in winter. In summary, although the differences were small, CLM32 provided better results than did CLM20 relative to the reference (the mean difference decreased by about 30%, see Fig. 1), except for the Mediterranean in summer.

4.4 TOA net long-wave radiation (TNL)

Despite some differences in the references, CLM clearly overestimated TNL (i.e. underestimates TOA outgoing

---

[1] Remind that downward radiation is counted positive and upward radiation is counted negative.
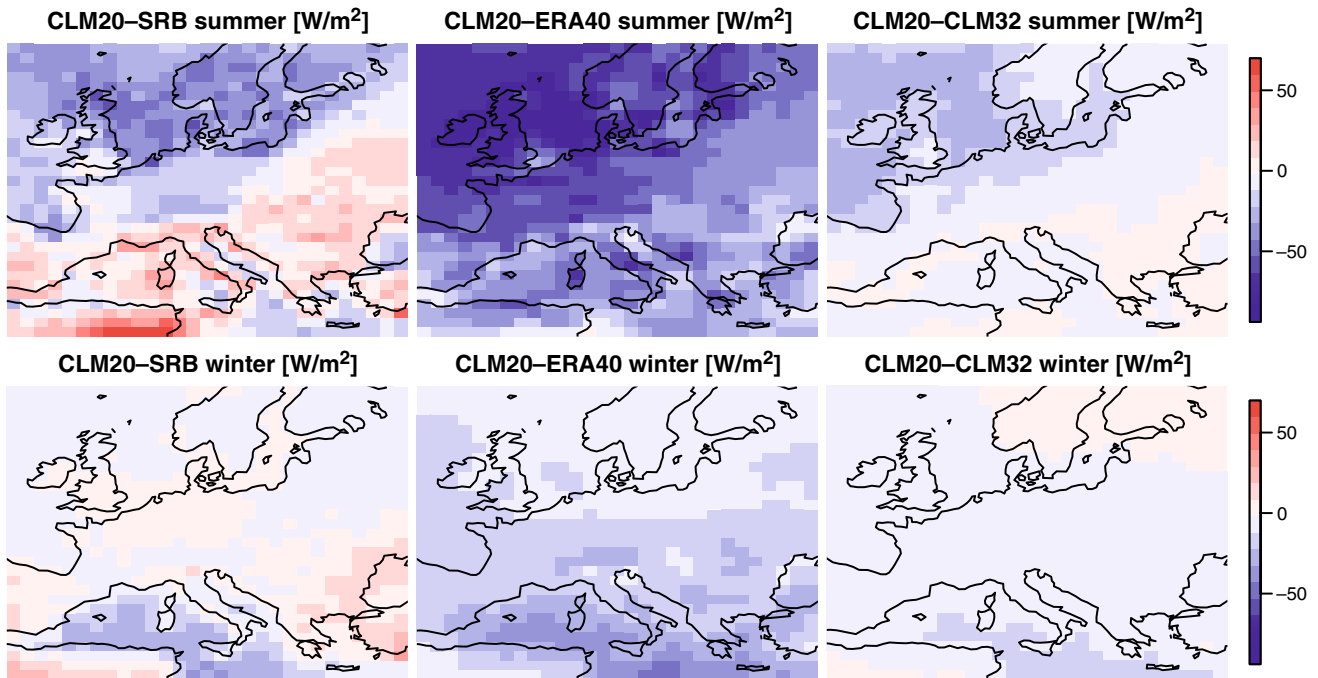
Fig. 3 The same as Fig. 2 but for TNS
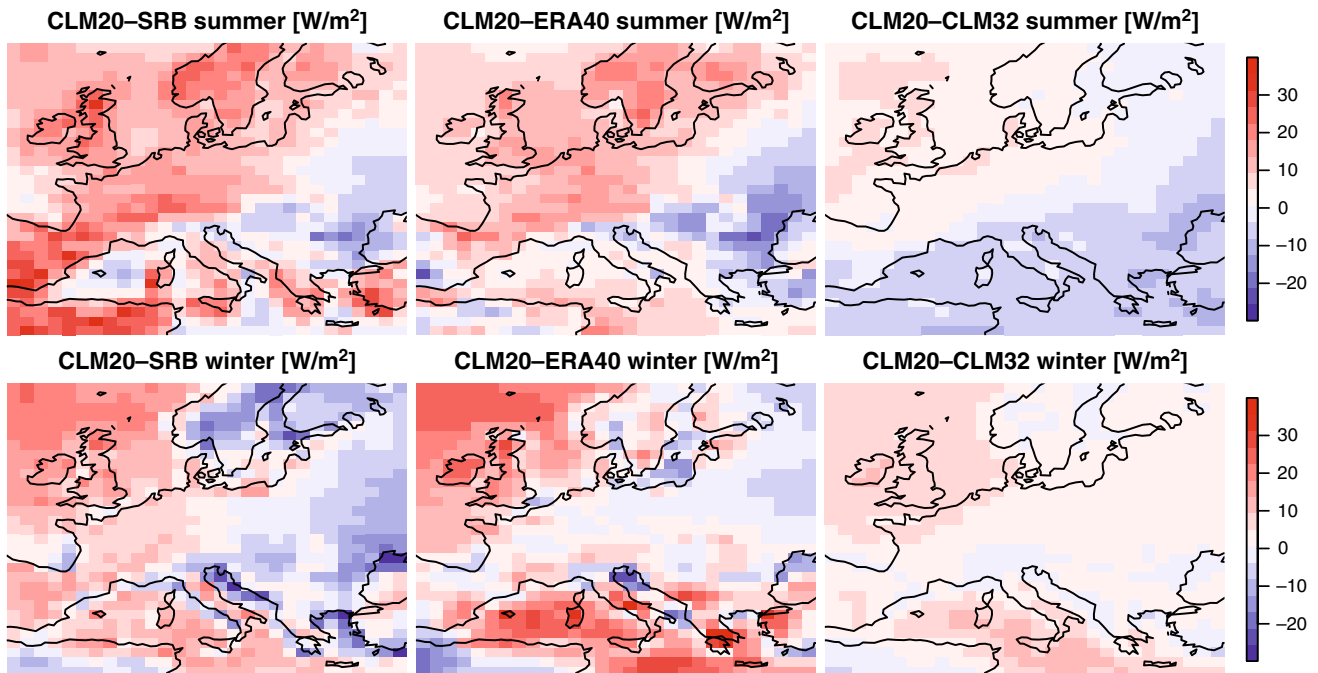
Fig. 4 Differences of SNL [W/m^2] in summer (JJA, *upper row*) and winter (DJF, *lower row*) for CLM20 minus SRB (*left*), CLM20 minus ERA40 (*middle*), and CLM20 minus CLM32 (*right*)

long-wave radiation). The annual cycle of the spatial mean differences to SRB data ranged from 8 W/m^2 (winter) to more than 12 W/m^2 (May). The largest differences to ERA40 data were in winter (about 20 W/m^2). Figure 5 (left and middle) shows that CLM20 overestimated TNL in

almost the entire evaluation domain with maximum differences over the Mediterranean Sea and Scandinavia.

For TNL, CLM20 yielded smaller spatial mean TNL values (up to 7 W/m^2) than CLM32. The spatial distribution (Fig. 5, right) showed that the smallest differences are
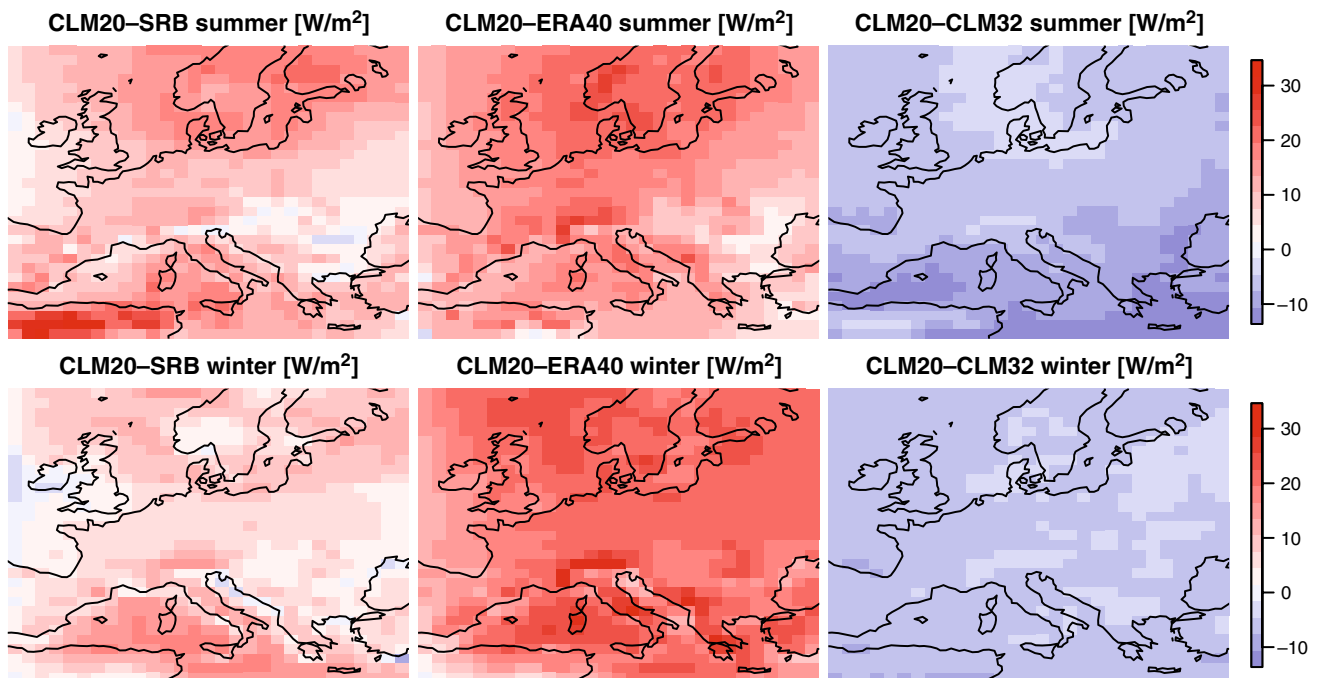
Fig. 5 The same as Fig. 4 but for TNL

around the British Islands, Scandinavia, and central Europe, and that the largest differences were in the southeast part of the Mediterranean Sea. A decrease in mean overestimation of about 35% (see Fig. 1) for TNL showed that the results of CLM20 were better than those of CLM32.

4.5 Discussion of comparisons

A comparison of CLM with SRB and ERA40 showed a clear underestimation of net incoming short-wave radiation and net outgoing long-wave radiation. The magnitude of the found biases was comparable to the biases of other regional climate models discussed in the Appendix 1 and given in Fig. 10. In the total radiation budget these CLM errors partly compensated. At the surface, SNS was too low, possibly because of underestimation of solar downwelling radiation caused by an overestimation of cloud cover or atmospheric absorption. Another possible reason might be an overestimation of short-wave upwelling radiation resulting from errors in the surface albedo. Similar effects could explain the large underestimation of TNS. In this context it has to be mentioned that Jaeger et al. (2008, 2009) state that clear-sky radiation and surface albedo are reasonably modelled in CLM. We discussed the potential error sources in more detail in the next section. For the short-wave divergence it was impossible to judge the quality of CLM because of a large evaluation uncertainty (Fig. 1).

The bias in SNL might result from an underestimation of surface emission caused by errors in surface temperature or from errors in cloud cover. The same effects might be responsible for the underestimation of TNL. Furthermore, the results showed that CLM32 had smaller errors than CLM20 in most of the radiation components (except for TNL and the divergences). But, as shown by Fig. 1, after integration (SNS + SNL, respectively, TNS + TNL) the errors compensate and it cannot be concluded that one model version is superior. Nevertheless, CLM32 performed better over sea (as Figs. 2, 3, 4, 5 indicate).

5 Impact of cloud fraction, surface albedo, and surface temperature

Based on the results of previous studies (see discussion in Sect. 1), we expected that cloud fraction (CFR), surface albedo (ALB), and surface temperature (TS) are the main factors influencing the radiation components of CLM. Simple comparisons of CFR, ALB, and TS of the different datasets confirmed this expectation. For example, the spatial allocations of differences in short-wave net radiation are often co-located with differences in CFR. Especially over the ocean, there seemed to be a correlation between CFR overestimation and SNS underestimation. However, there were also regions where errors in CFR seemed not to be the main cause of errors in SNS.

The connection between errors in ALB and SNS or TNS was not as obvious as for CFR. Nevertheless, there were geographic areas with seasonally dependent correlations between underestimations of SNS and overestimations of ALB. Contrary to our expectations, there was no pronounced correlation between errors in TS and SNL or TNL.

Here, we provide a quantification of the impact of the errors ΔCFR, ΔALB and ΔTS (the difference between the respective CLM and reference values) on the net radiation fluxes. This requires that the results are comparable at different geographical latitudes. Thus, we normalised the shortwave fluxes with the factor $1/(4\sin\theta)$, where θ is the solar elevation angle.

Figure 6 (top left) shows the dependence of errors in SNS on errors in CFR and ALB. If ΔCFR = 0, the error in SNS increases from about -30 W/m^2 to about 20 W/m^2 as ΔALB decreases. If ΔCFR and ΔALB were positive (meaning that CLM predicts too many clouds and an excessively high surface albedo), SNS was underestimated. The analogous figure for TNS looks very similar (Fig. 6 top right).

Assuming linear relationship between the errors, the squared correlation coefficient R^2 is a measure of the explained error variance. The explained variances for SNS

(Fig. 7) indicated that the error in CFR plays a more important role than the ALB error and that the combination of ΔALB and ΔCFR is responsible for the largest part of the error in SNS. The highest values of explained variance for ΔALB were during the winter and spring over land, whereas the contribution of ΔALB to variance over the ocean was smaller. For ΔCFR, the largest values of R^2 were during the autumn and winter. Figure 8 shows that the explained variance had large regional differences. For ΔALB, high values of R^2 occured during winter in an area from the Alps to nearly all of Eastern Europe. These are regions with frequent winter snow cover (see for example: http://www.dwd.de/snowclim) with high albedos and albedo uncertainties. R^2 values for ΔCFR were largest in the Mediterranean Sea throughout the year and around the British Islands in spring and summer.

The sensitivity of ΔTNS to ΔCFR was similar to that of ΔSNS, whereas the sensitivity of ΔTNS to ΔALB was lower. Again, the influence of errors in ALB over the sea was very low. The seasonal and regional distribution of R^2 for ΔCFR and ΔALB was similar to that of SNS.

A simple calculation confirmed these results for SNS and TNS (see Appendix 2, Table 2). An increase in CFR or ALB led to a negative bias in net short-wave radiation, and

Fig. 6 Differences of monthly means (07/1983–12/2001) of CLM minus ERA40 SNS (derived from daytime means) and TNS (*upper row*) against errors in ALB and CFR and for SNL and TNL (*lower row*) against errors in TS and CFR. In this figure, the SNS error was averaged within boxes with a side length of 0.04 units for CFR and ALB and 0.25 K for TS. The Figure bases on single grid points over the whole area without coast pixels
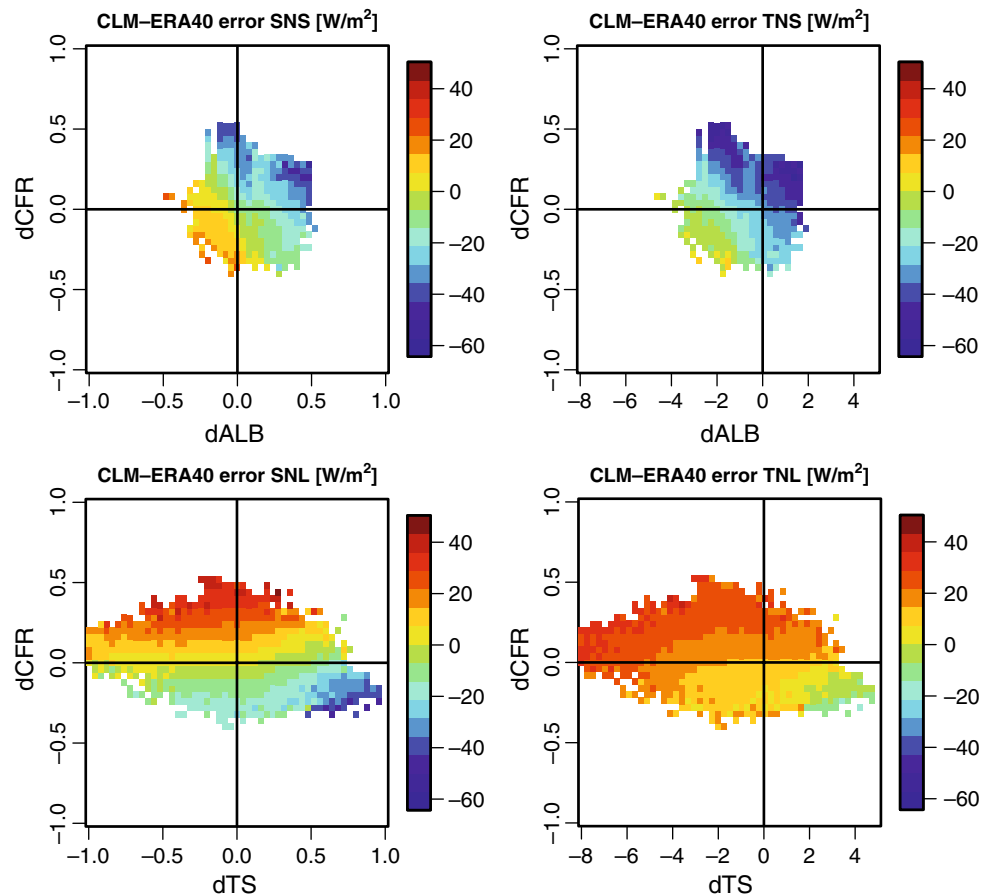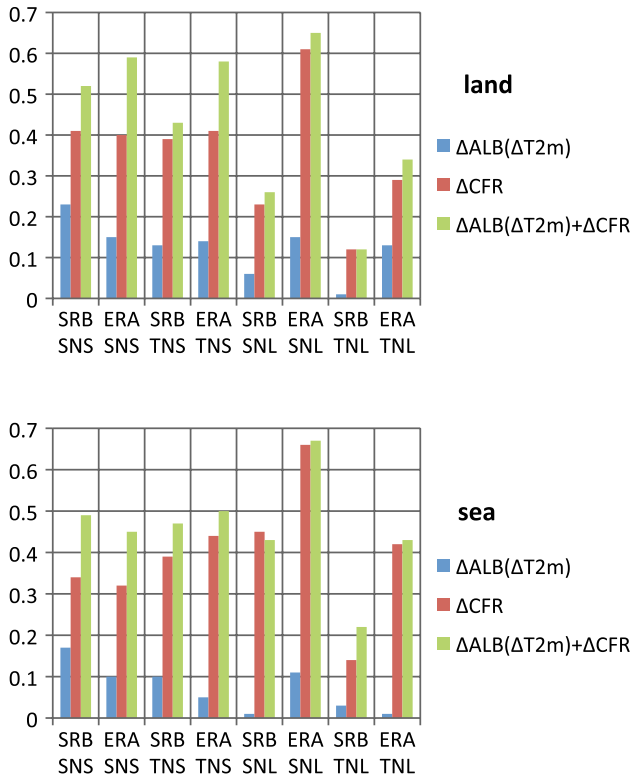
Fig. 7 Explained variances of radiation errors relative to errors in CFR, ALB, TS and the according combinations ΔALB + ΔCFR and ΔTS + ΔCFR, for land (*top*) and sea (*bottom*). The values are means for the whole investigation area and time period 07/1983–12/2001

the ΔCFR impact was in case of typical errors a multiple than that of ΔALB. A similar calculation for the long-wave net radiation showed that errors in CFR had a large effect on errors in the net long-wave radiation (Appendix 2, Table 3). We assumed that TS is another important factor for net long-wave radiation, but this simple calculation showed that for typical errors the impact of TS is low compared to the impact of CFR.

This was pictured by the CLM results. Figure 6 (bottom left) shows a clear dependence of the error in SNL on ΔCFR and a small dependence on ΔTS. As mentioned above, for SRB the ERA40 TS was used over sea and CRU TS over land. Using ERA40 TS over land instead of CRU TS changed the R^2 values only slightly (within ± 0.02).

In combination, Fig. 6 (bottom and top panels) shows that there is a partial compensation of errors in the net short- and long-wave radiation. Whereas for SNS, a positive error in ΔCFR and ΔALB was mainly associated with a negative error in net radiation, a positive error in ΔCFR and ΔTS for SNL was associated with a positive error in net radiation. Figure 7 shows that for SNL, there were small values of R^2 for ΔTS. However, ERA40 had large values of explained variance for SNL over both land and ocean. These high levels of explained variance resulted from a high sensitivity to ΔCFR. The R^2 value of about 0.15 over land for ΔTS (Fig. 7) with ERA40 was because of relatively large R^2 values in summer over Eastern

Fig. 8 Explained variance of SNS in winter (mean 1983–2001) of errors in SNS and ALB (denoted by ΔSNS $\sim$ ΔALB) and errors in SNS and CFR (denoted by ΔSNS $\sim$ ΔCFR) for SRB (*top*) and ERA40 (*bottom*)
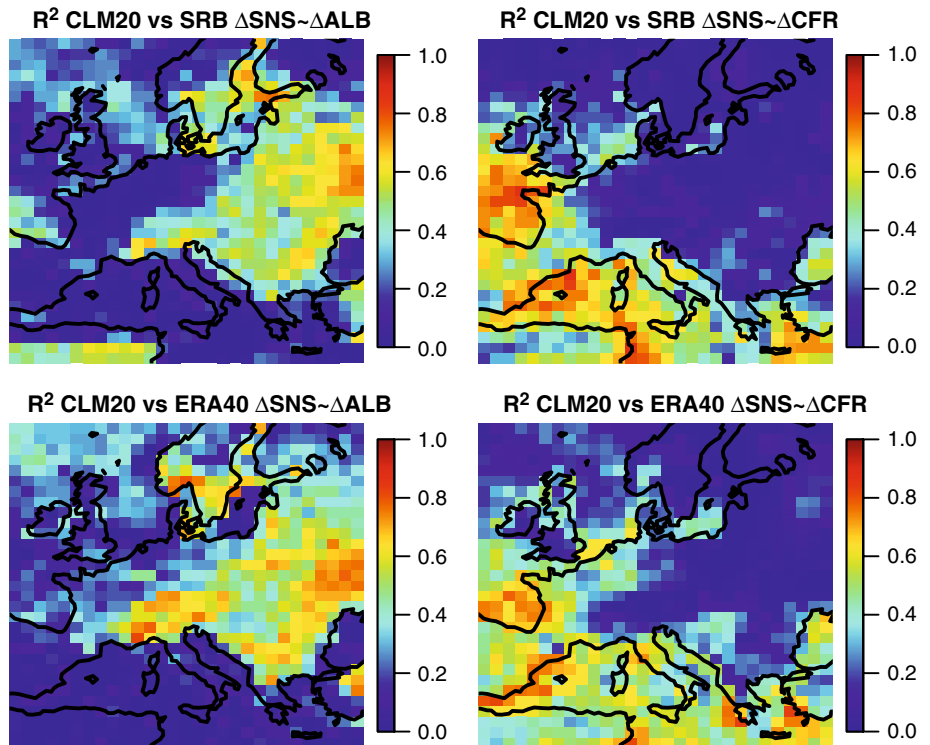
Europe (Fig. 9). In all other seasons, the variance explained by ΔTS was very low. A possible reason for the higher R^2 values in case of ERA40 than in case of SRB was that the radiation fluxes and the TS reference applied in the SRB comparison might be inconsistent. Compared with SNL, the explained variance of TNL was even lower.

In summary, ΔCFR and ΔALB explain about 50% of the error variance in the solar spectrum. In the long-wave spectrum ΔCFR was of less importance compared to short-wave (besides in the comparison against ERA40 in case of SNL), and the impact of TS errors on the radiation budget was small (except for the summer season with generally smaller cloud fractions). These results were confirmed by a investigation of two other state-of-the-art regional climate models (see Appendix 1). Obviously, there were more influential errors especially in the long-wave spectrum, but a better representation of CFR and ALB will substantially improve the computation of radiation budgets in CLM.
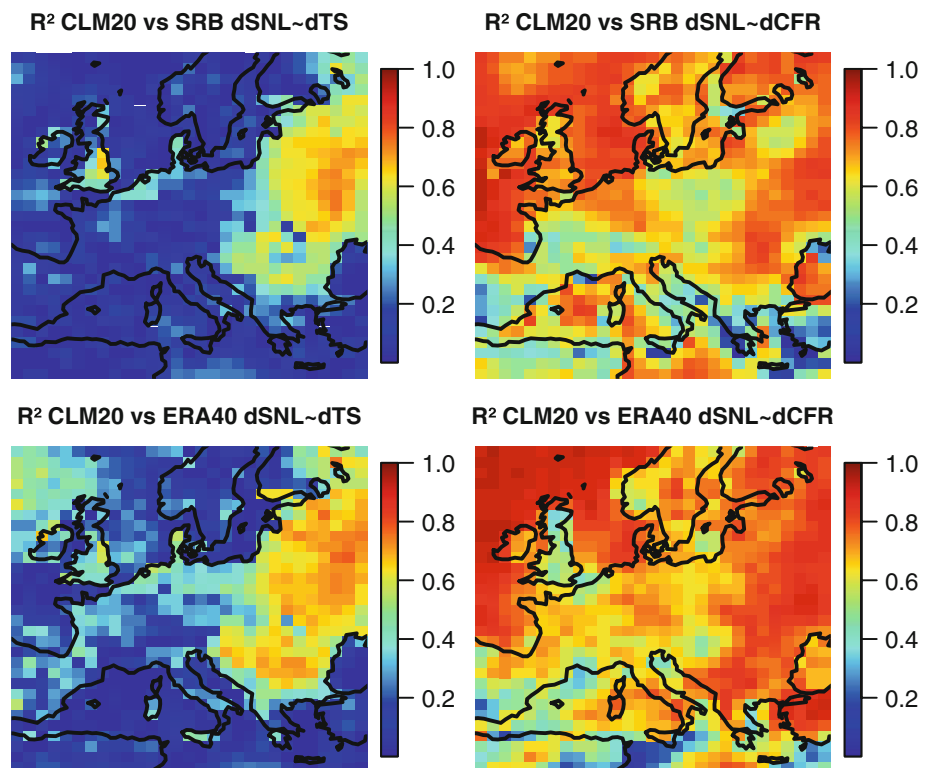
6 Conclusions

The main goal of this study was to quantify uncertainties in the short- and long-wave components of the radiation budget for CLM simulations using the satellite-based GEWEX/SRB dataset and the ERA40 re-analysis dataset as references. Our comparisons showed considerable underestimations of the net short-wave radiation in large parts of

Europe, especially over ocean areas. Over land, the differences of CLM to SRB were smaller than to ERA40. For TNS, an overall underestimation of CLM was found, whereas SRB showed a slight overestimation in southern parts of Europe. In particular, for the TOA components, the satellite-based SRB dataset was expected to be more reliable than the ERA40 dataset. Overall, the CLM results were quite satisfactory, if the evaluation uncertainties due to the differences in the reference datasets were considered. The CLM overestimated SNL in most areas, but underestimates SNL in some parts of Eastern Europe. Overestimation of TNL was even larger, especially in comparison with ERA40. But again, these differences were not very large with respect to the difference between the reference datasets.

We also investigated the effect of the number of atmospheric layers used in CLM simulations. We found that the climate simulation with 32 layers yielded (except for TNL and long-wave divergence) better results. The use of 32 layers considerably reduced the biases (up to 40%) in the radiation components. However, the improvement was relatively small if compared to the evaluation uncertainties and if the long- and short-wave compensation effects are considered (Fig. 1). Therefore, with respect to computational costs and evaluation uncertainties, the use of 20 atmospheric layers is a considerable option in terms of the radiation budget. Nevertheless, the evaluation approach applied in this paper relies on generally available data and

Fig. 9 Explained variance of SNL in summer (mean 1983–2001) of errors in SNL and TS (denoted by ΔSNL $\sim \Delta$TS) and errors in SNL and CFR (denoted by ΔSNL $\sim \Delta$CFR) for SRB (*top*) and ERA40 (*bottom*)

R² CLM20 vs SRB dSNL~dTS

R² CLM20 vs SRB dSNL~dCFR

R² CLM20 vs ERA40 dSNL~dTS

R² CLM20 vs ERA40 dSNL~dCFR

helps in the evaluation of model differences (CLM20, CLM32, and the additional models REMO and ALADIN in Appendix 1) and will support the evaluation of CLM in other parts of the world in a future study.

Finally, we also estimated possible sources of errors with respect to possible approaches for model improvement. It was expected, that the main error sources in radiation components would be errors in CFR, ALB, and TS. For net short-wave radiation, we confirmed that ΔCFR and ΔALB are important factors; the explained variance for ΔCFR was two- to threefold higher than for ΔALB. The large seasonal and geographic differences also had to be considered. Errors in CFR led to substantial biases in the net long-wave radiation. However, we found that ΔTS had only a small or even negligible influence on errors in the net long-wave radiation budget. In a comparison to simulations of the regional climate models REMO and ALADIN we could confirm the found relations. Thus, a better representation of cloud fraction CFR and surface albedo ALB yields a substantially better estimation of the radiation budget components by CLM. It is worth to wrestle with these relatively simple parameters compared to parameters like cloud inhomogeneity, cloud phase, direct and indirect aerosol effects, etc.

Appendix 1: Results compared to other regional climate models

To see how our results with the regional model CLM compare to results with other regional climate models, we investigated simulations with the REMO regional climate model of the Max Planck Institute for Meteorology (Hamburg, Germany) (Jacob et al. 2001, 2007) and the ALADIN in climate mode of the Centre National de Recherches Météorologiques (Toulouse, France) (Sanchez-Gomez et al. 2008; Radu et al. 2008). These two regional climate models were applied in the EU-project ENSEMBLES (Hewitt and Griggs 2004) and we have analysed the corresponding simulations for Europe. The used simulations were ERA40 driven with a horizontal resolution of 0.5°. The REMO used 27 and ALADIN used 31 vertical layers, respectively.
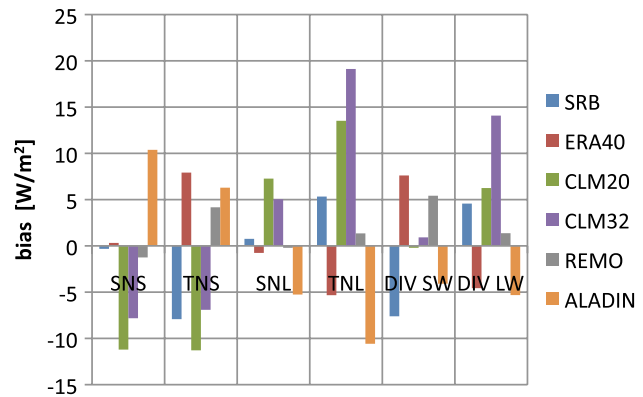

Fig. 10 Same figure as Fig. 1 but additionally with biases of REMO and ALADIN

The model bias of REMO (Fig. 10) relatively to SRB and ERA40 was small and for all parameters within the uncertainty range of the reference data. Opposite to CLM there was a small overestimation of TNS, which led to a larger solar divergence error than quantified for CLM. The model bias of ALADIN (Fig. 10) was of similar magnitude as of CLM, but in all cases with the opposite algebraic sign. Thus, ALADIN showed an overestimation of short-wave net radiation and an underestimation of long-wave net radiation. This shows that our evaluation approach is useful in identification of inter-model difference in radiation budget components.

In terms of the identification of error sources the pattern of the dependence of flux errors on errors in the explaining quantities CFR, ALB, and TS in general was similar for all investigated models and setups (CLM20, CLM32, REMO, ALADIN). Figure 11 (upper panels) shows a strong dependence of the SNS differences in REMO and ALADIN on errors in CFR and ALB. For SNL (Fig. 11, lower panels) there was also a strong dependence on errors in CFR, while there was no dependence on errors in TS. These results compare very well to the results shown for CLM in Fig. 6.

The explained variances (not shown) also yielded similar results as those displayed for CLM in Fig. 7. Errors in CFR explain two to three times more than errors in ALB of the error variance in solar fluxes. For ALADIN explained variances for errors in ALB were with a range of about 11–22% clearly higher than for errors in TS, with a range of 0–7%. For REMO the values of explained variance for errors in ALB as well as for TS had a higher range than for ALADIN (for ALB 5–22%, for TS 2–22%). Thus, the investigation of REMO and ALADIN confirms the results with CLM that it is useful to invest some effort in relatively easily improvable parameters like CFR and ALB in further improvement of RCMs.

Fig. 11 Same figure as Fig. 6 but for REMO and ALADIN and only for surface radiation components
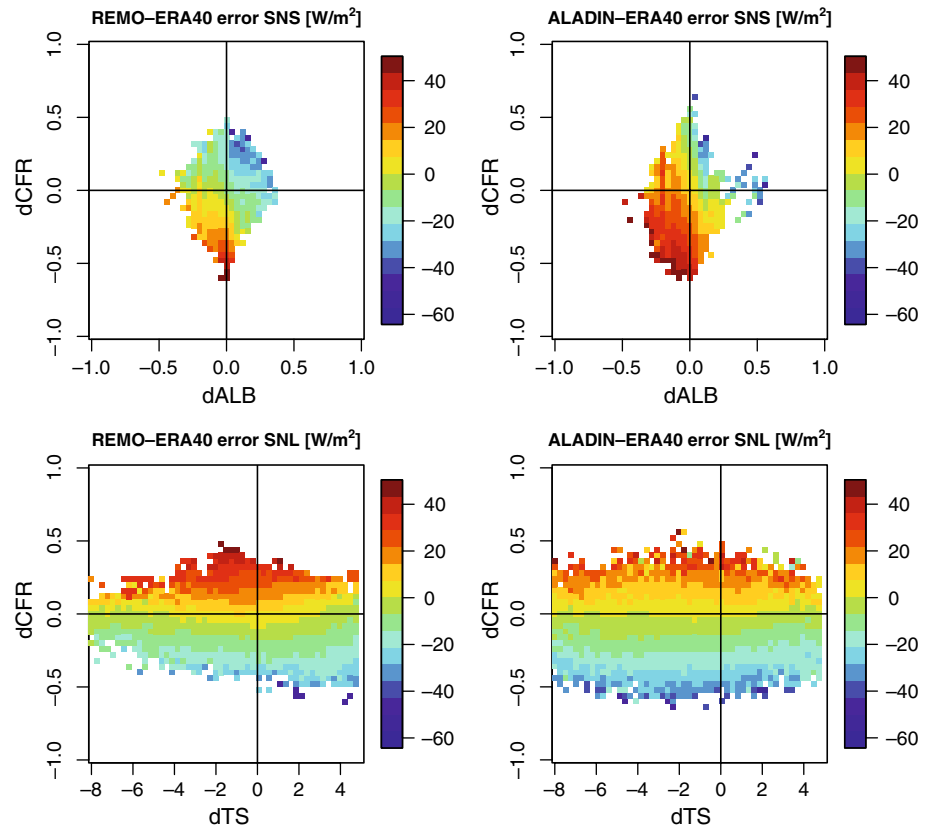
Appendix 2

By the help of a simplified calculation we wanted to discuss the impact of uncertainties in CFR, ALB, or TS on radiation fluxes. In the solar spectrum a cloud albedo of one and a transparent clear-sky atmosphere were assumed. Then the shortwave radiation components (SW) can be written to:

$$SW_{SFC}\downarrow = (1 - CFR) \cdot SW_{TOA}\downarrow$$
$$SW_{SFC}\uparrow = ALB \cdot (1 - CFR) \cdot SW_{TOA}\downarrow$$
$$SW_{TOA}\uparrow = SW_{TOA}\downarrow \cdot \left[ALB \cdot (1 - CFR)^2 + CFR \right]$$

The indices SFC and TOA represent the surface or top of atmosphere and the arrows $\uparrow$ or $\downarrow$ represent the upwelling or downwelling fluxes. The net short-wave fluxes are given by:

$$SNS = SW_{SFC}\downarrow - SW_{SFC}\uparrow = (1 - ALB) \cdot$$
$$(1 - CFR) \cdot SW_{TOA}\downarrow$$
$$TNS = SW_{TOA}\downarrow - SW_{TOA}\uparrow = SW_{TOA}\downarrow \cdot$$
$$\left[1 - ALB \cdot (1 - CFR)^2 + CFR \right]$$

The impact of errors in CFR and ALB is nearly linear, but (a) CFR is larger than ALB on average and (b) the error in CFR typically is larger than the error of ALB.

The average values are given in Table 1 and applied in simple calculations summarised in Table 2. The results show that an overestimation in CFR and ALB led to a decrease in SNS and TNS and that the impact of errors in CFR was larger than the impact of errors in ALB on average.

In case of long-wave radiation (LW) the single components are given by:

$$LW_{SFC}\uparrow = \sigma \cdot TS^4$$
$$LW_{SFC}\downarrow = 0.75 \cdot \sigma \cdot TS^4 \cdot \left(1 + 0.22 \cdot CFR^2 \right)$$
$$LW_{TOA}\uparrow = (1 - CFR) \cdot \sigma^* \cdot TS^{k^*} + CFR \cdot$$
$$\left((1 - \varepsilon^*) \cdot \sigma^* \cdot TS^{k^*} + \varepsilon^* \cdot \sigma^* \cdot TC^{k^*} \right)$$

The SFC components were estimated following Ångström and Bolz (see Warnecke 1997) with σ the Stefan Boltzmann constant. The outgoing long-wave radiation $LW_{TOA}\uparrow$ was approximated following Corti and

Table 1 Mean values and typical errors (mean errors of all data) for CFR, ALB and TS in the model simulations discussed

Parameter	Mean	Typical error
CFR	0.62	0.06
ALB	0.14	0.03
TS	284 K	−1.0 K

Table 2 Example of a simplified calculation of typical errors in SNS (denoted by ΔSNS) and TNS (denoted by ΔTNS) to test the sensitivity to uncertainties in CFR (denoted by ΔCFR) and ALB (denoted by ΔALB) under the assumption of $SW_{TOA}\downarrow = 1367/4$ W/m^2

ΔALB	ΔCFR	ΔSNS (W/m^2)	ΔTNS (W/m^2)
+0.03	0	−3.9	−1.5
0	+0.06	−17.6	−18.5
+0.03	+0.06	−20.9	−19.6

Peter (2009). They estimated the parameters σ^* and k^* to 1.607×10^{-4} Wm^{-2} K^{-4} and 2.528, respectively, by radiative calculations. For a mid-level cloud a cloud temperature TC = 255 K and an effective cloud emissivity $\varepsilon^* = 0.79$ (Allen 1971) were assumed. The choice of the cloud emissivity was important for the respective impact of CFR and TS (the higher ε, the higher is the impact of CFR and the lower the impact of TS). SNL and TNL are the difference of the downwelling minus the upwelling component:

$$SNL = LW_{SFC}\downarrow - LW_{SFC}\uparrow = \sigma \cdot TS^4 \cdot$$
$$\left(0.165 \cdot CFR^2 - 0.25\right)$$
$$TNL = 0 - LW_{TOA}\uparrow = -\sigma^* \cdot \left((1 - CFR) \cdot TS^{k^*}\right.$$
$$\left.+ CFR \cdot \left((1 - \varepsilon^*) \cdot TS^{k^*} + \varepsilon^* \cdot TC^{k^*}\right)\right)$$

For the example calculations in Table 3 typical errors of TS (denoted by ΔTS) and CFR (denoted by ΔCFR) were assumed (see Table 1). The table shows that the typical impact of errors in CFR was larger than in TS because of a partly compensation of terms with TS. In Table 3 it is also to see that ΔTNL in most cases was smaller than ΔSNL, while Fig. 1 shows a larger bias for TNL than for SNL. In combination with Fig. 7, where it can be seen that the explained variance for TNL was lower than for SNL, this shows that especially for TNL there were other important influencing factors besides CFR and TS. For example, Corti and Peter (2009) said that their parameterization could be improved by including a measure for the amount of absorption from water vapour, but they left it for simplification reasons.

Table 3 Example of a simplified calculation of typical errors in SNL (denoted by ΔSNL) and TNL (denoted by ΔTNL) to test the sensitivity to uncertainties in TS (denoted by ΔTS) and CFR (denoted by ΔCFR)

ΔTS	ΔCFR	ΔSNL (W/m^2)	ΔTNL (W/m^2)
−1 K	0	0.9	1.1
0 K	+0.06	4.7	2.9
−1 K	+0.06	5.6	3.9

References

Ahrens B, Karstens U, Rockel B, Stuhlmann R (1998) On the validation of the atmospheric model REMO with ISCCP data and precipitation measurements using simple statistics. Meteorol Atmos Phys (68):127–142. doi:10.1007/BF01030205

Allen J (1971) Measurements of cloud emissivity in the 8–13 μ waveband. J Appl Meteorol 10:260–265

Beck A, Ahrens B, Stadelbacher K (2004) Impact of nesting strategies in dynamical downscaling of reanalysis data. Geophys Res Lett 31:L19101. doi:10.1029/2004GL020115

Böhm U, Kücken M, Ahrens W, Block A, Hauffe D, Keuler K, Rockel B, Will A (2006) CLM—the climate version of LM: brief description and long-term applications. COSMO Newsl 6:225–235

Corti T, Peter T (2009) A simple model for cloud radiative forcing. Atmos Chem Phys Discuss 9:8541–8560

Dobler A, Ahrens B (2008) Precipitation by a regional climate model and bias correction in Europe and South Asia. Meteorol Z 17(4):499–509

Frei C, Christensen JH, Déqué M, Jacob D, Jones RG, Vidale PL (2003) Daily precipitation statistics in regional climate models: evaluation and intercomparison for the European Alps. J Geophys Res 108(D3):4124. doi:10.1029/2002JD002287

Gibson JK, Kållberg P, Uppala S, Nomura A, Hernandez A, Serrano E (1997) ERA description. ECMWF ERA15 Project Report Series, 1

Giorgi F, Marinucci MR, Visconti G (1990) Use of a limited area model nested in a general circulation model for regional climate simulation over Europe. J Geophys Res 95(18):413–418 431

Gupta SK, Ritchey NA, Wilber AC, Whitlock CH, Gibson GG, Stackhouse PW (1999) A climatology of surface radiation budget derived from satellite data. J Clim 12:2691–2710

Gupta SK, Stackhouse PW, Mikovitz JC, Cox SJ, Zhang T (2006) Surface radiation budget project completes 22-year data set. GEWEX WCRP News 16(4):12–13

Hagemann S, Machenhauer B, Jones R, Christensen O, Déqué M, Jacob D, Vidale P (2004) Evaluation of water and energy budgets in regional climate models applied over Europe. Clim Dyn 23(5):547–567

Hewitt CD, Griggs DJ (2004) Ensembles-based predictions of climate changes and their impacts. Eos 85:566

Hollweg HD, Fast I, Hennemuth B, Keup-Thiel E, Lautenschlager M, Legutke S, Schubert M, Wunram C (2008) Ensemble simulations over Europe with the regional climate model CLM forced with IPCC AR4 global scenarios. Technical Report No. 3, Max Planck Institute for Meteorology, Hamburg, Germany

Jacob D, Andrae U, Elgered G, Fortelius C, Graham LP, Jackson SD, Karstens U, Koepken C, Lindau R, Podzun R, Rockel B, Rubel F, Sass HB, Smith RND, Van den Hurk BJJM, Yang X (2001) A comprehensive model intercomparison study investigating the water budget during the BALTEX-PIDCAP period. Meteorol Atmos Phys 77(1–4):19–43

Jacob D, Bärring L, Christensen OB, Christensen JH, de Castro M, Déqué M, Giorgi F, Hagemann S, Hirschi M, Jones R, Kjellström E, Lenderink G, Rockel B, Sànchez ES, Schär C, Seneviratne SI, Somot S, van Ulden A, van den Hurk B (2007) An inter-comparison of regional climate models for Europe: design of the experiments and model performance. Clim Change 81(1):31–52. doi:10.1007/s10584-006-9213-4

Jaeger EB, Anders I, Lüthi D, Rockel B, Schär C, Seneviratne SI (2008) Analysis of ERA40-driven CLM simulations for Europe. Meteorol Z 17(4):349–367

Jaeger EB, Stöckli R, Seneviratne SI (2009) Analysis of planetary boundary layer fluxes and land–atmosphere coupling in the

regional climate model CLM. J Geophys Res 114:D17106. doi:10.1029/2008JD011658

Leung LR, Mearns LO, Giorgi F, Wilby RL (2003) Regional climate research. Bull Am Meteorol Soc 84:89–95

Markovic M, Jones CG, Vaillancourt PA, Paquin D, Winger K, Paquin-Ricard D (2008) An evaluation of the surface radiation budget over North America for a suite of regional climate models against surface station observations. Clim Dyn 31(7–8):779–794

Marras S, Jimenez P, Jorba O, Perez C, Baldasano JM (2007) Present-day climatic simulations run with two GCMs: a comparative evaluation against ERA40 reanalysis data. American Geophysical Union, Fall Meeting 2007

Mitchell TD, Jones PD (2005) An improved method of constructing a database of monthly climate observations and associated high-resolution grids. Int J Climatol 25:693–712

Ohmura A, Dutton EG, Forgan B, Fröhlich C, Gilgen H, Hegner H, Heimo A, König-Langlo G, McArthur B, Müller G, Philipona R, Pinker R, Whitlock CH, Dehne K, Wild M (1998) Baseline Surface Radiation Network (BSRN/WCRP): new precision radiometry for climate research. Bull Am Meteorol Soc 79(10):2115–2136

Pinker RT, Laszlo I (1992) Modeling surface solar irradiance for satellite applications on a global scale. J Appl Meteorol 31:194–211

Radu R, Déqué M, Somot S (2008) Spectral nudging in a spectral regional climate model. Tellus 60A(5):885–897. doi:10.1111/j.1600-0870.2008.00343.x

Reichler T, Kim J (2008) Uncertainties in the climate mean state of global observations, reanalyses, and the GFDL climate model. J Geophys Res 113:D05106. doi:10.1029/2007JD009278

Ritter B, Geleyn JF (1992) A comprehensive radiation scheme for numerical weather prediction models with potential applications in climate simulations. Mon Weather Rev 120:303–325

Sanchez-Gomez E, Somot S, Déqué M (2008) Ability of an ensemble of regional climate models to reproduce the weather regimes during the period 1961–2000. Clim Dyn 33(5):723–736. doi:10.1007/s00382-008-0502-7

Shmakin AB, Milly PCD, Dunne KA (2002) Global modeling of land water and energy balances. Part III: interannual variability. J Hydrometeorol 3:311–321

Smiatek G, Rockel B, Schättler U (2008) Time invariant data preprocessor for the climate version of the COSMO model (COSMO-CLM). Meteorol Z 17(4):395–405

Steppeler J, Dom G, Schättler U, Bitzer HW, Gassmann A, Damrath U, Gregoric G (2003) Meso-gamma scale forecasts using the nonhydrostatic model LM. Meteorol Atmos Phys 82:75–96

Tiedtke M (1989) A comprehensive mass flux scheme for cumulus parameterization in large-scale models. Mon Weather Rev 117:1779–1800

Tjernström M, Sedlar J, Shupe MD (2008) How well do regional climate models reproduce radiation and clouds in the arctic? An evaluation of ARCMIP simulations. J Appl Meteorol Climatol 47:2405–2422

Uppala SM, Kallberg PW, Simmons AJ, Andrae U, Bechtold VD, Fiorino M, Gibson JK, Haseler J, Hernandez A, Kelly GA, Li X, Onogi K, Saarinen S, Sokka N, Allan RP, Andersson E, Arpe K, Balmaseda MA, Beljaars ACM, Berg LVD, Bidlot J, Bormann N, Caires S, Chevallier F, Dethof A, Dragosavac M, Fisher M, Fuentes M, Hagemann S, Holm E, Hoskins BJ, Isaksen L, Janssen PAEM, Jenne R, Mcnally AP, Mahfouf JF, Morcrette JJ, Rayner NA, Saunders RW, Simon P, Sterl A, Trenberth KE, Untch A, Vasiljevic D, Viterbo P, Woollen J (2005) The ERA40 re-analysis. Q J R Meteorol Soc 612:2961–3012

Vidale PL, Lüthi D, Frei C, Seneviratne SI, Schär C (2003) Predictability and uncertainty in a regional climate model. J Geophys Res 108(D18):4586. doi:10.1029/2002JD002810

Warnecke G (1997) Meteorologie und Umwelt: Eine Einführung. Springer, Heidelberg

Wild M (2008) Short-wave and long-wave surface radiation budgets in GCMs: a review based on the IPCC-AR4/CMIP3 models. Tellus A 60(5):932–945

Wild M, Ohmura A, Gilgen H, Morcrette JJ (1998) The distribution of solar energy at the earth's surface as calculated in the ECMWF re-analysis. Geophys Res Lett 25(23):4373–4376

Wild M, Ohmura A, Gilgen H, Morcrette JJ, Slingo A (2001) Evaluation of downward longwave radiation in general circulation models. J Clim 14:3227–3239

Winter JM, Eltahir EA (2008) Evaluating regional climate model version 3 Over the Midwestern United States. American Geophysical Union, Spring Meeting 2008

Wyser K, Jones C, Du P, Girard E, Willén U, Cassano J, Christensen J, Curry J, Dethloff K, Haugen J, Jacob D, Køltzow M, Laprise R, Lynch A, Pfeifer S, Rinke A, Serreze M, Shaw M, Tjernström M, Zagar M (2008) An evaluation of Arctic cloud and radiation processes during the SHEBA year: simulation results from eight Arctic regional climate models. Clim Dyn 30(2–3):203–223

Zhang Y, Rossow WB, Stackhouse PW (2006) Comparison of different global information sources used in surface radiative flux calculation: radiative properties of the near-surface atmosphere. J Geophys Res 111:D13106. doi:10.1029/2005JD006873

Zhang Y, Rossow WB, Stackhouse PW (2007) Comparison of different global information sources used in surface radiative flux calculation: radiative properties of the surface. J Geophys Res 112:D01102. doi:10.1029/2005JD007008

Zhang T, Stackhouse PW, Gupta SK, Cox SJ, Mikovitz JC (2009) Validation and analysis of the release 3.0 of the NASA GEWEX surface radiation budget dataset. AIP Conf Proc 1100:597. doi:10.1063/1.3117057

List of publications by A. Dobler

Peer reviewed journals

Dobler, A. and B. Ahrens, 2010: Analysis of the Indian summer monsoon system in the regional climate model COSMO-CLM. *J. Geophys. Res.*, **115**, D16101, doi:10.1029/2009JD013497.

Kothe, S., A. Dobler, A. Beck and B. Ahrens, 2010: The radiation budget in a regional climate model. *Clim. Dyn.*, in press, doi:10.1007/s00382-009-0733-2

Dobler, A., M. Yaoming, N. Sharma, S. Kienberger and B. Ahrens, 2010: Regional climate projections in two alpine river basins: Upper Danube and Upper Brahmaputra. *Adv. Sci. Res.*, submitted

Dobler, A. and B. Ahrens, 2010: Four climate change scenarios for the Indian summer monsoon by the regional climate model COSMO-CLM. *J. Geophys. Res.*, submitted

Steppeler, J., A. Dobler, S. Park, 2010: A Five Day hindcast experiment using a cut cell z-Coordinate model. *Atm. Sci. Lett.*, submitted

Dobler, A., R. Müller and B. Ahrens, 2010: Development and evaluation of a method for estimating evapotranspiration from satellite data, *Rem. Sens.*, in revision

Dobler, A. and B. Ahrens, 2008: Precipitation by a regional climate model and bias correction in Europe and South Asia. *Meteorol. Zeitschrift*, **17(4)**: 499-509

Contributed papers

Dobler, A., 2010: Implementation of cut cells in a well-balanced 2D finite volume model. Cut Cell Methods for Atmosphere and Ocean Modeling 2010. Berlin, Germany, 05 July 2010

Dobler, A. and B. Ahrens, 2010: Analysis of the Indian summer monsoon system in the regional climate model COSMO-CLM . EGU general assembly 2010. Vienna, Austria, 05 May 2010

Dobler, A. and B. Ahrens, 2009: ERA Interim angetriebene Klimasimulationen mit dem COSMO-CLM im CORDEX Gebiet "West-Asia". Deutsche Kliamtagung 2009. Bonn, Germany, 05 October 2009

Dobler, A. and B. Ahrens, 2009: The Asian summer Monsoon in ERA40 driven CLM simulations. 2nd Lund Regional-scale Climate Modeling Workshop. Lund, Sweden, 04 May 2009

Dobler, A. and B. Ahrens, 2009: ERA40 driven CLM simulations in the European and the south Asian region. EGU general assembly 2009. Vienna, Austria, 22 April 2009

Dobler, A., B. Ahrens, M. Yaoming and N. Sharma, 2008: Precipitation modeling in Europe and South-Asia. EGU general assembly 2008. Vienna, Austria, 14 April 2008

Ahrens, B. and A. Dobler, 2008: Climate change projections in the upper Danube (European Alps) and the upper Brahmaputra (Himalayas). Extended abstract. 17th Conference on Applied Climatology. Whistler, BC, Canada, 13 August 2008

Dobler, A. and B. Ahrens, 2007: Tägliche Beobachtungsdaten für Downscaling und Debiasing von Niederschlagsfeldern. DACH 2007. Hamburg, Germany, 10 September 2007

Dobler, A., B. Ahrens and D. Luethi, 2007: Downscaling of precipitation - need and use of observational data. EGU general assembly 2007. Vienna, Austria, 20 March 2007

Diploma thesis and term papers

Dobler, A., 2005: A 2D Finite Volume Non-hydrostatic Atmospheric Model - Implementation of Cut Cells and further Improvements. Diploma thesis, Institut für Atmosphäre und Klima, ETH Zürich

Dobler, A., 2003: Softwareentwicklung zur visuellen Untersuchung von heterogener Eisnukleation. Term paper, Institut für Atmosphäre und Klima, ETH Zürich

Dobler, A., 2004: Ein Modellsystem für die ideale Magnetohydrodynamik. Term paper, Seminar für Angewandte Mathematik, ETH Zürich

Curriculum Vitae

Contact information

Dobler Andreas
Schulstr. 42
60594 Frankfurt/Main

Phone: 069 798 40234
dobler@iau.uni-frankfurt.de

Personal information

Date of birth	07. June 1978
Place of origin	Appenzell AI, Switzerland
Citizenship	Swiss
Sex	Male
Marital Status	unmarried

Education

11/2006-06/2010	Ph.D. in geosciences at Goethe University, Frankfurt/Main
10/2001-02/2005	Diploma in computational sciences and engineering at ETH Zürich
10/1998-10/2001	Intermediate diploma in maths at ETH Zürich
08/1993-01/1998	Matura at cantonal secondary school Sargans

Work experience and internships

since 07/2010	Research assistantat at Biodiversity and Climate Research Centre, Frankfurt/Main
11/2006-07/2010	Research assistantat at Goethe University, Frankfurt/Main
01/2005-10/2006	Post-graduand at the Institut für Atmosphäre und Klima, ETH Zürich
08/2003-06/2006	Software quality assurance assistant at GretagMacbeth, Regensdorf ZH
10/2003-02/2004	Tutor for probability and statistics at the Seminar für Statistik, ETH Zürich
07/2003-08/2003	Internship at Eco Physics AG, Dürnten ZH
02/2003-07/2003	Call-Center-Agent at Zürcher Kantonalbank, Zürich
03/2002-07/2003	Tutor for probability and statistics at the Seminar für Statistik, ETH Zürich

Language skills

Swiss German	mother tongue
German	like mother tongue
English	fluent in spoken and written language
French	good knowledge

Computer skills

Operating systems	proficient in Linux and Windows, good knowledge in OS X
Programming	proficient in Fortran and html, good knowledge in C++, C, Java and LabView
Parallelization	knowledge in MPI and OpenMP
Script languages	proficient in R and Matlab, knowledge in Maple and Mathematica
Office	proficient in LaTeX, OpenOffice and MS-Office